

# Dynamics of Highly Charged Finite Systems Induced by Intense X-ray Pulses

## Dissertation

zur Erlangung des akademischen Grades  
Doctor rerum naturalium (Dr. rer. nat.)

vorgelegt von

**Abraham Camacho Garibay**

geboren am 21.11.1982 in Tlalnepantla, México



1. Gutachter: \_\_\_\_\_
2. Gutachter: \_\_\_\_\_
3. Gutachter: \_\_\_\_\_



*A mi padre.*

*A mi madre,  
con sus diferentes rostros,  
y sus diferentes nombres.*



# Abstract

The recent availability of X-ray Free Electron Lasers (XFELs) has opened a completely new and unexplored regime for the study of light-matter interactions. The extremely bright intensities delivered by XFELs can couple many photons into the target, turning well known interactions such as photoionization and scattering into new, non-linear, complex many-body phenomena. This thesis reports theoretical investigations aiming to improve the understanding of the fundamental processes and dynamics triggered by intense X-ray pulses, with a special focus in finite systems such as molecules and clusters.

Sequential multiple photoionization in atomic clusters was investigated, where previous observations were extended for higher charge states where direct photoionization is frustrated. Through a rate equation study and subsequent molecular dynamics simulations, it was found that frustrated ionization is partially responsible for the low-energy peak observed in the electron energy spectrum. The influence of plasma evaporation over the formation of the sequential low-energy peak was also investigated, identifying the effects of the system size and photon energy.

Multiple channel ionization was also investigated for the case of fullerenes. This is done through a series of studies, starting from a simplified rate equation scheme, and culminating with full molecular dynamics simulations. From these results, a good insight was obtained over the origin, physical meaning, and relevant parameters that give rise to the complicated features observed in the electronic spectra. The mechanisms responsible of all these features are expected to be present in other systems, making these results quite general.

Diffraction imaging of biomolecules was studied in a final step, with a particular focus on the influence of intramolecular charge transfer mechanisms. To this end a conformer of T4 Lysozyme was used, a representative enzyme with well known structure. Charge migration is found to allow for additional processes such as proton ejection, a mechanism which enables an efficient release of energy from the system. This mechanism considerably suppresses structural damage for heavy ions, improving the quality of the measured diffraction patterns.



# Contents

<b>1</b>	<b>Introduction</b>	<b>3</b>
<b>2</b>	<b>Concepts in XFEL Phenomena</b>	<b>7</b>
2.1	Light-Matter Interaction with X-rays . . . . .	7
2.1.1	Elastic Scattering . . . . .	8
2.1.2	Compton Scattering . . . . .	9
2.1.3	X-ray Photoionization . . . . .	9
2.2	Auger Decay and X-ray Fluorescence . . . . .	10
2.2.1	Auger Transitions . . . . .	11
2.2.2	X-ray fluorescence . . . . .	12
2.2.3	Widths and fluorescence yields . . . . .	12
2.3	An Overview of Numerical Methods in XFEL Dynamics . . . . .	14
2.3.1	The Nanoplasma and other Rate Equation Models . . . . .	14
2.3.2	Molecular Dynamics . . . . .	16
<b>3</b>	<b>Multiple Ionization in Clusters</b>	<b>19</b>
3.1	Frustrated Ionization in Clusters . . . . .	19
3.2	Analytical Results for Sequential Ionization . . . . .	21
3.2.1	Frustrated Sequential Ionization in Clusters . . . . .	23
3.2.2	Analytical Approximation for Frustrated Ionization . . . . .	24
3.3	Coulomb Complex Study . . . . .	26
3.4	Plasma Formation in Sequential Ionization . . . . .	30
3.5	Conclusions . . . . .	36
<b>4</b>	<b>Multiple Channel Ionization and Ionic Motion</b>	<b>39</b>
4.1	Rate Equation Description of Multi-channel Ionization . . . . .	41
4.1.1	Rate equation description of two channels . . . . .	42
4.2	Molecular Dynamics of Multi-channel Ionization in Fullerenes . . . . .	51
4.2.1	MD Simulation Details . . . . .	51
4.2.2	Multiple Ionization of Fullerenes with Fixed Ions . . . . .	53
4.2.3	Influence of Ionic Motion in the Multiple Ionization of Fullerene . . . . .	60
4.3	Dynamical Footprints of Auger Decay Rates . . . . .	64

4.3.1	Bottle-Neck Model of Multi-channel Ionization . . . . .	67
4.4	Conclusions . . . . .	70
<b>5</b>	<b>Charge Migration in XFEL Diffractive Imaging</b>	<b>73</b>
5.1	Diffraction before destruction . . . . .	74
5.2	Charge Transfer in Heterogeneous Clusters . . . . .	76
5.3	Charge Migration in Biomolecules . . . . .	78
5.3.1	Time Evolution . . . . .	81
5.4	Influence in XFEL Diffractive Imaging . . . . .	83
5.5	Ionic Motion and Coulomb Explosion . . . . .	88
5.5.1	Deterministic trajectories in sulphur . . . . .	90
5.5.2	Conclusions . . . . .	92
<b>6</b>	<b>Summary and Outlook</b>	<b>93</b>
6.1	Multiple Ionization . . . . .	93
6.2	Multiple Channel Ionization . . . . .	94
6.3	Charge Migration . . . . .	95
	<b>List of Figures</b>	<b>97</b>
	<b>Bibliography</b>	<b>99</b>

# Chapter 1

## Introduction

From its very first steps such as the discovery of the X-rays or the photoelectric effect, AMO physics has contributed to the development of some of the most important scientific achievements in the history of mankind. It was certainly one of the main drivers for the development of quantum mechanics at the beginning of the last century, opening a new era not only in physics but in science as a whole. Not only that, but the methods and technologies developed in AMO physics have also found applications in all branches of knowledge and in our daily lives, ranging from spectroscopic techniques and atomic clocks to laser technology and medical imaging. But it is not just only the past glories where AMO physics find its importance, as it is still a relevant, cutting edge, booming and rapidly advancing field, evidenced by the fact that no less than four Nobel prizes have been awarded in the last two decades for achievements in AMO. This advancements are nowadays led not only by new ideas and breakthroughs, but are also accompanied by major developments in technology allowing for a better reliability, performance and control of both atoms and molecules, as well as new light sources with unprecedented properties.

It is precisely one of such recently available light sources one of the main drivers behind the work presented here, that is, the X-ray free electron lasers (XFELs). These novel light sources enable a completely new point of view for the study of light-matter interaction, including atomic and molecular dynamics in previously unreachable regimes and new techniques to probe systems and retrieve detailed structural information. XFELs are unique in many ways, starting from their high photon fluxes which make it possible to collect a scattering signal from small, dilute, or non-periodic systems. This high flux also implies that the pulse is no longer a weak perturbing probe (a *de facto* assumption in most traditional X-ray experiments) but through the deposition of large amounts of photons into the samples, they are capable of creating exotic and extreme states of matter far from equilibrium. Furthermore, operating within the X-ray regime the wavelengths allow for diffraction experiments with atomic resolution, and their interaction with inner-shell electrons provide both environmental as well as element specific information. Finally, as the laser is delivered in pulses with lengths on the order of femtoseconds, it is feasible to follow the time evolution of ultrafast processes in atoms,

molecules and aggregates, including chemical reactions and phase transitions. From all these characteristics, the potential applications of XFELs permeate research in atomic physics, material science, chemical catalysis, astrophysics, structural biology and many other scientific disciplines, fostering new ideas and posing new challenges.

In the last decade a handful of XFEL facilities have become operational, starting in 2005 with the first lasing of FLASH [1,2] in Hamburg, and quickly followed by LCLS [3] in California, SCSS [4] and SACLA [5] in Japan, and FERMI [6] in Trieste. In addition, some others are already under construction like the European XFEL [7] or the Swiss-FEL [8], and are expected to become operational in the near future. From the very first experiments it was found that in this new regime of intensities even well studied phenomena in atoms, molecules and clusters often show unexpected results, like the observation of extremely high atomic charge states in Xe clusters [9] or the plasma creation and subsequent explosion of clusters [10], making it clear that nonlinear processes were going to be commonplace phenomena. Despite the short time they have been available, these facilities have already achieved several major scientific breakthroughs covering a wide range of topics. Some examples include the FEL imaging of living bacteria and cell organelles [11,12], viruses [13], membrane proteins as well as the undamaged structure at room temperature of photosystem II [14], including its highly radiation sensitive  $\text{Mn}_4\text{CaO}_5$  cluster, and tracking its photosynthetic cycle [15]. Other achievements include new understanding of photochemical reactions through the determination of the reaction intermediates from photoactive yellow proteins [16], as well as the determination of structures with high impact in medicine such as the CatB protease, a potential drug target against the serious disease of sleeping sickness [17].

From the previous examples it is clear that complex atoms, molecules, clusters, and nanostructures are very interesting targets for XFEL experiments, usually possessing many degrees of freedom, multiple ionization channels, complicated structures, different constituents and inhomogeneities, often showing a highly correlated behavior and nontrivial couplings. A fundamental understanding of both the nonlinear light-matter interactions, as well as the complicated electronic and ionic dynamics triggered in these systems by such interactions are not only interesting topics in their own right, but also essential prerequisites for numerous applications. Unfortunately, both the complex structures and the nonlinear phenomena present make it a very complicated goal to achieve. Here we make a modest contribution to better understand some of these phenomena, with a special focus and interest for the case of highly charged systems. Special care has been put into making our results as general as possible by studying systems that are both representative and pose a special interest in different research areas.

To familiarize the reader with some of the basic interactions of X-rays with matter, we provide in Chapter 2 a simple and short review of the necessary background, focusing in particular on the relevant concepts for the case of isolated atoms and how they extend to more complicated systems. We make special emphasis of single photon ionization, Auger decay, and elastic scattering, and briefly mention the particular challenges imposed by the high intensities of XFELs. A discussion of the numerical methods and tools commonly used in the dynamics of complex finite systems is also included, highlighting



some of their comparative advantages and drawbacks.

A recurring theme in the present work is the analysis of systems and scenarios with increasing levels of complexity and our results are presented following the same philosophy. We begin in Chapter 3 for the case of sequential multiple photon ionization in atomic clusters, where we first review some known results of sequential ionization and immediately generalize them for charge states high enough that trapping of electrons is an important effect. From this generalization a new feature arises naturally in the photoelectron spectra in the form of what appears to be a low energy structure for clusters. We are able to explain this feature, as well as to propose a simple analytical formula showing remarkably good agreement. A molecular dynamics study in the framework of Coulomb Complexes further confirms our results and gives hints of additional effects due to the plasma electron evaporation.

We continue in Chapter 4 where we study the multiple ionization dynamics of molecules, for which the many ionization channels make the interpretation of their photoelectron spectra a quite formidable task. We focus our effort on fullerene  $C_{60}$ , an intriguing molecule with simple spherical symmetry that is representative of this general problem. A series of studies with progressive degrees of complication are performed, starting with a rate equation analysis for two subsequent ionization channels and finalizing with a full molecular dynamics simulation including both electronic and ionic degrees of freedom. In this way we are able to obtain a fair amount of insight which might allow for an easier interpretation of experimental results. Further implications of the obtained results are discussed.

Finally in Chapter 5 we deal with the issue of charge transfer in biological molecules and its impact in single-particle diffractive imaging experiment. To this end we analyze a conformer of a T4 lysozyme mutant (pdb entry 2LC9), which contains all the major atomic species present in systems of biological interest. Building on the previous chapters, we perform from the very beginning a full molecular dynamics simulation, where both electronic impact and field ionization, as well as charge transfer is taken into account. By tracking the time evolution of the system, both as a whole and by atomic species, we observe that these mechanisms have important consequences. The diffraction pattern of this system is calculated, taking into account the time dependent positions and structure factors, and the influence of these mechanisms are discussed. We close our study by analyzing the movement of sulphur ions during and after the pulse, and the potential information they carry about the molecular orientation.



## Chapter 2

# Concepts in XFEL Phenomena

The process of making XFEL sources a reality required the combination of multiple interdisciplinary efforts and developments [18] and the potential applications of XFEL pulses have attracted the attention of even more disciplines, from molecular biology, nanoscience, cluster physics, biochemistry, among many others, slowly merging and forming a completely new community. In such an interdisciplinary field, understanding all the processes involved represents a tremendous challenge just by the wide spectrum of highly specialized topics. An exhausting coverage of the background required to understand all XFEL applications would therefore be an extremely formidable effort, and clearly falls outside the goal of any reasonable introduction. Here we only attempt to provide a simple and clear exposition of the most relevant and fundamental physical processes occurring in the interaction of X-rays with matter, in a hopefully sufficient measure as required for the following chapters. The particularities and importance of these phenomena in XFEL experiments are highlighted by presenting some recent and often surprising results.

Equally important as the light-matter interactions are the coulombic interaction among particles as well as their time evolution. The diverse applications, target sizes and complexities, energies and time scales allowed for different theoretical frameworks and numerical methods to be developed, each with different advantages and limitations. For that reason we also devote a space to talk about some of the most widely used approaches for the study of particle dynamics in XFEL phenomena, while focusing in those who are particularly relevant for upcoming chapters.

### 2.1 Light-Matter Interaction with X-rays

The interaction of light with matter involves many distinct processes, and the relative importance and efficiency of each one strongly depends on the energy of the photons. Usually X-rays are considered to span the range from  $\approx 100$  eV to  $\approx 100$  keV in energy, or somehow equivalently from  $\approx 0.01$  nm to  $\approx 10$  nm in wavelength. In this energy region the photons mainly interact with atoms in two different ways: elastically through Rayleigh scattering, or by the inelastic interactions of photoionization and Compton

scattering. As the inelastic interactions with inner electrons are favored, the atom is often left with an inner shell vacancy which tends to decay predominantly via Auger transitions or X-ray emission.

All these previous phenomena are fundamental concepts to understand the applications and research performed in XFEL facilities.

### 2.1.1 Elastic Scattering

Also known as Rayleigh scattering, this denotes the scattering produced by bound atomic electrons. For angles different than  $0^\circ$  elastic scattering has progressively higher contributions from deeper shells with an increasing photon energy, making it sensible to the atomic structure. This process is usually understood by the use of form factors, which treat the scattered radiation as a superposition of the contributions from different volume elements. The form factor  $A(\mathbf{k})$  of a charge density  $\rho(\mathbf{r})$  is therefore just its Fourier transform [19]

$$A(\mathbf{k}) = \int d^3r \rho(\mathbf{r}) e^{i\mathbf{k}\cdot\mathbf{r}}, \quad (2.1)$$

with  $\mathbf{k}$  being the momentum transfer, whose magnitude is obtained in turn by

$$k = \frac{2\hbar\omega}{c} \sin\left(\frac{\theta}{2}\right), \quad (2.2)$$

where  $\theta$  is the scattering angle. This form factor serves as a correction to the Thomson scattering cross-section from point charges, from which the differential Rayleigh scattering cross-section then reads

$$\frac{d\sigma}{d\Omega} = r_e^2 |\boldsymbol{\varepsilon} \cdot \boldsymbol{\varepsilon}'|^2 A(\mathbf{k}), \quad (2.3)$$

where  $r_e$  denotes the Thomson scattering length or classical radius of the electron, while  $\boldsymbol{\varepsilon}$  and  $\boldsymbol{\varepsilon}'$  are correspondingly the polarization vectors of the incoming and scattered waves.

The next step of complication is the scattering by molecules composed by many atoms, for which a scattering factor can also be assigned by

$$A^{\text{mol}}(\mathbf{k}) = \sum_j A_j(\mathbf{k}) e^{i\mathbf{k}\cdot\mathbf{R}_j} \quad (2.4)$$

where, as before,  $A_j(\mathbf{k})$  is the atomic factor of the  $j$ -th atom in the molecule, located at  $\mathbf{R}_j$ . In principle if  $|A^{\text{mol}}(\mathbf{k})|^2$  is experimentally determined for sufficiently many values of  $\mathbf{k}$ , then the atomic positions in the molecule could be determined [20]. In reality the use of common X-ray sources have to exploit the periodic structure of crystals to obtain a measurable signal, which cannot be produced from a single molecule. The use of XFEL pulses as a way to avoid this problem is currently a topic of intense research and will be treated later in chapter 5.

### 2.1.2 Compton Scattering

The term Compton scattering usually denotes scattering from free electrons, but it is also applied for the inelastic scattering from bound electrons when the incoming photon energy exceeds considerably the electron binding energy, as is the case for X-rays. Within the lowest-order relativistic quantum electrodynamics, Compton scattering is described by the Klein-Nishina formula, approximated at low energies by [21]

$$\sigma^{\text{KN}} = \sigma^{\text{T}} \left( 1 + \frac{2\hbar\omega}{m_e c^2} + \dots \right), \quad \hbar\omega \ll m_e c^2 \quad (2.5)$$

where  $\sigma^{\text{T}}$  is the classical Thomson scattering cross section,

$$\sigma^{\text{T}} = \frac{8\pi}{3} r_e^2, \quad (2.6)$$

being  $r_e$  the classical electron radius. The energy  $\hbar\omega'$  of a photon scattered at an angle  $\theta$  relates to the incident photon energy  $\hbar\omega$  by the Compton relation

$$\hbar\omega' = \frac{\hbar\omega}{1 + (\hbar\omega/m_e c^2)(1 - \cos\theta)}. \quad (2.7)$$

Finally, in the limit  $\omega' \rightarrow \omega$  the differential cross-section simply reduces to the Thomson differential cross-section

$$\frac{d\sigma^{\text{T}}}{d\Omega} = r_e^2 |\boldsymbol{\varepsilon} \cdot \boldsymbol{\varepsilon}'|^2. \quad (2.8)$$

Compton scattering is the dominant interaction for the highest X-ray photon energies (roughly above 100 keV), but does not contribute significantly for lower energies. Additionally for XFELs, recent results seem to suggest the observation of non-linear Compton scattering, where concerted Compton scattering of two identical photons by an electron produces a single more energetic photon, a process which appears to scale quadratically with respect to the intensity [22, 23].

### 2.1.3 X-ray Photoionization

Perhaps one of the most basic and well studied light-matter interactions is the ionization by the absorption of a single photon, whose first accounts can be traced back to the photoelectric effect in solids and its contributions to the development of quantum mechanics. Nowadays photoemission is also a powerful tool for the investigation of matter, as photoelectron spectroscopy helps to reveal the nature of bound electrons. In the simplest terms it can be expressed as a process where an electron located in a solid, molecule or atom, increases its energy by absorbing a photon. In the X-ray regime photons usually are energetic enough to move the electron into the continuum, leaving the original atom.

This absorption process is usually discussed in terms of cross-sections, which are a measure of the probability of such interaction. For an atom with  $Z$  electrons this cross-section can be derived from first order perturbation theory, within the validity of the

dipole approximation, as [21, 24, 25]

$$\sigma(\omega) = \frac{4\pi^2\alpha}{\omega} \sum_f \left| \sum_{n=1}^Z \langle \Psi_f | \boldsymbol{\varepsilon} \cdot \hat{\mathbf{p}}_n | \Psi_i \rangle \right|^2 \delta(E_f - E_i - E_\omega) \quad (2.9)$$

where  $E_\omega$  is the photon energy,  $E_i$  and  $E_f$  are the energies of the corresponding initial and final states  $\Psi_i$  and  $\Psi_f$ ,  $\boldsymbol{\varepsilon}$  is the polarization vector of the incoming photon, and the index  $n$  spans all the available electrons<sup>1</sup>. The delta function ensures energy conservation by requiring that  $E_f = E_i + \omega$ . If along the emission process all the remaining electrons can be considered to be unaffected, Koopman's theorem states that  $E_i$  equals the binding energy of the emitted electron.

The ionization rate  $\Gamma$  of an atom is obtained by means of Fermi's golden rule, which can be expressed quite simply with the use of  $\sigma(\omega)$  as

$$\Gamma = \frac{I\sigma(\omega)}{\hbar\omega}, \quad (2.10)$$

where  $I$  is the intensity or flux of the ionizing pulse hitting the atom. It should be noted that the cross section does not depend on the field strength and, therefore, for a given photon energy the photoionization rate usually increases linearly with respect to the intensity. This is no longer the case in the X-ray regime as the energy of the incoming photons is high enough to generate subsequent states with higher charge states by a series of *sequential* single-photon events [26], which give rise to a non-linear ionization process. The high intensities provided by XFELs can even deplete the atom entirely of its electrons, effectively rendering it transparent to the pulse [27, 28].

All these previous interactions have a different dependence with respect to the photon energy, which means that for different regions of the spectrum the relative importance of each process will change. Interactions that might not be very important for some photon energies can completely dominate at other energy regions. While these interactions depend on the atomic species a general trend is shared, as depicted in Fig. 2.1.

## 2.2 Auger Decay and X-ray Fluorescence

Atoms with inner shell vacancies formed through X-ray photoionization are highly excited states that tend to decay either through non-radiative Auger transitions or through X-ray fluorescence, that arise from the electronic Coulomb interactions. In atoms of low  $Z$ , the Auger decay rate is much higher than the corresponding X-ray fluorescence rate. In heavier atomic species (for  $Z > 30$ ) inner-shell states decay predominantly, in a first step, through X-ray fluorescence. This behavior relates to the fact that while the electronic density of states increases as a square root of the electron energy, the photon density of states increases quadratically with respect to the photon energy.

---

<sup>1</sup>Definition (2.9) is not unique and alternative forms of the photoionization cross-section can be found in literature using the “length”, “velocity”, and “acceleration” forms of the dipole operator. These forms arise by making use of the commutation relations of  $\hat{\mathbf{p}}$  with the Coulomb potential [21].

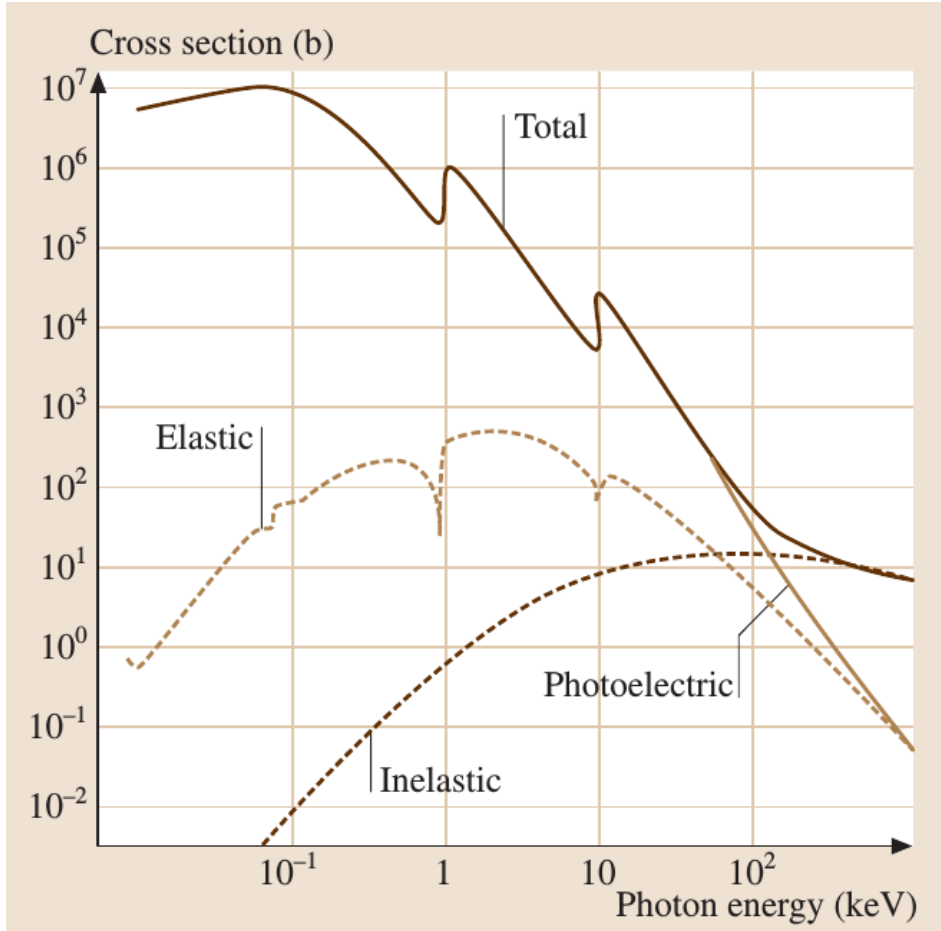
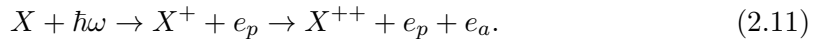


**Figure 2.1:** Relative contributions of the elastic Rayleigh scattering, inelastic Compton scattering, and photoionization cross-sections of Cu, as a function of the photon energy. While the actual values of each contribution depend of the atomic species, the same trends are observed across most elements. Taken from [21].

### 2.2.1 Auger Transitions

Auger electron emission is usually described as a two-step process in which the decay follows incoherently the core hole creation [29]



This approximation holds if the photoelectron ( $e_p$ ) is sufficiently energetic that it does not interact with the Auger electron ( $e_a$ ), and core hole state only interacts weakly with the Auger continuum. In this case the core hole state can be considered to be quasi-stationary and the decay rate can be expressed according to Wentzel's Ansatz as [21, 25]

$$\Gamma_{i,jj'} = 2\pi \sum_a |\nu_{aijj'} - \nu_{aij'j}|^2 \rho(E_f), \quad (2.12)$$

where  $\rho(E_f)$  is the density of energy conserving final states for the energy  $E_f$ , and

$$\nu_{pqrs} = \left\langle \Psi_{pq}(\mathbf{x}, \mathbf{x}') \left| \frac{1}{|\mathbf{x} - \mathbf{x}'|} \right| \Psi_{rs}(\mathbf{x}, \mathbf{x}') \right\rangle \quad (2.13)$$

denote two-electron Coulomb matrix elements. Clearly the Auger process does not depend on the incoming field, as it is a purely electronic phenomenon.

The Auger transition energy  $E_A$  or kinetic energy of the emitted electron, within the central field model, is

$$E_A(klm) = E_k - E_{l,m}, \quad (2.14)$$

where  $E_k$  and  $E_{l,m}$  correspondingly denote the energies of the states with one and two vacancies defined by the subscripts, commonly used in the literature as labels to identify a given transition.

The use of XFEL sources have made it possible to create double core-hole states which gives rise to a distinct Auger-spectra compared to the usual single core-hole case [30]. The binding energies associated to this double core-hole states are more sensitive to chemical shifts and has motivated studies in molecular double core-hole spectroscopy, as well as theoretical studies about their lifetime [31].

### 2.2.2 X-ray fluorescence

The study of X-ray emission, despite being less probable, precedes non-radiative transitions and has been widely used to research atomic structure. The X-ray fluorescence rate is also obtained by first order time-dependent perturbation theory in the dipole approximation, reading

$$\Gamma_{i,i'} = \frac{4}{3} \alpha^3 (E_{i'} - E_i) \left| \left\langle \Psi_i \left| \frac{\nabla}{i} \right| \Psi_{i'} \right\rangle \right|^2, \quad (2.15)$$

where  $E_{i'}$  and  $E_i$  are the respectively the energies of the initial and final states  $\Psi_{i'}$  and  $\Psi_i$  involved in the transition and the energy of the emitted X-ray photon is then given by the difference  $E_{i'} - E_i$ . Just like in the case of Auger electrons, the indexes of the participating states are commonly used to label a particular X-ray fluorescence transition. Both fluorescence and Auger spectroscopy provide information about the elemental composition of the sample and also their chemical environment, as their energies involve transitions between inner shells.

### 2.2.3 Widths and fluorescence yields

An exponentially decaying hole state is found to have a Lorentzian energy profile [21] for which its full width  $\Gamma$  at half maximum (FWHM) is proportional to the total decay rate according to Heissenberg's uncertainty principle,  $\Gamma\tau = \hbar$ . For the case of 1s hole states ( $K$ -level), the width increases monotonically with respect to the atomic number following the approximate relation [32]

$$\Gamma \approx 1.73 Z^{3.93} \times 10^{-6} \text{ eV}. \quad (2.16)$$



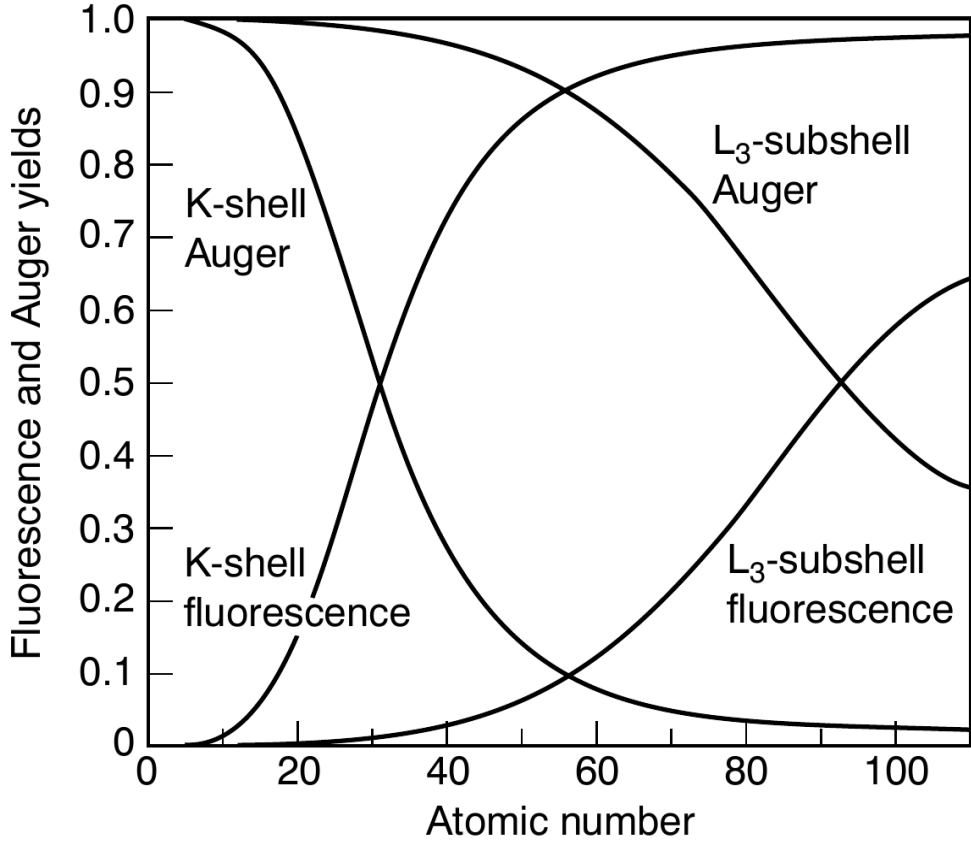


**Figure 2.2:** Fluorescence and Auger yields for K-shell and L<sub>3</sub>-subshell hole states as a function of the atomic number  $Z$ . Taken from [33].

Vacancies located at other levels do not follow such a simple relation and present many sharp discontinuities.

If many decay channels are available, the total width is given by the summation of each partial width

$$\Gamma = \sum_i \Gamma_i, \quad (2.17)$$

including both radiative ( $\Gamma_R$ ) and Auger ( $\Gamma_A$ ) transitions. This defines what is known as fluorescence yield  $\omega_i$  of a given hole state  $i$  as the relative probability to undergo a radiative transition

$$\omega_i = \frac{\Gamma_R(i)}{\Gamma(i)}. \quad (2.18)$$

This definition is quite simple for K-shell vacancies, but higher shells have to take into account the different sub-shells and even intermediate transitions. It can be seen in Fig. 2.2 that the competition between both transitions tends to favor Auger for low  $Z$  atoms, and fluorescence for high  $Z$  atoms. For the particular case of biomolecules, which

constitute an important objective of XFEL studies and are composed mainly by low  $Z$  atoms, Auger decay is the predominant relaxation mechanism.

## 2.3 An Overview of Numerical Methods in XFEL Dynamics

In order to describe the time evolution of the complex systems we are interested in, with all the details of the electronic, ionic and photon dynamics, one should in principle solve the full quantum mechanical many-body problem. This is of course not possible and, depending on the problem at hand, different approximations are required. Many different methods have been developed, with different formalisms and levels of sophistication and we do not aim to describe all of them. Instead, here we discuss briefly some of the methods that are more closely related to the ones used during this work.

### 2.3.1 The Nanoplasma and other Rate Equation Models

The use of a rate equation description can be regarded as the most macroscopic approach among the different available methods, as it describes the system in terms of a set of global variables. The time evolution is described by accounting for the major couplings such as the interactions with the laser field and the internal electronic and ionic processes, in a continuum picture.

One of the first of such formulations was a phenomenological study of the dynamics of a homogeneous cluster under strong-fields known as the nanoplasma model [34]. It assumes that the electrons can be described as a spatially homogeneous plasma with time dependent density, for which the Debye length is smaller than the cluster size. The dynamical degrees of freedom are the number of ions  $N_j$  in the charge state  $j$ , the number of (inner) ionized electrons  $N_e$ , the internal energy  $E_{\text{int}}$  of the electron cloud, and the radius  $R$  of the cluster. The evolution of the ion numbers are then described by [35, 36]

$$\frac{dN_j}{dt} = \Gamma_j N_{j-1} - \Gamma_{j+1} N_j, \quad (2.19)$$

where  $\Gamma_j$  is the ionization rate for ions in charge state  $j$ , accounting for all available channels. The electron number  $N_e$  evolves in turn as

$$\frac{dN_e}{dt} = \sum_j j \frac{dN_j}{dt} - \frac{dQ}{dt} \quad (2.20)$$

where  $Q$  is the total net charge of the cluster. The evolution of the cluster radius  $R$  is described by

$$\frac{\partial^2 R}{\partial t^2} = \frac{5}{R} \frac{p_C + p_H}{\rho}, \quad (2.21)$$

where  $p_C$  is the Coulomb pressure from the net charge and  $p_H$  the thermal pressure of the electron gas (treated as an ideal gas with internal energy  $E_{\text{int}}$ ), while  $\rho$  denote

the mass density of the ions. Finally the internal energy  $E_{\text{int}}$  of the electronic cloud is described as

$$\frac{dE_{\text{int}}}{dt} = F_{\text{abs}} - F_{\text{loss}} - \frac{2E_{\text{int}}}{R} \frac{\partial R}{\partial t} - \sum_j E_{\text{IP}}^j \frac{\partial N_j}{\partial t}, \quad (2.22)$$

where  $F_{\text{abs}}$  is the energy flux into the system from the laser field,  $F_{\text{loss}}$  is the energy flux out of the system due to outer ionized electrons,  $E_{\text{IP}}$  are the ionization potentials, and the radial term accounts for expansion cooling. Depending on the photon energy regime or the specific system the term  $F_{\text{abs}}$  can be modified to include different heating mechanisms. Despite its simplicity the nanoplasma model have been applied to many experimental results with some success, and the original formulation has since expanded in several aspects [37–39].

It has to be emphasized that, as a mean field method, the nanoplasma model can only describe the gross features of the laser interaction and cannot reproduce experimental data beyond average values. The model then fails to explain details of collisional interactions and energy distributions, yet it serves as a good starting point to gain insight into the time evolution of a system.

Rate equations have recently been applied to the multiple ionization problem in rare gas atoms, as well as scattering for carbon [40,41]. In this approach the focus is centered on calculating the time evolution of the probability  $P_K(t)$  of finding an atom with bound electrons in a certain configuration  $K$ . As the pulse interacts with an atom starting in a neutral state with  $Z$  electrons, it will progressively evolve into different configuration with  $Z - 1$  electrons,  $Z - 2$  and so forth, which are in general not unique. As electrons are removed and new configurations are obtained, the electronic orbitals are subjected to an optimization process in order to account for orbital relaxation. The electrons that are either excited or ionized are not taken into account in the electronic configurations.

The time evolution of the populations of different bound configurations are described then as

$$\frac{dP_K(t)}{dt} = \sum_{K' \neq K} [\Gamma_{K' \rightarrow K} P_{K'}(t) - \Gamma_{K \rightarrow K'} P_K(t)], \quad (2.23)$$

where the different rates  $\Gamma$  are, depending of the configuration involved, time dependent photoionization, X-ray fluorescence rates, or Auger decay rates. In calculations with polyatomic systems other channels such as electron impact ionization have to be included. At very high fluences other terms accounting for nonsequential multiphoton processes can also be included.

This rate equation description sometimes fail when resonances with the electromagnetic field are encountered, such as Rabi oscillations between populations of resonantly coupled quantum levels, but it is usually not an important problem in the X-ray regime. For more complex systems like clusters and molecules, the electronic dynamics cannot be simply disregarded and some approaches combining rate equations with molecular dynamics are currently being explored [42].

### 2.3.2 Molecular Dynamics

While mean-field treatments are capable of providing a good description of several systems, the details and mechanisms of the characteristic processes that arise in intense XFEL pulses are quite difficult to elucidate, as large fluctuations are usually involved. In order to microscopically explore these processes an statistical ensemble of trajectories is needed. This surpasses the usual capabilities of the previously described approach, as well as some other popular mean field theories such as hydrodynamic models or density functional methods which, in addition, are usually computationally expensive [35, 36].

In response to this need, classical molecular dynamics have been employed to resolve and describe the many-particle ionization dynamics that lead to highly charged systems and currently it is the only practical solution for many problems. Molecular dynamics simulations simply consist of the numerical solution of the classical equations of motion

$$\begin{aligned}\dot{\mathbf{r}}_i &= \frac{\mathbf{P}_i}{m_i} \\ \dot{\mathbf{p}}_i &= -\frac{\partial H(\{\mathbf{r}_j\})}{\partial \mathbf{r}_i},\end{aligned}\tag{2.24}$$

for which the forces acting on each particle have to be calculated according to the Hamiltonian  $H$  of the system. Some of the most commonly used molecular dynamics approaches may even have been known to Newton [43], yet in the last decades both the increase in the computational capabilities as well as advancements in the understanding of numerical algorithms have made them common tools for research.

The treatment of electrons by molecular dynamics methods gave rise to the development of the key idea of inner and outer ionization [44]. Inner ionization is understood as an excitation of bound electrons that result in a quasi-free particle, not bound to a particular atom but to the system as a whole. Once inner ionized, these electrons are propagated according to classical equations of motion under the influence of the Coulomb interactions, accounting in this way for the many particle correlations and fluctuations in the field. These quasi-free electrons can be heated further reaching the continuum, which is defined as outer ionization.

There are however certain complications that might be circumvented. First, the Coulomb interaction has to be regularized in order to avoid instabilities and numerical artifacts or unphysical bound states. A usual solution to cope with this problem is the introduction of a soft-core potential for the Coulomb interaction

$$W_{i,j}(\mathbf{r}_i, \mathbf{r}_j) = \frac{q_i q_j}{\sqrt{r_{ij}^2 + \alpha}},\tag{2.25}$$

where the smoothing parameter  $\alpha$  provides a cutoff to the interaction [45]. Of course, alternative approaches to (2.25) for the regularization of the potential exist such as the inclusion of short-range repulsions or the attribution of an effective ionic radius. In particular, a different alternative will be introduced in chapter 5, which not only regularizes the potential, but also imposes clear conditions for ionization mechanisms such as electron-impact or field ionization.

A second problem arises in the computational cost from the direct treatment of pairwise interactions, as the calculation of the forces in an  $N$  particle system scales unfavorably as  $N^2$ . For systems beyond a few thousands particles it quickly becomes prohibitive and dedicated algorithms are needed such as hierarchical tree codes or particle in cell (PIC) methods. Such methods allow for the treatment of large systems over long propagation times of the order of hundreds of femtoseconds, while maintaining time steps on the order of attoseconds.



## Chapter 3

# Multiple Ionization in Clusters

In the study of the interaction of finite systems with XFEL pulses one encounters basic phenomena common to all of them, regardless of their specific nature. These common phenomena are mainly the multiple single photon absorption (direct outer ionization) and the gradual creation of a Coulomb potential due to the build-up of the positive charge, whose interplay is the main driver of the dynamics in the X-ray regime.

Particularly interesting conditions are reached when the coulomb potential is deep enough that the direct emission of photoelectrons is no longer possible, which instead gives origin to a nanoplasma (inner ionization). This nanoplasma is not unique to the X-ray regime, as it has been observed multiple times both in the IR and the VUV regime, playing a fundamental role in the energy absorption [35, 36, 46, 47]. However, what truly is unique to X-rays is the highly indirect formation process, as the laser field does not couple directly to the plasma and inverse bremsstrahlung (IBS) is not a relevant mechanism.

The formation phase of this nanoplasma where both inner and outer ionization coexist, and the unexpected consequences it has on the energy spectra of the directly emitted electrons is the topic of this chapter. We start by briefly reviewing recent results regarding direct photoionization frustration as well as the sequential ionization in clusters. This gives a clear insight of not only the systems charge dependence but also the spatial dependence of the electrons energy, and will make both the arising phenomena and the corresponding theoretical treatment clear.

A comparison with numerical dynamics simulations will bring further insight over the relative importance of this effect, and the place it occupies among other simultaneously occurring phenomena such as plasma evaporation. We will then end up with a clear picture and understanding of the systems and how the different parameters affect the observed features.

### 3.1 Frustrated Ionization in Clusters

Atomic clusters occupy a privileged place in the study of the interaction of short intense laser pulses with matter due to their solid-like density without the energy dissipation

channels present in solids. This characteristics make them ideal targets for the study of photoabsorption and ionization in complex systems. In the IR regime for example, experiments with rare-gases clusters have shown a strong laser field coupling with a transient nanoplasma leading to an enhanced energy absorption. The initial field ionization with the subsequent electron impact ionization, along with the plasma electron emission mainly due to IBS gave rise to the concepts of inner and outer ionization [44]. On the other hand, further experiments in the VUV regime, where collective effects start to fade, brought a new discussion over improved IBS models, the barrier suppression phenomena and enhanced-heating through collisions in a transient nanoplasma.

It is therefore no surprise that the advent of XUV and X-ray sources like FLASH, LCLS and SACLA rapidly brought along new experiments with clusters. The first experiments with argon clusters along with Monte Carlo simulations demonstrated the sequential ionization regime [48], where multiple single-photon absorptions induce a highly non-thermal electron energy distribution. These findings motivated further experimentation with xenon clusters as well as the development of the Coulomb Complex model [49, 50], where fast electrons with energies well beyond the excess energy were observed. Theory also demonstrated the existence of a prominent peak near zero energy, which due to experimental limitations could not be initially observed. Both features originate from the equilibration of a very dense nanoplasma trapped by the strong ionic Coulomb potential where the trapped electrons exchange energy through multiple collisions, some of them acquiring very high velocities.

This electron trapping (also referred to as direct ionization frustration) was quickly recognized in several works as responsible of some initial results that seemed at first sight contradictory. For example, measured kinetic energy distributions of fragment ions from Ar clusters in XUV pulses showed mostly single charge states possessing at the same time considerably high kinetic energies [51–53]. Frustrated ionization explains the low charge states as a consequence of the recombination of plasma electrons, transferring more energy to the ions which transiently achieve much higher charge states.

Due to the successful theoretical descriptions of both the prominent peak near zero energy, as well as the plateau observed for sequentially emitted electrons, partially frustrated ionization has attracted not enough attention. Partially frustrated ionization occurs when the system charge is high enough to trap the photoelectrons emitted close to the cluster center, but yet not high enough to trap the photoelectrons emitted from regions close to the surface. This transitional regime is interesting by itself as it deals with slow electrons in a complex system, particularly sensitive to the environment and important in different near-threshold phenomena. Some evidence of the existence of this peculiar regime can be seen for example in Monte Carlo simulations results that show a peak near zero [48] that cannot be explained by plasma relaxations, or the existence of what it appears to be an asymptotic average energy for the emitted photoelectrons [53]. Both results will be clear at the end of the following section.



## 3.2 Analytical Results for Sequential Ionization

The sequential ionization regime is characterized by the fact that between any two consecutive ionization events there is enough time for the previous photoelectron to leave the system, so there is no chance for them to interact directly with each other. In this regime the global phenomena can then be understood by analyzing every single step in the multiple ionization process. The final observables can then be obtained by integrating over all these steps.

Here we analyze a spherical cluster of radius  $R$  which remains constant for the duration of the pulse at every ionization step. As the pulse develops the system gets increasingly charged through the energy absorption from the laser field. For a given charge state  $q$ , and assuming the charge is homogeneously distributed all over the system, the potential inside the cluster takes the form

$$V_q(r) = \frac{3}{2} \frac{q}{R} - \frac{q}{2} \frac{r^2}{R^3}. \quad (3.1)$$

It follows that a photoelectron with excess energy  $\mathcal{E}$  emitted from an ion situated at a distance  $r$  from the center of the cluster would arrive at a detector located far from the system with a final energy  $E$  given by

$$E_q(r) = \mathcal{E} - \frac{q}{R} \left( \frac{3}{2} - \frac{r^2}{2R^2} \right) \quad r \leq R. \quad (3.2)$$

Due to the random nature of the photoabsorption the photoelectron can be emitted anywhere inside the cluster, meaning that for a given charge state  $q$  the energy of the emitted photoelectrons would possess a probability distribution given by

$$P_q(E) = \frac{3}{R^3} \int_0^R dr r^2 \delta(E - E_q(r)) \quad (3.3)$$

which along with (3.2) gives

$$P_q(E) = \begin{cases} \frac{3R}{q} \sqrt{3 - \frac{2R}{q}(\mathcal{E} - E)} & \text{for } E_{\min}(q) \leq E \leq E_{\max}(q) \\ 0 & \text{elsewhere} \end{cases} \quad (3.4)$$

where

$$E_{\min}(q) = \mathcal{E} - 3q/2R \quad (3.5a)$$

$$E_{\max}(q) = \mathcal{E} - q/R. \quad (3.5b)$$

Here  $E_{\min}$  is the energy of a photoelectron originating from the center of the cluster while  $E_{\max}$  is the corresponding energy of a photoelectron originating at the cluster surface.

Additionally,  $P_q(E)$  has to fulfill the normalization condition

$$\int_{E_{\min}}^{E_{\max}} dE P_q(E) = 1 \quad (3.6)$$

which is necessary in order to ensure the increase of the system charge by one unit at each step.

In the sequential ionization regime the final photoelectron spectra can be obtained through the integration of the individual spectra  $P_q$  for each charge state  $q$  from  $q = 0$  (the initial neutral state of the cluster) to the final charge state  $q = Q$

$$P(E) = \int_0^Q dq P_q(E). \quad (3.7)$$

But as equations (3.4) and (3.5) show, the individual  $P_q$  distributions are only defined in a clear interval so we can instead write

$$P(E) = \int_{q_{\min}(E)}^{q_{\max}(E)} dq P_q(E) \quad (3.8)$$

with

$$q_{\min}(E) \equiv \frac{2}{3}(\mathcal{E} - E)R \quad \text{and} \quad q_{\max}(E) \equiv (\mathcal{E} - E)R$$

When the final charge state  $Q$  is such that  $E_{\min}(Q) \geq 0$ , Eq. (3.8) can be integrated analytically [50, 54] to yield

$$P(E) = \begin{cases} 6R\sqrt{3} \left[ \coth^{-1}(\sqrt{\xi}) - \sqrt{\xi} \right] & E_{\min}(Q) \leq E < E_{\max}(Q) \\ 6R \left[ \sqrt{3}\coth^{-1}(\sqrt{3}) - 1 \right] & E_{\max}(Q) \leq E \leq \mathcal{E} \end{cases} \quad (3.9)$$

where

$$\xi = 1 - \frac{2}{3} \frac{R}{Q} (\mathcal{E} - E).$$

While equations (3.9) might perhaps seem complicates, it should be pointed out that for  $E_{\max}(Q) \leq E \leq \mathcal{E}$  that is just a constant value, while for  $E_{\min}(Q) \leq E < E_{\max}(Q)$  it display simply a monotonously increasing behavior.

For a system ionized under these conditions it is quite straightforward to observe that

$$Q = N_{\text{Photons}}$$

that is, the final charge state is equal to the number of photons absorbed by the cluster. This might not be the case when the final charge  $Q$  is high enough that the excess energy

of the photoelectrons is not enough to escape the background potential, as we will see next.

### 3.2.1 Frustrated Sequential Ionization in Clusters

If charging of the system continues, there will be two important moments in the ionization sequence. The first one occurs when a charge  $q_{\text{trap}}$  is reached such that

$$E_{\min}(q_{\text{trap}}) = 0. \quad (3.10)$$

When this state is reached, in every ionization step there is a non-zero probability that the absorbed photon will produce a photoelectron at negative energies that can not escape, and therefore does not increase the charge of the system. The next important step in the ionization sequence occurs when the potential is so deep that not even the photoelectrons produced in the surface have enough energy to escape, and the charging is terminated<sup>1</sup> with a final charge  $Q$ . This occurs when

$$E_{\max}(Q) = 0 \quad (3.11)$$

From Eq. (3.5) we find that

$$q_{\text{trap}} = \frac{2}{3}R\mathcal{E} \quad (3.12a)$$

$$Q = R\mathcal{E}. \quad (3.12b)$$

One immediate consequence of trapping is that  $Q \neq N_{\text{Photons}}$ , as in average more photons are absorbed in order to further increase the charge of the system. This also impacts the spectra  $P_q$  in this region, as the normalization condition (3.6) has to be modified to guarantee the proper charge increase with every step, as follows

$$\int_0^{E_{\max}(q)} dE P_q(E) = 1. \quad (3.13)$$

Applying this normalization condition we obtain

$$P_q^{\text{trap}}(E) = \frac{1}{1 - \left(3 - 2\frac{R\mathcal{E}}{q}\right)^{3/2}} P_q(E) \quad \text{for } 0 \leq E \leq E_{\max}(q_{\text{trap}}). \quad (3.14)$$

The final spectra therefore has to be constructed taking into account this two different and well defined energy regions as can be seen in Fig. 3.1. Depending on the energy, the final spectrum will have contribution from either one or both regions.

Some of the different  $P_q$  contributions can be observed in Figure 3.2 where two different distinctive behaviors are clearly recognizable. As long as  $q \leq q_{\text{trap}}$  each subsequent

---

<sup>1</sup>Strictly speaking the system can and most surely will achieve higher charge states through other mechanisms, like plasma evaporation.

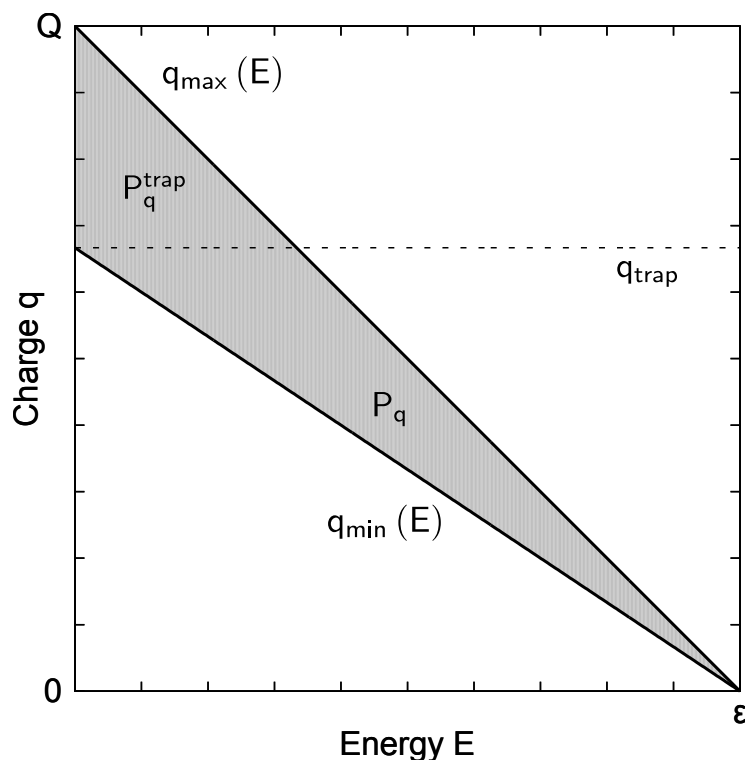


**Figure 3.1:** Sketch of the different regions and quantities influencing the total sequential ionization spectrum of a spherical cluster.

distribution  $P_q$  is defined over a wider energy range with the corresponding lower height, reaching its minimum at  $q_{\text{trap}}$  where the trend is reversed for further charge states, finally diverging at  $E = 0$ . Taking this into account the energy spectra (3.7) can be described as

$$P(E) = \int_{q_{\min}}^{q_{\max}} dq P_q(E) \quad \text{for } \mathcal{E}/3 \leq E \leq \mathcal{E} \quad (3.15a)$$

$$P(E) = \int_{q_{\min}}^{q_{\text{trap}}} dq P_q(E) + \int_{q_{\text{trap}}}^{q_{\max}} dq P_q^{\text{trap}}(E) \quad \text{for } 0 \leq E \leq \mathcal{E}/3 \quad (3.15b)$$

Equation (3.15a) as well as the first term of (3.15b) are identical to (3.9), but the second term of (3.15b) does not allow for a compact analytical solution and has to be integrated numerically.

### 3.2.2 Analytical Approximation for Frustrated Ionization

Interestingly enough the actual shape of the individual  $P_q$  is not the most relevant characteristic for the construction of the final spectrum. As it has been noted for the

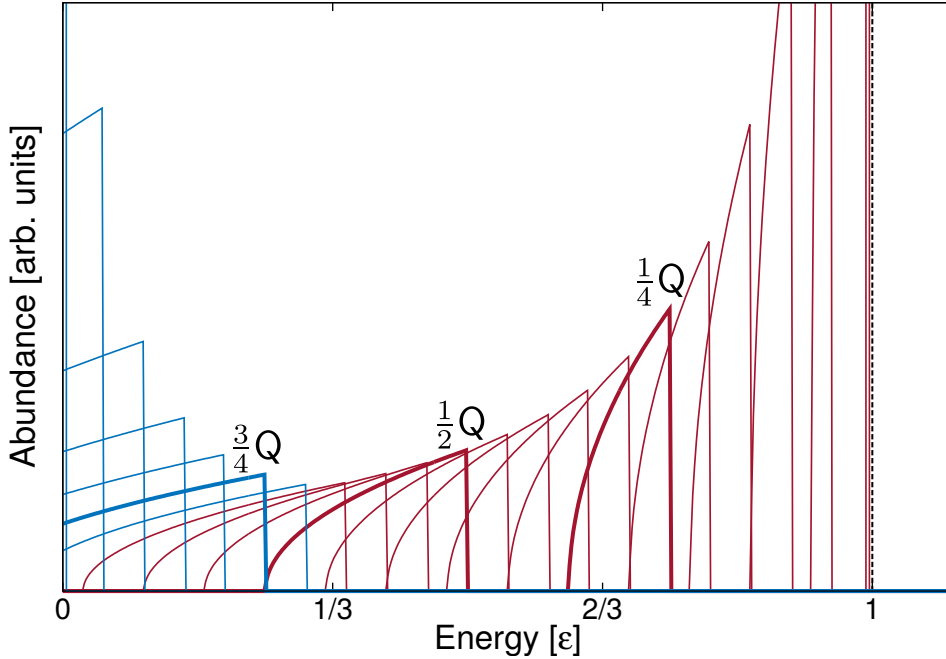


**Figure 3.2:** A collection of different  $P_q$  contributions, for both the regular direct photoelectrons (red) as well as the screened ones (blue). The contributions are highlighted for  $q/Q = 1/4, 1/2$  and  $3/4$ .

case of normal sequential ionization [50], as long as the different contributions  $P_q$  differ only by a simple scaling, the final spectrum will retain the main characteristics. In order to test this assertion and hopefully obtain an analytic form for the spectrum we approximate the  $P_q$  by the simplest possible function, namely a constant spectrum between  $E_{\min}$  and  $E_{\max}$ . The dependence with respect to the instantaneous charge  $q$  comes into play through the normalization condition (3.6). With  $E_{\min}(q)$  and  $E_{\max}(q)$  given by (3.5) this leads to

$$P_q(E) = \frac{1}{E_{\max} - E_{\min}} = \frac{2R}{q} \quad \text{for } 0 \leq q \leq q_{\text{trap}} \quad (3.16a)$$

$$P_q^{\text{trap}}(E) = \frac{1}{E_{\max}} = \frac{1}{\mathcal{E} - q/R} \quad \text{for } q_{\text{trap}} \leq q \leq Q. \quad (3.16b)$$

These distributions allow for the analytic integration of (3.15) as follows

$$P(E) = 2R \ln(3/2) \quad \text{for } \mathcal{E}/3 \leq E \leq \mathcal{E} \quad (3.17a)$$

$$P(E) = 2R \ln\left(\frac{\mathcal{E}}{\mathcal{E} - E}\right) + R \ln\left(\frac{\mathcal{E}}{3E}\right) \quad \text{for } 0 \leq E \leq \mathcal{E}/3 \quad (3.17b)$$

A comparison between the numerically integrated original spectra from Eq. (3.15) and the analytical results from Eq. (3.17) is shown in Figure 3.3, where a remarkably

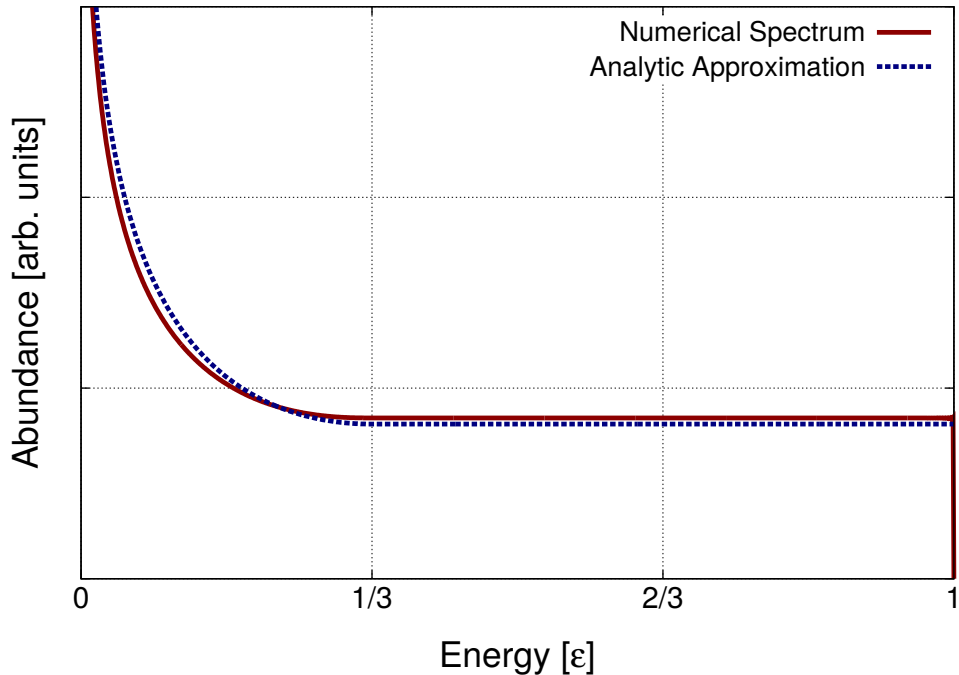


**Figure 3.3:** Comparison of the final spectrum obtained by numerical integration of Eq.(3.15) (red) as well as the one obtained from the analytical approximation (3.17) (navy-blue).

good agreement can be observed. The analytic form reproduces the behavior in both regions, showing a plateau for  $E \geq \mathcal{E}/3$  and the divergence around  $E = 0$ .

While these results look promising and seem to capture the essence of some previously observed results [48, 53], being derived in the sequential ionization framework might put its validity into question. After all, while sequential ionization assumes the complete absence of interaction between emitted electrons, the presence of system bound electrons certainly implies the possibility of such interactions. Furthermore the trapped electrons form a nanoplasma which can thermalize [49] emitting electrons and reaching charge states higher than  $Q$ . It is therefore necessary to determine if and when are this assumptions valid.

### 3.3 Coulomb Complex Study

A molecular dynamics study (MD) is necessary to asses the validity of the previous results as it does not rely on the simplifying assumptions of sequential ionization and perfect screening of trapped electrons. The MD calculations simulate the more complex electronic dynamics and interactions, naturally including the effects of the well-known plasma thermalization through electron collisions. The Coulomb complex model is a particularly suitable framework for the present case, due to its simple implementation and numerical efficiency. It also captures the main phenomena involved, which is the

repulsive interaction between electrons (here regarded as classical point particles) and an attractive potential  $V_Q$

$$V_Q(r) = \begin{cases} \frac{Q}{2R} \left( \frac{r^2}{R^2} - 3 \right) & \text{for } r \leq R \\ -\frac{Q}{r} & \text{for } r > R \end{cases} \quad (3.18)$$

due to the ions, also known as jellium potential.

The initial electronic configuration is numerically obtained by assuming  $N$  electrons inside the corresponding potential, and propagating them according to the full Hamiltonian

$$H = \sum_{i=1}^N \left( \frac{\mathbf{p}_i^2}{2} + V_Q(r_i) \right) + \sum_{i<j}^N \frac{1}{|\mathbf{r}_i - \mathbf{r}_j|} \quad (3.19)$$

while reducing the particle velocities by a factor (typically 0.5) which allows for the particles to reach a minimum energy configuration. In this minimum energy configuration, the binding energy or ionization potential ( $E_b$ ) of each electron can be calculated by

$$E_{b,i} = V_Q(\mathbf{r}_i) + \sum_{i<j}^N \frac{1}{|\mathbf{r}_i - \mathbf{r}_j|}. \quad (3.20)$$

Interestingly, the individual electron binding energies so calculated do not vary significantly and a shell structure is obtained [54]. Upon absorption of a photon, the magnitude of the initial momentum  $p_0$  for each electron is determined by

$$p_{0,i} = \sqrt{2(\mathcal{E} - E_{b,i})} \quad (3.21)$$

while the direction is chosen randomly according to an isotropic distribution.

In order to determine the different activation times a Gaussian temporal profile is assumed for the XFEL beam, that is

$$I(t) = I_0 \exp \left( -4 \ln 2 \left( \frac{t}{T} \right)^2 \right) \quad (3.22)$$

where  $T$  is the full-width at half-maximum. Assuming the system only interacts with the electric field via single-photon absorption, the absorption rate is proportional to the intensity of the pulse and the total cross-section. That is

$$\frac{dn_e}{dt} = N(t)\Gamma(t) \quad (3.23a)$$

$$\Gamma(t) = \frac{\sigma_\omega I(t)}{\hbar\omega} \quad (3.23b)$$

where  $N(t)$  and  $n_e(t)$  are respectively the number of non-activated and activated electrons at time  $t$  and  $\sigma_\omega$  is the photoabsorption cross-section of the constituent atoms in the

cluster at photon frequency  $\omega$ . This process defines a probability for a photoionization event happening during a time interval  $\Delta t$  by [55]

$$p_{\text{abs}}(t) = N(t)\Gamma(t)\Delta t \quad (3.24)$$

which through a Monte Carlo calculation defines the ionization events along the time evolution.<sup>2</sup>

All the electrons remain at their initial positions before activation. As the pulse develops the first electron is activated with an initial energy equal to the excess energy  $\mathcal{E}$ . For the subsequent activated electrons, their energy decreases as the previously activated electrons leave the system. The energy of the activated electrons will therefore start with an energy  $E_i^0 \leq \mathcal{E}$  and eventually for a sufficient number of activated electrons  $E_i^0 < 0$ . The initial energy of an electron at its activation time can be utilized to distinguish between direct photoelectrons ( $E_i^0 \geq 0$ ) and plasma electrons ( $E_i^0 < 0$ ).

Once activated the electrons are propagated classically according to Newton's equations with the corresponding forces exerted by the positive jellium potential (3.18) and the electron-electron interactions. In this way the correlations (collisions) of the electrons are fully taken into account, making it possible for plasma electrons to thermalize and leave the system. The system is propagated for a sufficiently long time (on the order of  $t = 10^4$ ) before the spectra is calculated, taking into account multiple realizations (typically 100). It is worth noticing that the calculations presented in this chapter are done in an arbitrary unit system and other conditions can be reached by applying the following scaling according to [54]

$$\{\mathbf{r}, \mathbf{p}, \mathcal{E}, t\} \rightarrow \{\eta^{-1}\mathbf{r}, \eta^{1/2}\mathbf{p}, \eta\mathcal{E}, \eta^{3/2}t\}.$$

Nevertheless, it should be emphasized that this scaling only applies for systems with the same number of activated electrons.

The resulting spectra of one of such simulations is shown in Fig. 3.4, where both the total spectrum as well as the contribution due to the directly emitted photoelectrons are shown. The low energy peak is clearly visible in the direct photoelectron contribution (defined as those outer ionized directly by a photon absorption) as it is expected from our previous results. It is also clearly visible that in this low energy region there is simultaneously a contribution from the evaporation of nanoplasma electrons which, at a first glimpse at least, seem to behave in a relatively similar way.

We still need to address the question of how well the analytic expression (3.17) describes the spectrum contribution of the directly emitted photoelectrons. While the answer is quite simple, it is not completely obvious, due to the dependence of this effect on different parameters. We exemplify this in Fig. 3.5 for three different scenarios where, for the sake of clarity, only the direct emission contribution is shown.

Probably the most dramatic difference with respect to the analytic result can be observed in 3.5(c), where the low energy peak is suppressed considerably for long pulses.

---

<sup>2</sup>There exist alternative approaches for the determination of the activation times [54], but Eq. (3.24) can be readily implemented in more complicated scenarios and will also be used in upcoming chapters.



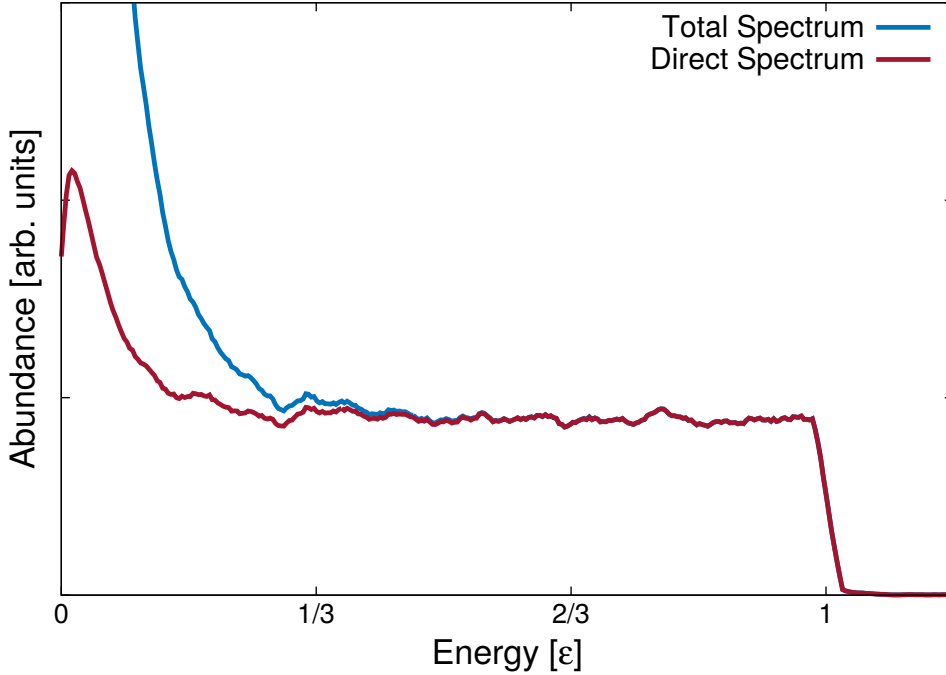


**Figure 3.4:** Electron energy spectra calculated for a Coulomb complex of radius  $R = 10$ , with an excess energy  $\mathcal{E} = 40$  and a number of atoms  $N = 1000$ . For a Gaussian pulse with  $T = 2$  and peak absorption rate  $\Gamma = 1$  the average charge accounts for  $q = 0.882$ . The full spectrum is shown (blue) as well as the spectrum from direct electrons (red).

This suppression is due to the fact that during the activation stage there is enough time for some of the plasma electrons to collide and obtain sufficient energy to escape, contributing to the further charging of the system. The plasma electrons evaporate with a rate that depends on the electron density [49] and therefore, on the cluster size and the total amount of trapped electrons.

One might be tempted to propose that, in order to suppress the additional charging from plasma electrons, shorter pulses should be used in order to increase the agreement with our analytical estimate. This is partially true as we can observe already an almost perfect agreement in 3.5(b) but for the shortest pulse in 3.5(a) we observe that the direct photoelectron contribution obtained numerically by MD actually exceeds our analytical estimation. The reason behind this is that for very short pulses we start leaving the sequential ionization regime, as the photoabsorption rate is so high that the photoelectrons can interact and exchange energy before leaving the cluster, which occurs in what is known as massive parallel ionization [56]. Evidence for the onset of this regime can be observed in the formation of the characteristic high energy tails above the cutoff at  $E = \mathcal{E}$ .

We can conclude that the comparison between fully numerical spectra obtained by MD, as particularly observed in the photoelectron contribution, shows that the low-energy peak routinely observed in the electron energy spectrum of cluster XFEL studies

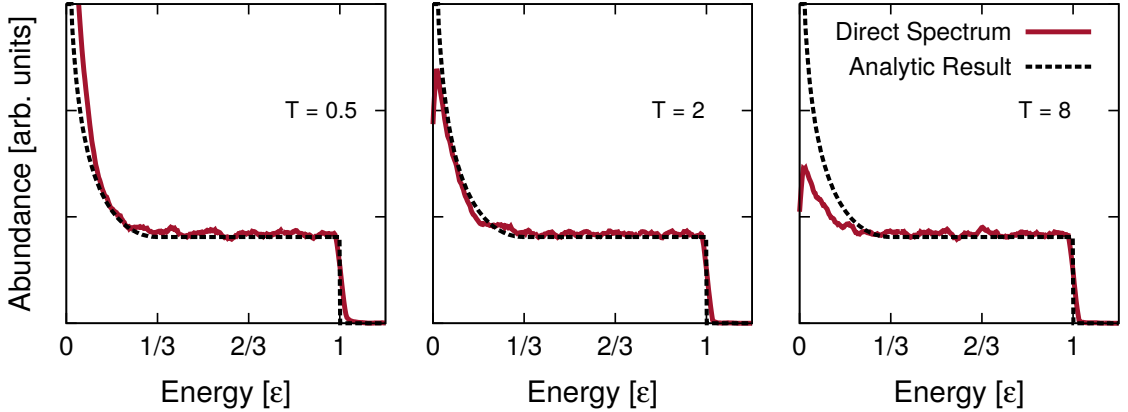


**Figure 3.5:** Numerical electron energy spectra (red solid) of the direct photoelectrons, obtained from Coulomb complexes with  $R = 10$ ,  $N = 1000$ ,  $\mathcal{E} = 40$ , and a Gaussian pulse with  $\Gamma = 5$  for different pulse lengths. Alongside is shown the analytical approximation (black dashed line) for comparison.

is not only generated by plasma evaporation. The origin of the low-energy peak for sequentially emitted photoelectrons is correctly understood and under certain parameter conditions precisely described by the analytic results previously obtained.

### 3.4 Plasma Formation in Sequential Ionization

While for the time being our attention has been focused almost exclusively on the study of the sequentially emitted direct electrons, we have observed that the trapped plasma electrons also play an important role. This is true not just only because the sequential energy peak is created precisely due to the existence of bound plasma electrons, but also because the contribution that the evaporated plasma electrons have in the energy spectra might have prevented the identification of said peak in previous experiments. Besides, our Coulomb complex study has shown that plasma electron evaporation can suppress the formation of the sequential peak, and while this can be mitigated by the use of shorter pulses, this brings along new issues as we leave the sequential ionization regime. In order to find alternative strategies it is therefore necessary to gain more insight into the plasma formation.

In order to assess the relative importance that the plasma electrons could have in the spectra, it is necessary to determine both the total number of plasma electrons and photoelectrons. This would help us to understand which parameters contribute to the appearance of slow electrons from plasma evaporation. In Fig. 3.6 we can observe that along the two regions contributing to the sequential spectrum,  $q_{\min}(E)$  also defines a third region for negative energies, where the absorption of a photon creates a bound plasma electron ( $n_{\text{pl}}$ ). To maintain the following discussion as clear as possible, it is useful to classify the number of photoelectrons ( $n_{\text{ph}}$ ) according to the two regions that define their  $P_q$  distributions. In this way we define the number of direct photoelectrons

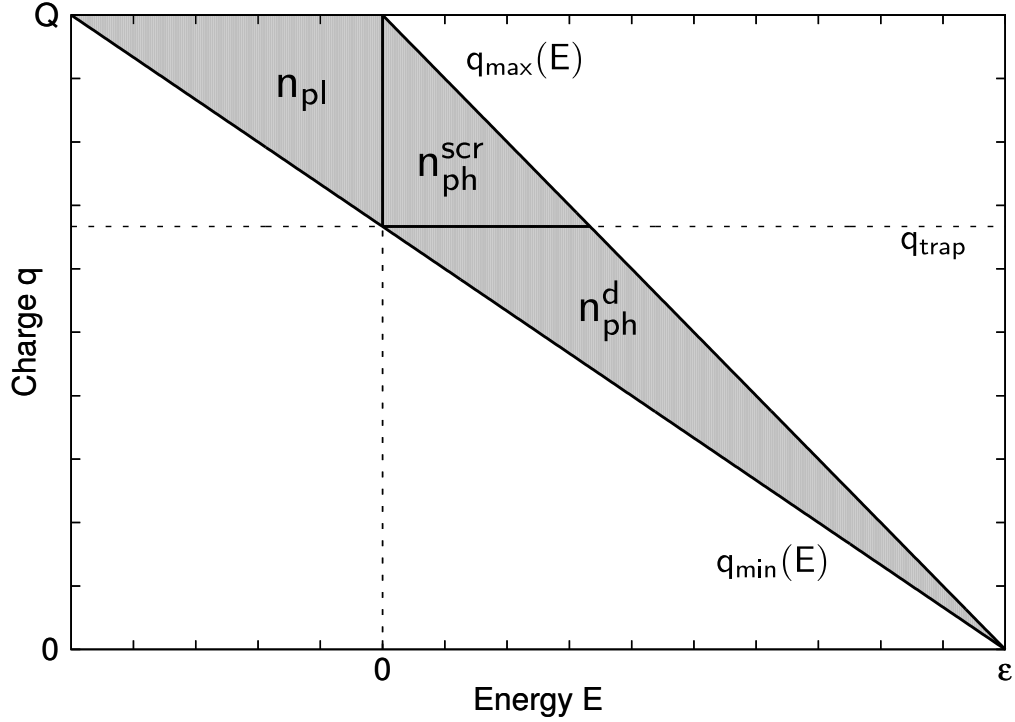


**Figure 3.6:** Sketch of the different regions and quantities that define the number of electrons involved in the sequential ionization process. Photons absorbed by electrons in positive energy regions contribute to the number of photoelectron ( $n_{\text{ph}}$ ), while those absorbed at negative energies contribute to the plasma ( $n_{\text{pl}}$ ).

( $n_{\text{ph}}^{\text{d}}$ ) as those emitted from charge states  $q \leq q_{\text{trap}}$ , and the number of screened photoelectrons ( $n_{\text{ph}}^{\text{scr}}$ ) as those emitted from charge states  $q \geq q_{\text{trap}}$ . The only difference resides in the fact that the creation of a screened photoelectron implies the creation of plasma electrons and otherwise all photoelectrons are identical in nature.

The total number of photoelectrons  $n_{\text{ph}}$  can be easily calculated from the photoelectron spectra as follows

$$\begin{aligned}
 n_{\text{ph}} &= \int_0^{\varepsilon} dE P(E) = \int_0^{\varepsilon} dE \int_0^Q dq P_q(E) \\
 &= \int_0^Q dq \int_0^{\varepsilon} dE P_q(E) = \int_0^Q dq = Q
 \end{aligned}$$

where the normalization condition (3.13) allows us to trivially solve the integral. Unsurprisingly we found that the charge  $Q$  obtained by sequentially ionizing the system is equal to the number of photoelectrons that can escape. Furthermore, as  $Q = q_{\text{max}}(0)$ , it follows from (3.5) that

$$n_{\text{ph}} = R\mathcal{E}. \quad (3.25)$$

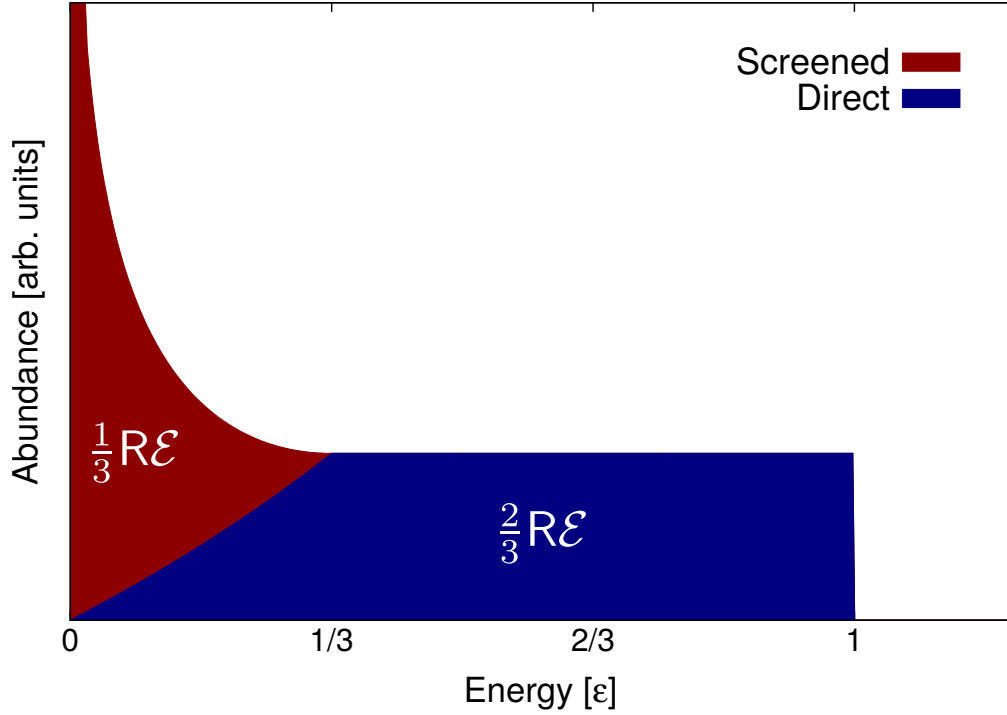


**Figure 3.7:** Contribution of direct electrons (navy-blue) and screened direct electrons (red) in the sequential ionization spectrum.

We quite naturally find that bigger clusters and higher excess energies allow the escape of more photoelectrons. Following the exact same procedure with the appropriate integration limits, using the fact that  $q_{\text{trap}} = 2Q/3$ , we easily find

$$n_{\text{ph}}^{\text{d}} = \frac{2}{3} R\mathcal{E} \quad (3.26a)$$

and

$$n_{\text{ph}}^{\text{scr}} = \frac{1}{3} R\mathcal{E}. \quad (3.26b)$$

Nowhere in the previous derivation of these quantities the particular shape of  $P_q$  was needed, and no approximation has been made. The screened and direct photoelectrons are shown in Fig. 3.7, where both fractions were obtained using the approximated rectangular distributions (3.16) for the different  $P_q$  contributions.

In order to determine the plasma electrons we have to clarify that the distributions  $P_q$  determines the probability of a photon being absorbed by a spherical cluster with charge state  $q$  ionizing an electron with energy  $E$ . For  $E > 0$  this event leads to outer ionization, increasing the charge of the system. For charge states  $q \geq q_{\text{trap}}$ , while the outer ionization requires the normalization condition (3.13) in order to increase the system charge, the distribution  $P_q$  still describes the probability of absorption, being defined over the interval  $[E_{\text{min}}(q), E_{\text{max}}(q)]$  and reaching negative energies (Eq.(3.5)). The photoabsorption by electrons with negative energies causes an inner ionization event,

and contributes to the plasma formation. As  $P_q$  is still defined at negative energies, we recognize with the help of Fig. 3.6 that

$$n_{\text{pl}} + n_{\text{ph}}^{\text{scr}} = \int_{-\frac{1}{2}\mathcal{E}}^{\mathcal{E}} dE \int_0^Q dq P_q^{\text{trap}}(E), \quad (3.27)$$

where we have used (3.5) to determine  $E_{\text{min}}(Q) = -\frac{1}{2}\mathcal{E}$ . We must emphasize that  $P_q^{\text{trap}}$  is essentially the same as in (3.14) with the exception that it is now also defined for negative energies.

As we already determined  $n_{\text{ph}}^{\text{scr}}$  in (3.26), only the integral on the right is needed to determine  $n_{\text{pl}}$ . Unfortunately the integrand diverges as  $q \rightarrow Q$ , and a different approach is needed. For this we rely once again in the approximation with rectangular distributions (3.16) and on the fact that the charge increase occur in unit steps, which allows for a discrete formulation of the integral (3.27). Then, for a given charge state  $q$  such that  $q_{\text{trap}} < q \leq Q$ , we have the following rectangular distribution

$$P_q^{\text{trap}}(E) = \frac{R}{R\mathcal{E} - q} \quad \text{for} \quad E_{\text{min}}(q) \leq E \leq E_{\text{max}}(q). \quad (3.28)$$

Thus, the number of plasma electrons<sup>3</sup>  $n_{\text{pl}}^q$  created in the charge step  $q$  is

$$n_{\text{pl}}^q = \int_{E_{\text{min}}}^0 dE \frac{R}{R\mathcal{E} - q} \quad (3.29a)$$

$$\begin{aligned} &= -\frac{R}{R\mathcal{E} - q} E_{\text{min}}(q) \\ &= \frac{q}{2(Q - q)} - 1, \end{aligned} \quad (3.29b)$$

where we have used Eq.(3.12) in the last step. To obtain  $n_{\text{pl}}$  we only need to sum over all the pertinent charge states  $q$ , starting from  $q = q_{\text{trap}}$  and finalizing at  $q = Q - 1$ . This final charge state is necessarily defined in this way as any state for which  $q \geq Q$  produces an ill-defined distribution  $P_q$  which diverges or is negative valued (3.28). From a physical point of view, in the sequential ionization regime it makes no sense to include states that cannot possibly be reached through this process. Therefore the number of plasma electron reads

$$n_{\text{pl}} = \sum_{q_{\text{trap}}}^{Q-1} \left( \frac{q}{2(Q - q)} - 1 \right), \quad (3.30)$$

---

<sup>3</sup>The number of plasma electrons calculated this way is not independent of the shape of  $P_q^{\text{trap}}$ , and the use of (3.16) systematically overestimates  $n_{\text{pl}}$  with respect to the actual distribution (3.14), which has to be kept in mind.

which can be written in a simpler form by acknowledging that  $q_{\text{trap}} = 2Q/3$ , and introducing an index change by  $i = Q - q$  as

$$\begin{aligned} n_{\text{pl}} &= \sum_{i=1}^{Q/3} \left( \frac{Q}{2i} - \frac{3}{2} \right) \\ &= \frac{Q}{2} \sum_{i=2}^{Q/3} \left( \frac{1}{i} \right). \end{aligned} \quad (3.31)$$

The number of plasma electrons is then simply defined by a harmonic progression starting at  $i = 2$ . While this harmonic progression does not have an exact compact formulation, it can be approximated by an integral as follows

$$\begin{aligned} \sum_{i=2}^{Q/3} \left( \frac{1}{i} \right) &\approx \int_2^{Q/3+1} dx \frac{1}{x - 1/2} \\ &\approx \ln \left( \frac{2}{9}Q + \frac{1}{3} \right). \end{aligned} \quad (3.32)$$

Substituting this result into (3.31) finally gives the following expression

$$n_{\text{pl}} = \frac{Q}{2} \ln \left( \frac{2}{9}Q + \frac{1}{3} \right), \quad (3.33)$$

which has a somewhat surprising functional form, specially when compared to the simple linear dependence of the expressions (3.26) for the photoelectrons. We also find that the photoelectrons and plasma electrons depend exclusively on one parameter  $Q = R\mathcal{E}$  which means that for any cluster of any size, we can choose an excess energy  $\mathcal{E}$  such that the exact same number of photoelectrons and plasma electrons are created (for the sequential regime).

As we show both the plasma electrons  $n_{\text{pl}}$  and the photoelectrons  $n_{\text{ph}}$  in Fig. 3.8(a) we observe an even more interesting fact, that is an offset in  $n_{\text{pl}}$ , as no plasma electrons are created for  $Q \leq 3$ . This can be understood as a consequence of equations (3.26) and (3.27), as for the case with  $Q = 3$  photoelectrons only one  $n_{\text{ph}}^{\text{scr}}$  photoelectron is created, whose distribution  $P_3$  is defined in the interval  $[0, \frac{1}{3}\mathcal{E}]$  without going into negative energies, thus not creating along a plasma electron.

As the value of  $Q$  increases (that is, for either bigger clusters and/or higher excess energies) the number of plasma electrons start to slowly increase at first until for a value of  $Q \approx 32$  the number of plasma electrons equals the number of photoelectrons. For that point onwards the plasma population takes over and increases in an ultimately almost linear fashion. However, this increase does not result in a quick domination of the plasma electron population, as the fraction of plasma electrons increases very slowly by comparison (Fig. 3.8(b)).

According to this results we could suggest that using either lower excess energies and/or clusters of smaller dimensions would reduce both the total number of trapped

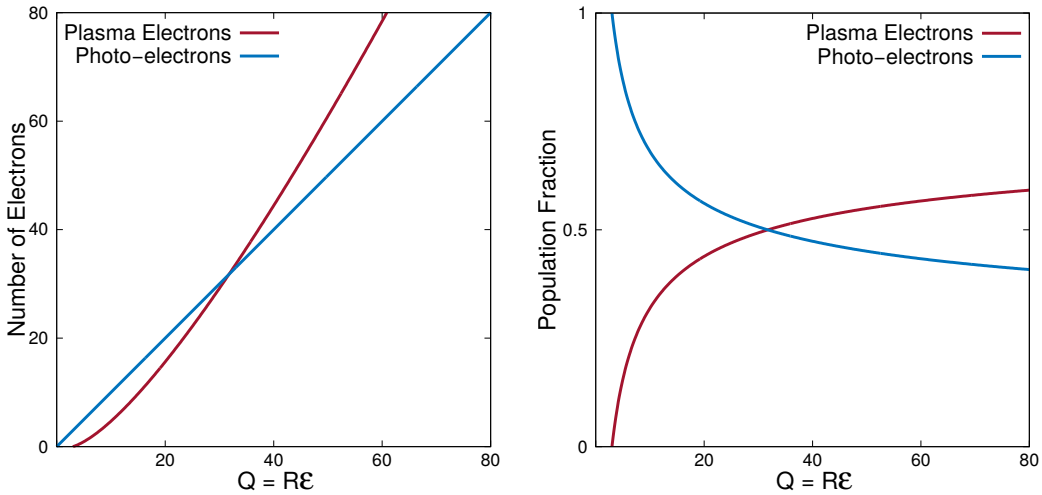


**Figure 3.8:** (a) Number of Photo-electrons (blue) and Plasma Electrons (red) with respect to the final charge  $Q$  obtained by sequential ionization. (b) Corresponding fractions of electron populations with respect to  $Q$ .

plasma electrons as well as their relative abundance with respect to the photoelectrons. In this way it would be natural to expect that the suppression of the low energy peak in the photoelectron spectrum would be diminished, as well as the relative contribution of the plasma electrons to the total spectrum. This certainly holds true for the excess energy, but numerical simulations with the same excess energy but different cluster sizes tell a different story. The results of this simulations are shown in Fig.3.9, where in order to make an useful comparison the ration  $q/R$  was kept constant, where  $q$  is the number of activated electrons. There we can appreciate that smaller systems suffer a stronger suppression of the low energy peak, suggesting that for smaller systems plasma evaporates faster even if fewer plasma electrons are present. Even more surprising is the trend we observe in the plasma electrons, as the plasma contribution actually increases for smaller clusters despite the fact that the relative plasma population is exactly the same.

This seemingly counter intuitive result has however a very simple explanation. While the number of plasma electrons certainly affects the plasma dynamics, the key parameter is the plasma electron density. The collision probability, and therefore the evaporation rate, depends on the density and it has also been previously described [49] that the average energy of the exponential plasma contribution scales proportionally to  $\rho^{1/3}$ . From equation (3.33) we can immediately obtain the electron plasma density as follows

$$\rho(\mathcal{E}, R) = \frac{3\mathcal{E}}{8\pi R^2} \ln \left( \frac{2}{9} R\mathcal{E} + \frac{1}{3} \right). \quad (3.34)$$

One important remark is that while the electron numbers  $n_{\text{ph}}$  and  $n_{\text{pl}}$  are functions of one single parameter  $Q$ , this no longer is the case for the electron plasma density and it depends on the excess energy and the cluster radius in a less trivial way.

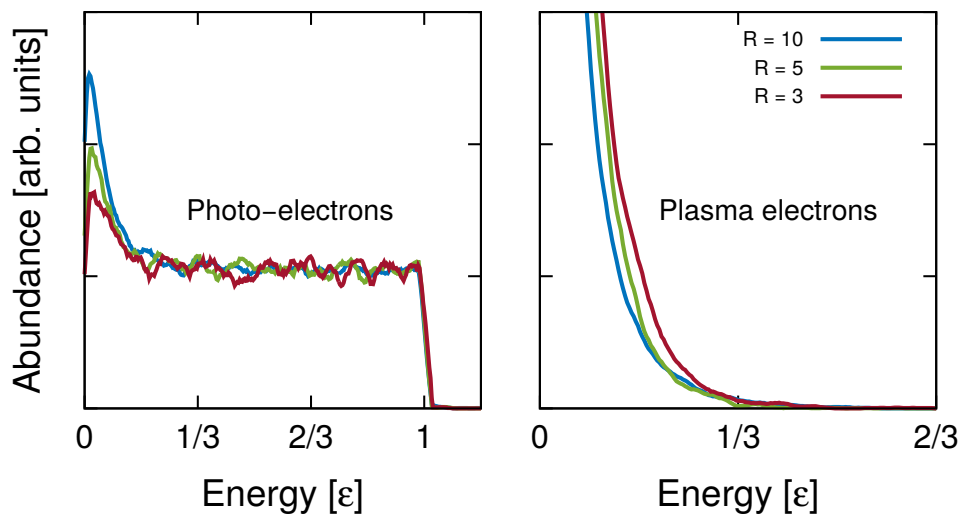


**Figure 3.9:** Numerical electron energy spectra for photoelectrons (left) and plasma electrons (right) for spherical clusters of different sizes. The excess energy is  $\mathcal{E} = 40$ , the pulse length  $\tau = 2$ , and  $q/R = 90$  for all cases

The electron plasma density is shown in Fig. 3.10 as a color map. Here we observe that indeed, for a fixed value of  $R$ , as higher excess energies imply a higher number of plasma electrons, this gets reflected in a higher plasma density. On the other hand, while a higher cluster size implies a bigger number of trapped plasma electrons, this does not get reflected into higher plasma densities. This means that for bigger systems and lower excess energies, the plasma evaporation will occur less rapidly and the low energy peak of the sequential photoelectrons would develop in a less disturbed way even for longer pulses.

### 3.5 Conclusions

It has been shown both analytically and numerically that the low-energy peak commonly encountered in the electron energy spectrum of clusters exposed to strong X-ray pulses is not only generated by the evaporation of the initially trapped plasma electrons, but also contains a contribution from direct photoelectrons. The analytical formulation of the energy spectrum in the sequential ionization framework provides a correct understanding of the origin of this low-energy peak and a fully analytic approximation was obtained. The numerical simulations with Coulomb complexes provide further understanding of the interplay between direct photoelectron emission and plasma evaporation, as well as the parameters involved.

We extended the sequential ionization framework to study the plasma formation, being able to calculate the number of plasma electrons that are created as the sequential ionization takes place. By doing so, it was possible to identify how the system size and the excess energy influence the plasma evaporation rate.



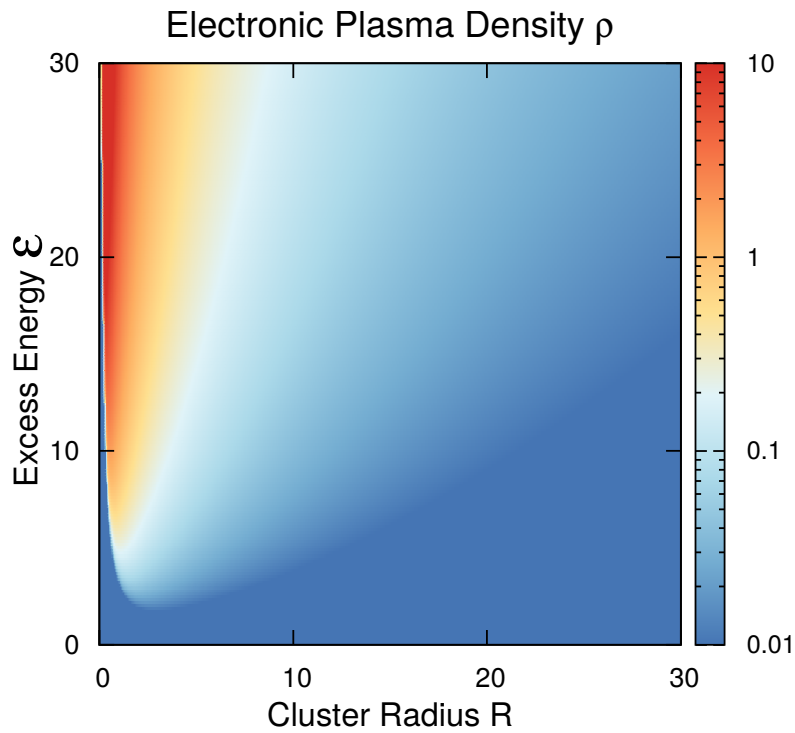


**Figure 3.10:** Contour plot showing the plasma electron density as a function of the cluster radius  $R$  and the excess energy  $\mathcal{E}$ .

An open question still remains on whether it is possible to disentangle the direct photoelectron dynamics from the plasma dynamics experimentally, as both naturally overlap in the energy spectra. Our understanding of the plasma density, and the dependence with respect to parameters easily controlled in the experiments, such as the laser wavelength and intensity as well as the cluster size, might allow for new experimental schemes were this could potentially be achieved.



## Chapter 4

# Multiple Channel Ionization and Ionic Motion

In the previous chapter we gained significant understanding over how multiple ionization of finite systems and the consequent formation of a strong background potential gets reflected in the broad electronic energy spectrum, as well as the role played by trapping and screening. Many systems of interest however, such as big polyatomic molecules and aggregates of biological importance, present a more complex behavior when exposed to short and intense XFEL pulses. These systems are prototypical examples of a many-body problem and, when a laser field is present, the different electronic and nuclear degrees of freedom are all potentially coupled together in ways far from trivial.

In the X-ray regime the multiple photon absorption does not only create photoelectrons and a transient nanoplasma, it also enables new ionization channels, either as one of the many autoionization processes or by multiple photoabsorption by a single atom. The later process has gained considerable attention lately due to the possibility of the creation of exotic and highly excited ionic double core-hole states, enabled just recently in molecules by XFEL pulses [30, 31, 57]. Autoionization processes on the other hand, typically involving many degrees of freedom, can be responsible of electron emission in different time scales. The resulting electron energy spectra therefore includes contributions from all of these different channels, presenting more complicated structures and making interpretation a difficult task.

Furthermore, ionic movement can now play an important role as the availability of more ionization channels means that higher charge states can be reached by the ions, inducing a stronger and faster displacement that can have an important impact over different time scales.

As we approach this problem, it is then desirable to study a molecule that exhibits all the previous features but at the same time allows for simplifications, perhaps based on its structure. With this in mind the fullerene  $C_{60}$  is an ideal system, as it is composed of 60 identical carbon atoms localized in a spherical shell at the exact same distance from the molecular center (3.5 Å). This symmetry allows us to get rid of the spatial dependence of the potential and focus exclusively on the interplay of different ionization

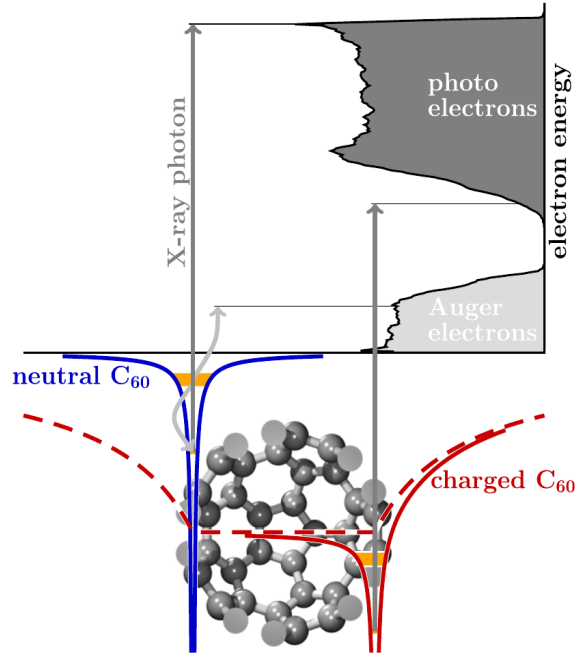


**Figure 4.1:** Sketch of the formation of a broad electron energy spectra in polyatomic molecules. The highest energy is observed for the photoionization of a core electron from neutral C<sub>60</sub> (blue line). As the C<sub>60</sub> gets charged (red solid line), the energy is reduced due to the background potential (dashed red line).

mechanisms.

Despite its apparent simplicity the fullerene C<sub>60</sub>, since its discovery [58], has become a poster molecule for physicists and chemists alike. Indeed this molecule is often used in the investigations of light induced dynamics in complex molecules thanks to its very unique and interesting properties [59,60]. This molecule satisfies all our requirements, as it undergoes ionization both by photoabsorption as well as by Auger decay, providing many potentially coupled channels.

In this chapter we tackle the complicated multi-channel ionization dynamics of C<sub>60</sub> in gas phase, progressively gaining insight by starting with a very simplified scenario for which only two different channels are allowed and no ionic motion is present. The knowledge obtained will prove useful as we later allow for all possible transitions and charge states to occur until we finally end up with a full calculation including ionic motion. In this way it will be possible to disentangle the role of the different mechanism and identify their particular signatures in the final electronic spectra and some of their experimental implications.

We will finish by exploring briefly some intriguing possibilities that the different ionization processes with their different time scales entail, and the information that can potentially be extracted about the electronic structure and ionization processes.

## 4.1 Rate Equation Description of Multi-channel Ionization

As a first step in our effort to understand the multi-channel ionization of fullerenes we make use of rate equations, which share in their mathematical structure several similarities with the sequential ionization shown in the previous chapter. In this framework, if an electron is emitted from a system with a time-dependent ionization rate  $\dot{n}(t)$ , the energy spectrum of that electron is given by an integral over emission times as [61]

$$P(E) = \int dt \dot{n}(t) \delta(E - E'(t)), \quad (4.1)$$

where  $E'(t)$  is the final energy of an electron released at time  $t$  through a well defined ionization process (or channel). If the final energy is not time-dependent, the spectrum  $P(E)$  would only consist of a sharp peak at  $E'$ , as it occurs in the normal gas phase spectroscopic measurements. In XFEL experiments, however, the energy  $E'$  can strongly depend on time as the background potential might change dramatically as the system gets charged, in which case the spectrum  $P(E)$  will be defined over a broad energy range.

If the system can emit electrons through different channels  $i$ , the electron energy spectrum has to include the contributions from all of them

$$\begin{aligned} P(E) &= \sum_i \int dt \dot{n}_i(t) \delta(E - E'_i(t)) \\ &= \sum_i \left. \frac{\dot{n}_i(t)}{\dot{E}'_i(t)} \right|_{t=t'_i(E)}, \end{aligned} \quad (4.2)$$

where  $\dot{n}_i(t)$  and  $E'_i(t)$  are, respectively, the ionization rate and the final energy of the channel  $i$ , and  $t'_i(E)$  is the inverse function of  $E'_i(t)$ . Equations (4.1) and (4.2) clearly share similarities with (3.2) and (3.7) from sequential ionization, yet there are important conceptual differences. First of all, here we explicitly allow for the possibility to emit an electron simultaneously from more than one channel yet we assume that any interaction between them is negligible. But the most important difference is that all the different energies  $E_i(t)$  (and therefore the individual contribution to the spectrum) are coupled together through the Coulombic background potential. Furthermore, as different ionization processes can appear sequentially, the ionization rates  $\dot{n}_i(t)$  can themselves be coupled as we will see.

In the case of  $C_{60}$ , and for the time being, we assume that any charge is homogeneously distributed over a sphere of radius  $R$  so the final energies can be computed as<sup>1</sup>

$$E_i(t) = \mathcal{E}_i - V(t) \quad (4.3a)$$

$$V(t) = \frac{q(t)}{R}, \quad q(t) = \sum_i n_i(t), \quad (4.3b)$$

---

<sup>1</sup>In the case of the fullerene  $C_{60}$ , the correlation hole effect [62] defines an effective radius  $R = \alpha R_F$ , where  $\alpha \approx 1.14$ , and  $R_F = 3.5 \text{ \AA}$  is the actual molecular radius.

where  $\mathcal{E}_i$  are the excess energies for an electron emitted by means of the process  $i$  from a single carbon atom or ion. For a molecule interacting with X-rays the main ionization processes available can be divided into photoionization and autoionization. In the case of photoionization, this process involves one single electron from any energetically allowed shell, and the excess energy  $\mathcal{E}_i^{\text{ph}}$  of the channel  $i$  can be calculated as follows

$$\mathcal{E}_i^{\text{ph}} = E_\omega - E_{\text{b},i}, \quad (4.4)$$

where  $E_\omega$  is the photon energy, and  $E_{\text{b},i}$  is the corresponding binding energy of the electron. In contrast, for an autoionization process to take place typically two or more electrons are required, and the characteristic excess energy depends exclusively on the initial and final electronic states of the ion from which the electron is ejected. This means that for an autoionization process  $i$ , its excess energy  $\mathcal{E}_i^{\text{a}}$  is defined as

$$\mathcal{E}_i^{\text{a}} = \Delta_i, \quad (4.5)$$

where  $\Delta_i$  is the characteristic energy difference of the transition.

The number of electronic configurations and ionization channels increases rapidly with the atomic number  $Z$ , starting from only one channel for hydrogen via photoabsorption, and reaching already more than  $10^4$  channels for argon and many more than  $10^8$  for xenon [63]. While carbon is still a relatively light atom, the number of electronic configurations is already 27 (without taking into account electronic excitations into higher shells) and the possible ionization channels are close to 100. It is clear that tackling straightforwardly the full problem with such many transitions might not be the most transparent way to gain insight into the dynamics, and in order to do so we are going to start our analysis by studying fullerenes with a reduced and simplified number of channels.

#### 4.1.1 Rate equation description of two channels

As it has been mentioned before, the absorption of an X-ray photon by the core shell induces the subsequent Auger decay, leaving the ion doubly charged. While it is true that this process can occur repeatedly reaching even higher charge states, at this point we will restrict our study to this basic two step ionization scheme and generalize it for all the constituent atoms in  $\text{C}_{60}$ . Therefore we allow per atom only one photoelectron ( $e^{\text{ph}}$ ) from the core-shell and only one Auger electron ( $e^{\text{a}}$ ) from a well defined transition with a well defined rate. For the time being the possibilities of trapping and plasma formation, as well as nuclear movement, are not taken into consideration. In this simplified scenario, true for short and relatively weak pulses, the photoionization is continuously described by<sup>2</sup>

$$\dot{N}^0(t) = -\Gamma(t)N^0(t) \quad (4.6)$$

---

<sup>2</sup>In the following, we will use capital  $N$  to refer to the number of ions, while reserving lower case  $n$  for the number of electrons.

where  $N^0$  is the number of neutral atoms in the fullerene and  $\Gamma$  is the photoabsorption rate (3.23) at time  $t$ . The Auger decay process also follows a similar equation

$$\dot{N}_{(A)}^{+1}(t) = -\lambda N^{+1}(t) \quad (4.7)$$

with  $N^{+1}$  being the number of singly charged carbon ions and  $\lambda$  the constant Auger decay rate<sup>3</sup>. These two processes together determine a set of coupled differential equations that govern the time evolution of the individual ionic populations:

$$\begin{aligned} \dot{N}^0(t) &= -\Gamma(t)N^0(t), \\ \dot{N}^{+1}(t) &= \Gamma(t)N^0(t) - \lambda N^{+1}(t), \\ \dot{N}^{+2}(t) &= \lambda N^{+1}(t). \end{aligned} \quad (4.8)$$

These equations along with the initial conditions for a neutral fullerene  $C_{60}$ ,  $N^0(t_0) = N_0 = 60$  and  $N^{+1}(t_0) = N^{+2}(t_0) = 0$ , at  $t_0 \rightarrow -\infty$ , define the system evolution. From the ion number it is clear that the time evolution of the number of photoelectrons ( $n^{\text{ph}}$ ) and Auger electrons ( $n^{\text{a}}$ ) is determined by

$$\dot{n}^{\text{ph}}(t) = -\dot{N}^0(t) \quad (4.9a)$$

$$\dot{n}^{\text{a}}(t) = \dot{N}^{+2}(t) \quad (4.9b)$$

with the corresponding initial conditions  $n^{\text{ph}}(t_0) = n^{\text{a}}(t_0) = 0$ .

Before proceeding with the solution of the system of differential equations, it is pertinent to make some remarks. First of all, from (4.2) we observe that any scaling in the time domain will have no effect over the spectrum, as it is defined by the ratio of time derivatives. This means that, while the system itself is defined by the two rates  $\Gamma$  and  $\lambda$ , it suffices for the determination of the spectrum only to know the ratio of rates  $\Gamma/\lambda$ . Furthermore, from (4.3) we know that each channel contribution has its respective excess energy  $\mathcal{E}_i$  as its upper limit (which correspond to its respective atomic carbon line), while its lower limit is defined by the maximum attainable charge  $Q$  and their respective excess energy as follows

$$E_{\text{min},i}(t) = \mathcal{E}_i - \frac{Q(t)}{R}, \quad (4.10)$$

where it has been assumed for now that no trapping occurs for any of the channels.

We make a couple more final simplifications by considering first a rectangular pulse with a constant photoionization rate  $\Gamma$ , which allows for an explicit solution of the rate equations (4.8), and by assuming an excess energy for the Auger electrons  $\mathcal{E}^{\text{a}}$  big enough to avoid trapping. With all these assumptions the resulting spectra for the case  $\Gamma = \lambda = 1$  is shown in Fig. 4.2, where the final charge  $Q = 120$  means complete depletion of both channels. Here the excess energies  $\mathcal{E}^{\text{ph}} = 1200$  eV and  $\mathcal{E}^{\text{a}} = 600$  eV have been

---

<sup>3</sup>The subscript A is used in order to emphasize that this change in the number of  $N^{+1}$  ions is only due to the Auger process.

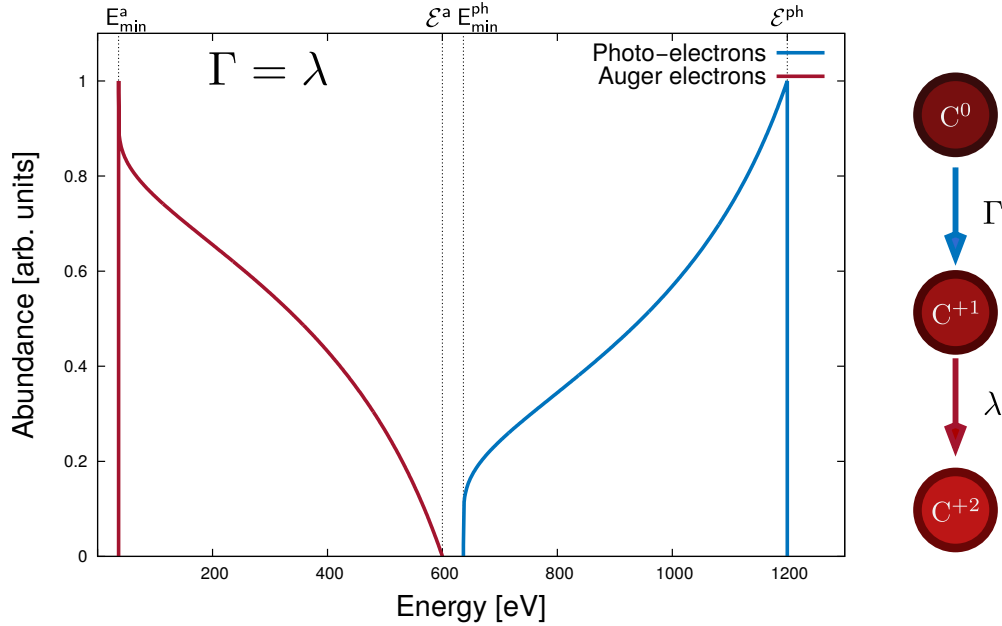


**Figure 4.2:** Spectrum obtained from rate equations for the case  $\Gamma = \lambda$ , showing the photoelectron (blue) and Auger (red) contributions, using a constant photoionization rate. The two step ionization path followed by the system is sketched on the right.

chosen in this way to prevent the overlapping of the contributions and to provide a clear graphical description.

In Fig. 4.2 is also observed that the photoelectrons show a skewed distribution that is “blue-shifted” towards higher energies, while the opposite “red-shift” is encountered in the Auger distribution. Also, a more intriguing feature is that both distribution seem to complement each other somehow. By analyzing some special cases for the parameter  $\Gamma/\lambda$  these features, as well as some others that will be encountered in following sections, will become clear.

### Fast Photoionization Limit ( $\Gamma \gg \lambda$ )

If the pulse intensity is so high that the photoabsorption rate  $\Gamma$  vastly overcomes the autoionization rate  $\lambda$ , that is  $\Gamma/\lambda \rightarrow \infty$ , all photoelectrons  $e^{\text{ph}}$  produced by the laser pulse would have escaped the system even before the first  $e^{\text{a}}$  is emitted. This effectively decouples entirely the equations (4.8) and divides them into two separate simpler subsystems. For the photoelectrons we have

$$\begin{aligned} \dot{N}^0(t) &= -\Gamma(t)N^0(t), \\ \dot{N}^{+1}(t) &= \Gamma(t)N^0(t), \end{aligned} \quad (4.11)$$



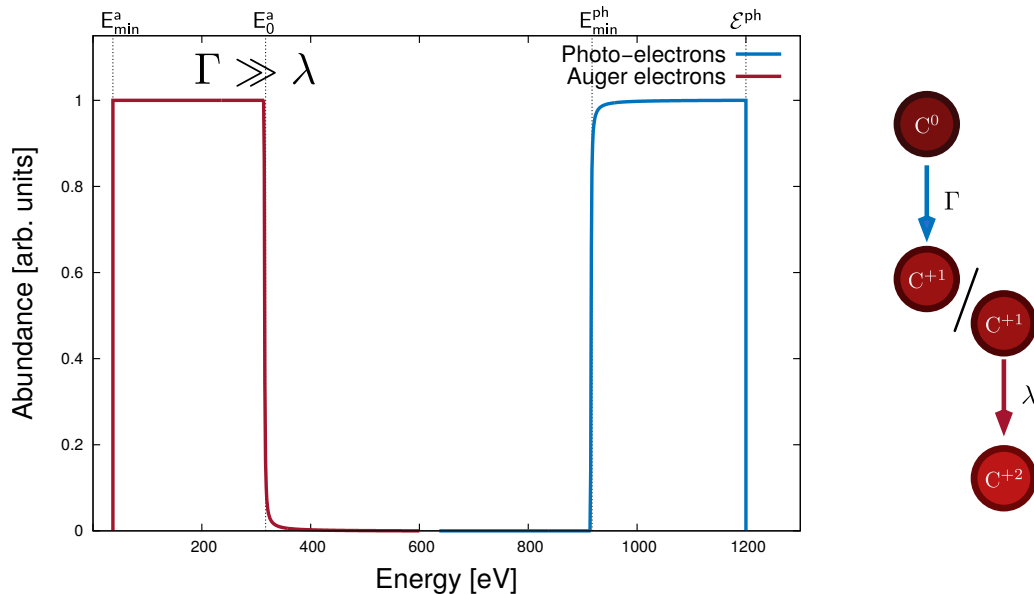


**Figure 4.3:** Electron energy spectrum numerically obtained in the fast photoionization limit for a ratio  $\Gamma/\lambda = 10^3$  with a rectangular pulse of infinite length. The electronic contributions are shown following the same color coding. The decoupled ionization path undergone by the system is shown on the right

with initial conditions  $N_0 = 60$  and  $N^{+1}(0) = 0$ . In the same way, on a completely different time scale, we have for the Auger electrons

$$\begin{aligned}\dot{N}^{+1}(t) &= -\lambda N^{+1}(t), \\ \dot{N}^{+2}(t) &= \lambda N^{+1}(t),\end{aligned}\tag{4.12}$$

with corresponding initial conditions  $N^{+1}(t'_0) = 60$  and  $N^{+2}(t'_0) = 0$ . The initial conditions determine the energy interval of each contribution.

The electron energy spectrum can be readily calculated without solving the differential equations (4.11) or (4.12), as from equation (4.3) we have for each of the decoupled subsystems dealing with  $e^{\text{ph}}$  and  $e^{\text{a}}$ , in their respective time scales

$$\left| \dot{E}_i(t) \right| = \frac{1}{R} \left| \dot{n}_i(t) \right|.\tag{4.13}$$

This means quite naturally that during the time scale relevant for the emission of photoelectrons, the system is only charged by this channel, and the same is true for the Auger electron timescale at a later time. Given that fact, the electron spectrum calculated from (4.2) simply reads

$$P(E) = |R|_{t=t'_{\text{ph}}(E)} + |R|_{t=t'_a(E)},\tag{4.14}$$

that is, the spectrum takes constant values over the energy intervals defined by each of the separate subsystems forming two separate plateaus of equal height.

The energy interval is defined by the boundary conditions of each subsystem, therefore in this case the final charge for the photoelectrons serves at the same time as the initial charge for the Auger electrons, that is  $Q^{\text{ph}} = q^{\text{a}}(t_0) = 60$ . The resulting spectrum, calculated numerically by solving (4.8) for the case  $\Gamma/\lambda = 10^4$ , is shown in Fig. 4.3 along with the corresponding  $\mathcal{E}_i^{\text{min}}$  and  $\mathcal{E}_i^{\text{max}}$  for each channel, calculated according to the corresponding boundary conditions. From the way these energy intervals are defined, if  $\mathcal{E}^{\text{ph}} > \mathcal{E}^{\text{a}}$ , there is no possible way that these two plateaus can overlap in the fast photoionization limit.

These results, obtained for a very simplified case, can also be applied to more complex scenarios with many more ionization channels. For example, in XFEL experiments with high intensities it is now possible to produce double core-holes by the absorption of two photons [30, 57]. As long as we can separate the photoabsorption processes and the following autoionization processes into subsystems with different time scales, while the electron spectra for each contribution can possibly be more complicated than just the plateau observed here, we would be able to treat each process separately and even control the overlap by using appropriate photon energies.

### Fast Autoionization Limit ( $\lambda \gg \Gamma$ )

For long pulses of low intensity we find ourselves in the fast autoionization limit where  $\lambda$  easily overcomes  $\Gamma$ , that is  $\Gamma/\lambda \rightarrow 0$ . In this regime the Auger decay occurs almost instantly with respect to the photoionization time scale, so we can effectively think of the simultaneous emission of  $e^{\text{ph}}$  and  $e^{\text{a}}$  after each photoabsorption. This bypasses the intermediate state  $N^{+1}$  and collapses the equations (4.8) into a simpler form that reads

$$\begin{aligned}\dot{N}^0(t) &= -\Gamma(t)N^0(t), \\ \dot{N}^{+2}(t) &= \Gamma(t)N^0(t),\end{aligned}\tag{4.15}$$

which consequently affects the ionization rates as

$$\dot{n}^{\text{ph}}(t) = \dot{n}^{\text{a}}(t) = \Gamma(t)N^0(t),\tag{4.16}$$

reflecting how these two electrons are emitted with a time difference that is negligible compared to the time between two photoabsorption events.

For the fast autoionization limit it is once again not necessary to explicitly solve the system (4.15) in order to calculate the electron energy spectrum, as we have for the energy change in this case

$$\left| \dot{E}_i(t) \right| = \frac{2}{R} \left| \dot{n}_i(t) \right|.\tag{4.17}$$

This means that, as the emission of any photoelectron is accompanied by an Auger (and the other way around), every new  $e^{\text{ph}}$  or  $e^{\text{a}}$  experiences a background charge increase by  $\delta q = 2$ . Calculating the electron spectrum from (4.2), it takes the following simple form

$$P(E) = \left| \frac{R}{2} \right|_{t=t'_{\text{ph}}(E)} + \left| \frac{R}{2} \right|_{t=t'_a(E)},\tag{4.18}$$

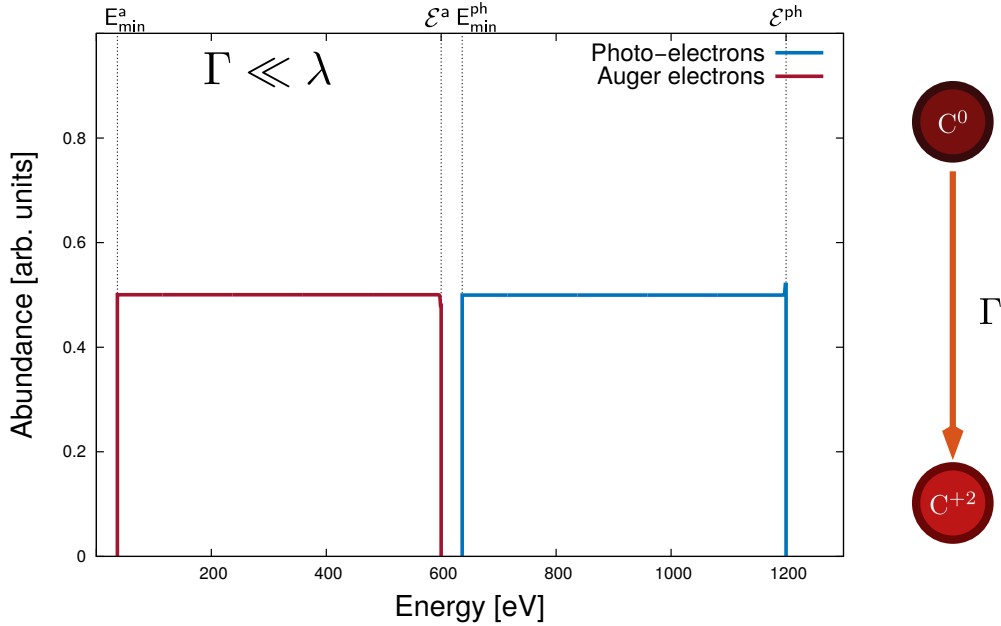


**Figure 4.4:** Electron energy spectrum for the fast autoionization regime numerically obtained with a rate  $\Gamma/\lambda = 10^{-3}$  from a rectangular pulse of infinite length with the same color coding. The ionization path, highlighting the effective instantaneous two electron removal is sketched on the right side.

which once again correspond to two plateaus of the same height. A couple differences are evident with respect to the fast photoionization limit, as the height is half the one observed for that case, while its energy interval over which they are defined is in turn stretched by a factor of 2. More importantly, due to the perfect correlation between the emission times of the photoelectrons and Auger electrons, the only difference in the energy intervals given by the functions  $t'_{\text{ph}}(E)$  and  $t'_a(E)$  comes from their respective excess energies  $\mathcal{E}^{\text{ph}}$  and  $\mathcal{E}^a$ . This means that the Auger electron plateau is a perfect copy of the photoelectron one, only displaced due to the different excess energies. This would also be true even if the photoelectron distribution happens to have a different, arbitrary shape.

The electron spectrum obtained numerically for the case  $\Gamma/\lambda = 10^{-4}$  is shown in Fig. 4.4. There we observe both the reduced height and increased width of the plateaus, by the predicted factors. Contrary to the fast photoionization case, overlapping of the distributions can be achieved if the charging is high enough, such that  $E_{\text{ph}}^{\text{min}} \leq \mathcal{E}^a$  (assuming a photon energy such that  $\mathcal{E}^a < \mathcal{E}^{\text{ph}}$  is used).

Once again, with these simplified example we have obtained results that can be applied to more complicated scenarios in the upcoming sections. Here we have seen that in the limit of fast autoionization, the perfect correlation between the emission times of Auger and photoelectrons gets reflected into distributions that are identical, and are only displaced due to different excess energies.

### Comparable Rates: $\Gamma = 2\lambda$

It is clear that in most regimes the channels will not be entirely decoupled as in the fast photoionization limit, nor perfectly correlated as in the fast autoionization case, and the spectrum will not show the simple plateaus from these scenarios, as we already observed in Fig. 4.2. We need then to study a regime where both rates are of comparable magnitude and we have chosen the particular case for  $\Gamma/\lambda = 2$ , as it allows not only to showcase the trends obtained in this regime but also allows a simple analytic form for the spectrum.

In this case the equations (4.8), for a rectangular pulse, reads

$$\begin{aligned}\dot{N}^0(t) &= -2\Gamma N^0(t), \\ \dot{N}^{+1}(t) &= 2\Gamma N^0(t) - \Gamma N^{+1}(t), \\ \dot{N}^{+2}(t) &= \Gamma N^{+1}(t).\end{aligned}\tag{4.19}$$

Here, unlike in the previous scenarios, it is necessary to explicitly include the pulse shape. Also, for the electrons we have from (4.9) that the ionization rates are expressed as

$$\dot{n}^{\text{ph}}(t) = 2\Gamma N^0(t),\tag{4.20a}$$

$$\dot{n}^{\text{a}}(t) = \Gamma N^{+1}(t).\tag{4.20b}$$

The system (4.19) is solved to obtain the time-dependent number of ions as

$$\begin{aligned}N^0(t) &= N_0 e^{-2\Gamma t}, \\ N^{+1}(t) &= 2N_0 \left( e^{-\Gamma t} - e^{-2\Gamma t} \right), \\ N^{+2}(t) &= N_0 \left( 1 - e^{-\Gamma t} \right),\end{aligned}\tag{4.21}$$

which along equations (4.3) and (4.20) allows us to obtain the time-dependent energy change as

$$\left| \dot{E}_i(t) \right| = \frac{2N_0\Gamma}{R} e^{-\Gamma t}.\tag{4.22}$$

With this result in hand we can calculate the electron spectrum following equation (4.2), obtaining for each of the contributions the expressions

$$P_{\text{ph}}(E) = R \left| e^{-\Gamma t} \right|_{t=t'_{\text{ph}}(E)},\tag{4.23a}$$

$$P_{\text{a}}(E) = R \left| \left( 1 - e^{-\Gamma t} \right) \right|_{t=t'_a(E)},\tag{4.23b}$$

where the time  $t$  parametrizes the energy. We can remove this temporal dependence by using equation (4.3), as for each channel we have then

$$e^{-\Gamma t} = 1 + \frac{R}{2N_0} (E_i - \mathcal{E}_i).\tag{4.24}$$

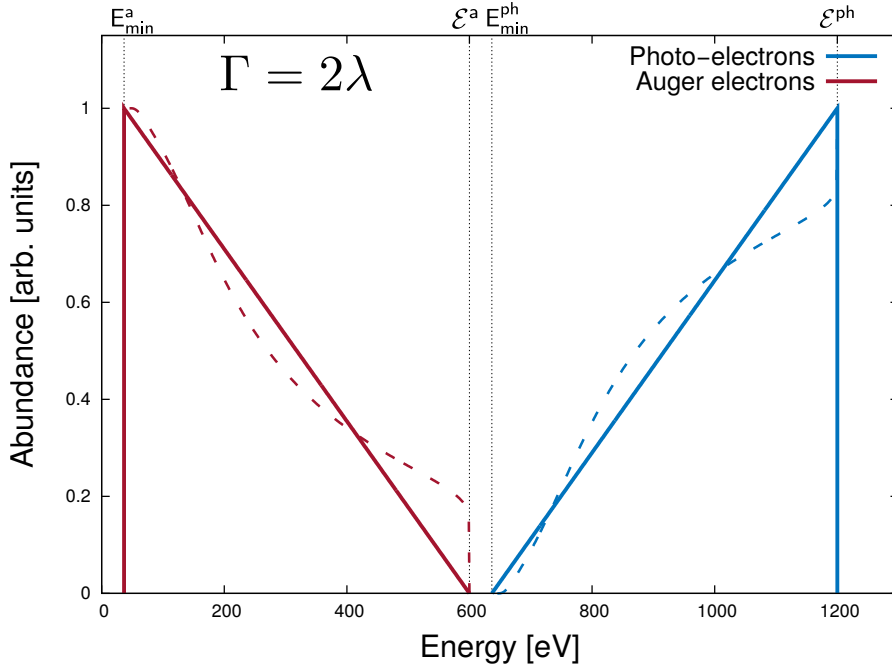


**Figure 4.5:** Energy spectra of Auger and photoelectrons for the ratio  $\Gamma/\lambda = 2$  numerically calculated for a rectangular pulse of infinite length (solid lines), as well as using a Gaussian pulse with  $T = 3/\Gamma$  (dashed lines).

By substituting this result into (4.23) we obtain the final form of the spectrum as follows

$$P_{\text{ph}}(E) = R + \frac{R^2}{2N_0} (E - \mathcal{E}^{\text{ph}}) \quad \text{for } E_{\text{min}}^{\text{ph}} \leq E \leq \mathcal{E}^{\text{ph}}, \quad (4.25a)$$

$$P_{\text{a}}(E) = \frac{R^2}{2N_0} (\mathcal{E}^{\text{a}} - E) \quad \text{for } E_{\text{min}}^{\text{a}} \leq E \leq \mathcal{E}^{\text{a}}, \quad (4.25b)$$

showing quite surprisingly a simple linear dependence with respect to the energy.

The spectrum obtained numerically for this case is shown in Fig. 4.5 where we confirm the predicted linear behavior which has a quite intuitive interpretation. When the pulse begins (that is, in the high energy part of each contribution) the probability to ionize a neutral carbon atom is certain, while the emission of an Auger electron is not possible. As more photoelectrons are emitted, the probability that the next emitted electron comes from photoabsorption is reduced, while the increase in the number of core-holes make the emission of Auger electrons to be more likely until, at the end of the pulse (the low energy part of the contribution), the emission of the last electron is certain to come from an Auger decay. For this special case of  $\Gamma/\lambda = 2$  the emission probability changes linearly with each photon absorbed, which is at first sight somehow hidden due to the more complicated temporal dependence.

As we previously remarked, in this regime the temporal pulse dependence is critical

to the final shape of the spectrum. To illustrate this we include with broken lines in Fig. 4.5 the spectrum calculated for the same ratio with a time-dependent Gaussian pulse of the form

$$\Gamma(t) = \Gamma_0 \exp\left(-4 \ln 2 \left(\frac{t}{T}\right)^2\right), \quad (4.26)$$

with peak intensity  $\Gamma_0$  and pulse length  $T = 3/\Gamma_0$ . We observe that although the simple linear functionality is lost, the qualitative features remain and the spectrum shape can be now understood as a deviation due to the time-dependent ratio  $\Gamma/\lambda$ .

This simple example also helps us to understand the role that the pulse length plays as we observe in the higher energy parts of the contributions a distortion in the direction of fast autoionization. This happens due to photoionization events occurring in the tails of the pulse where the ratio is considerably smaller. In order to suppress this effect a pulse whose length is shorter than the autoionization timescale is needed, which will prove to be a recurring condition to understand more complicated spectra in further sections. This emphasizes the importance of XFEL sources to study multichannel ionization due to the uniquely extreme requirements of short pulses and high intensities.

### Special Remarks for Equal Energies $\mathcal{E}^{\text{ph}} = \mathcal{E}^{\text{a}}$

We conclude our rate equation study by making some remarks for the particular case where both the Auger and photoelectrons share the same excess energy, which can be achieved by tuning the incoming photon energy. In this scenario, while in general  $\dot{n}_{\text{ph}} \neq \dot{n}_{\text{a}}$ , we encounter that for both channels  $\dot{E}_{\text{ph}}(t) = \dot{E}_{\text{a}}(t)$ , therefore the inverse functions  $t'_i(E)$  are also equal. In that case equation (4.2) can be written as

$$\begin{aligned} P(E) &= \int dt \delta(E - E'(t)) \sum_i \dot{n}_i(t), \\ &= \left| \frac{\sum_i \dot{n}_i(t)}{\dot{E}'(t)} \right|_{t=t'(E)}. \end{aligned} \quad (4.27)$$

It is clear from equation (4.3) that

$$\dot{E}'(t) = -\frac{1}{R} \sum_i \dot{n}_i(t)$$

and we can write expression (4.27) simply as

$$P(E) = R, \quad \text{for } \mathcal{E} - Q \leq E \leq \mathcal{E}. \quad (4.28)$$

This means that whenever the electrons emitted from different ionization processes share the same energy, they will effectively appear as a single channel in the electron energy spectrum, showing up just as a plateau. This happens regardless of the number of channel and also independently from the nature of the processes.

This can clearly be seen in all the previous studies, and explains why the distributions from photo and Auger electrons seem to complement each other. This also clearly happens independently of the pulse shape, as seen in the case of Gaussian pulses in Fig. 4.5. This feature might be useful when complicated systems with many channels are encountered, as it provides a way to simplify the spectrum and its interpretation.

## 4.2 Molecular Dynamics of Multi-channel Ionization in Fullerenes

Even if the rate equation treatment of the previous section has already shed some light on our problem, in order to deepen our understanding of multiple channel ionization we need to take a step towards a more realistic treatment by means of molecular dynamics. By doing so we move away from all the simplifications previously made, as we allow the system to reach higher ionic states through all the available ionization channels present in atomic carbon. We also include all the pairwise interactions among the particles including the ions with time-dependent charges, naturally including correlations and collision as the system is propagated in time.

### 4.2.1 MD Simulation Details

The initial configuration of the system is simply obtained by using the molecular coordinates of the fullerene  $C_{60}$  (which correspond to a truncated icosahedron of radius  $R = 3.5 \text{ \AA}$  [58]), and placing a neutral carbon atom at each vertex accounting for a total of 60 atoms. The system is then exposed to a Gaussian XFEL pulse according to equation (3.22). Assuming only single-photon photoabsorption is present, the probability of a photoionization event happening in a time interval  $\Delta t$  is given, for each atom  $i$ , as

$$p_{\text{abs},i}(t) = \frac{I(t)}{\hbar\omega} \sigma_{\omega,i}(t) \Delta t, \quad (4.29)$$

where  $\sigma_{\omega,i}$  is the photoabsorption cross-section of the ion  $i$  at time  $t$ . This time dependence is not trivial as the electronic configuration of each carbon ion, with electrons distributed in its three subshells<sup>4</sup>, continuously suffer changes due to electron emission and refilling of core-holes. For a carbon ion with electronic configuration  $(m_1, m_2, m_3)$ , the photoabsorption cross-section would be given by

$$\sigma_{\omega} = \sum_j m_j \sigma_{\omega,j} \quad (4.30)$$

with  $\sigma_{\omega,j}$  being the photoionization cross-section of the sub-shell  $j$  at frequency  $\omega$ . However, for photon energies larger than 1 keV, we can restrict ourselves to photoabsorption by the  $1s$  orbital as its cross-section accounts for 95% of the total absorption [64].

---

<sup>4</sup>In the following, to specify any arbitrary electronic configuration ( $1s^k 2s^l 2p^m$ ) it will suffice to state three numbers  $(k, l, m)$ . According to this convention, the initial electronic configuration of a neutral carbon atom is written as (2,2,2).

Transition	Atomic		Molecular	
	Rate $\lambda_A$ $10^{-4}$ [a.u.]	Lifetime $\tau$ [fs]	Rate $\lambda_A$ $10^{-4}$ [a.u.]	Lifetime $\tau$ [fs]
ss	8.42	28.7	17.32	14.0
sp	7.66	31.5	15.75	15.4
pp	3.54	68.7	7.28	33.3
Total	19.62	12.3	40.35	6.0

**Table 4.1:** Auger decay rates and lifetimes for single core ionized carbon, both atomic and in a molecular environment, as implemented in the simulation.

The Auger decay process is also modeled through the same probabilistic scheme, where the probability for this transition to occur in a given ion  $i$  during a time interval  $\Delta t$  is given by

$$p_{\text{Aug},i}(t) = \lambda_i(t)\Delta t, \quad (4.31)$$

where  $\lambda_i$  is the decay rate due to all possible Auger transitions ( $ss, sp$  and  $pp$ ) that the ion  $i$  might undergo according to its electronic configuration, that is

$$\lambda_i = \alpha_{ss,i}\lambda_{ss} + \alpha_{sp,i}\lambda_{sp} + \alpha_{pp,i}\lambda_{pp} \quad (4.32)$$

where the coefficients  $\alpha$  weight the probability of each transition due to the electronic vacancies. As an illustrative example, if we consider an ion  $i$  with electronic configuration  $(1, 1, 2)$ , its decay rate would be  $\lambda_i = \lambda_{sp}/2 + \lambda_{pp}$ , as no  $ss$  transition is possible, and only half of the  $sp$  channels remain available. The electronic configuration of the ion after the decay is randomly determined according to the relative weights  $\alpha$ .

In order to reflect the complexity of the molecular environment, the individual transitions are approximated using a typical molecular Auger lifetime of 6 fs [65–67] and the branching ratios of carbon in its atomic state [68]. The radiative decay of carbon core-holes, both atomic and in a molecular environment, is about 2 orders of magnitude slower than the nonradiative Auger decay, and is not considered here. In the Table 4.1 are summarized the values of the transition rates used in the simulations along with the rates for the atomic case for comparison.

As it has been stated before there is some strong evidence, both theoretical [69, 70] and experimental [31, 71], that for the exotic double core-hole states achievable under XFEL pulses the Auger decay rate for several low  $Z$  elements (including of course carbon) systematically exceeds the expected factor of two, with respect to the single core-hole rate. As no experimental values for double core-holes decay rates in fullerene are presently available, and because the electronic properties of fullerene prove time and time again to be quite exceptional [59], we refrain from making any claim on that matter and will simply regard the decay rate of these exotic states as twice the rate of the single core-hole state.



Whenever an electron emission from an ionization channel  $i$  takes place, the magnitude of the initial momentum is given by the characteristic excess energy of said channel as

$$p_{0,i} = \sqrt{2\mathcal{E}_i}, \quad (4.33)$$

while its direction is chosen randomly according to an isotropic distribution. Depending on the nature of the ionization channel,  $\mathcal{E}_i$  is calculated following either (4.4) for a photoelectron, or (4.5) for an Auger electron.

For the determination of the parameters  $E_{b,i}$  and  $\Delta_i$  we have obtained the energies for each of the different ionic states and electronic configurations by means of a DFT calculation. In this way the binding energies  $E_{b,i}$ , required to determine the photoionization excess energy  $\mathcal{E}_i^{\text{ph}}$ , take values ranging from 285 eV for the case of neutral carbon up to 476 eV for the case of a  $\text{C}^{+5}$  ion (the electronic configurations of the parent ions are (2,2,2) and (1,0,0) respectively). Similarly for the many different Auger decay transitions we obtain excess energies  $\mathcal{E}_i^{\text{a}}$  ranging from 229 eV up to 287 eV.

The system is propagated in time according to the full Hamiltonian including all the pairwise Coulombic interactions

$$H = \sum_{i=1}^N \frac{\mathbf{p}_i^2}{2m_i} + \sum_{i<j}^N \frac{q_i q_j}{|\mathbf{r}_i - \mathbf{r}_j|}, \quad (4.34)$$

where  $N$  is the the number of interacting particles, including both electrons and ions. It should be noted that in the present scheme, unlike the Coulomb complex MD simulations, the number of particles (as well as the ionic charges) change in time due to the electron emission. Several realizations are needed in order to obtain meaningful data and good statistics for the spectrum, as well as long simulation times. This is made not only to achieve the required asymptotic energies but also to ensure the complete decay of all excited states, which can happen long after the pulse is gone.

Having provided and explained all the details of our molecular dynamics simulation scheme, we will apply it to study multi-channel ionization of fullerenes in two steps. First we will perform all the calculations making just one simplifying assumption, which is that the ions remain fixed at their initial positions. This will prove useful when trying to connect with the previously obtained rate equations results. Once the similarities have been acknowledged, we will proceed with the full simulation including ionic motion for a complete treatment.

## 4.2.2 Multiple Ionization of Fullerenes with Fixed Ions

In order to facilitate the interpretation of the simulation results, we will take a moment to form a general qualitative idea of the present dynamics and the involved processes. We begin by recognizing that, assuming no other ionization mechanisms are involved, the number of ions of all possible electronic configurations in the system at any given

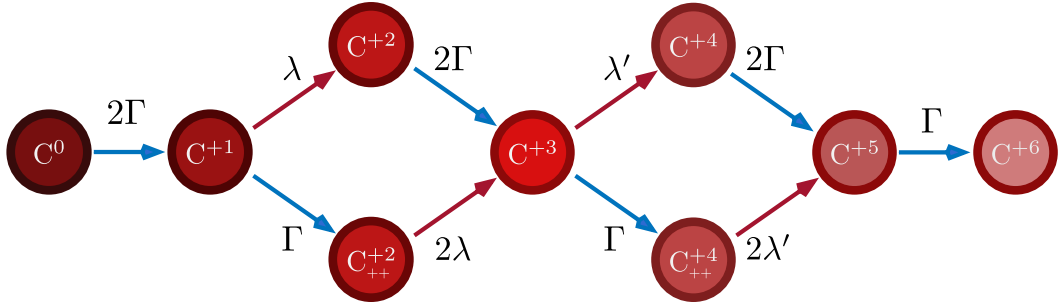


**Figure 4.6:** Simplified scheme of the ionization path of carbon atoms in fullerenes, from a neutral state until total depletion. Photoionization processes are depicted with blue arrows, while autoionization is similarly depicted with red ones.

time is described, in the most general way, by a set of coupled rate equations of the form

$$\begin{aligned} \dot{N}_K(t) = & \sum_{K' \neq K} (\Gamma_{K' \rightarrow K}(t) + \lambda_{K' \rightarrow K}) N_{K'}(t) \\ & - \sum_{K' \neq K} (\Gamma_{K \rightarrow K'}(t) + \lambda_{K \rightarrow K'}) N_K(t). \end{aligned} \quad (4.35)$$

Here the index  $K$  denotes a specific electronic configuration (given by the triad  $(k, l, m)$ ), and spans over all the possible configurations.

Only certain configuration pairs  $(K, K')$  have non-zero photoabsorption ( $\Gamma$ ) or Auger decay ( $\lambda$ ) rates, restricted to transitions where  $|\Delta q_{K \rightarrow K'}| = 1$ . The number of electrons in the core-shell determines the feasibility of each process, as can be seen in the diagram shown in Fig. 4.6. It sketches in a simplified manner the different transitions along the ionization path of a given carbon atom until full electron removal is reached, according to the aforementioned assumptions.

It is clear that the first ionization event is necessarily caused by the absorption of a photon and, according to our assumptions, takes place with a core electron. The formed  $C^{+1}$  ion can further be ionized by two processes, either by absorbing another photon and creating a double core-hole (absorption occurs with half the rate of the  $C^0$  atom, as the core-shell only has one remaining electron), or by an Auger decay which refills the core vacancy. A double core-hole ion  $C^{+2}_{++}$  is a highly excited state transparent to the laser field and can only undergo an Auger transition (twice as fast compared to a single core-hole state), and correspondingly an  $C^{+2}$  ion with refilled core-shell can only be ionized by absorbing another photon. Both transitions produce a  $C^{+3}$  with a single core electron, for which two ionization possibilities are available once again. Proceeding in this way the  $C^{+5}$  ion is reached, containing only one core-electron, for which only photoionization is available (as autoionization requires the participation of two electrons) to completely strip the ion. Following these observations, we arrive to a simplified version

of the equations (4.35) as

$$\begin{aligned}
\dot{N}^0 &= -2\Gamma N^0, \\
\dot{N}^{+1} &= 2\Gamma N^0 - (\Gamma + \lambda) N^{+1}, \\
\dot{N}_{++}^{+2} &= \Gamma N^{+1} - 2\lambda N_{++}^{+2}, \\
\dot{N}^{+2} &= \lambda N^{+1} - 2\Gamma N^{+2}, \\
\dot{N}^{+3} &= 2\lambda N_{++}^{+2} + 2\Gamma N^{+2} - (\Gamma + \lambda') N^{+3}, \\
\dot{N}_{++}^{+4} &= \Gamma N^{+3} - 2\lambda' N_{++}^{+4}, \\
\dot{N}^{+4} &= \lambda' N^{+3} - 2\Gamma N^{+4}, \\
\dot{N}^{+5} &= 2\lambda' N_{++}^{+4} + 2\Gamma N^{+4} - \Gamma N^{+5}, \\
\dot{N}^{+6} &= \Gamma N^{+5}.
\end{aligned} \tag{4.36}$$

It follows that to completely ionize a fullerene  $C_{60}$  molecule, a total of 240  $e^{\text{ph}}$  and 120  $e^{\text{a}}$  have to be emitted.

Another advantage of this schematic representation is that now, due to the assumptions made, it is possible to assign uniquely an excess energy for each transition and each process. Therefore we can write the energy and excess energy of a photoelectron leaving a  $C^{+1}$  ion as  $E_i^{\text{ph}}(t)$  and  $\mathcal{E}_i^{\text{ph}}$  correspondingly, and equivalently  $E_i^{\text{a}}(t)$  and  $\mathcal{E}_i^{\text{a}}$  for an Auger electron. It should be emphasized however that in this way we refer only to an average value of the excess energy from all the possible configurations, fully taken into account by the simulations.

With this picture in mind we proceed to analyze the results from the simulations with fixed ions for different cases, using different values for the ratio  $\Gamma/\lambda$ , which correspond to different intensities. At this point a photon energy  $E_\omega = 2 \text{ keV}$  is chosen in order to avoid overlapping between the spectral regions of  $e^{\text{ph}}$  and  $e^{\text{a}}$ , helping in this way to identify the different contributions and improve clarity in the discussion.

### Fast Photoionization Limit ( $\Gamma \gg \lambda$ )

We begin in a similar way as in our rate equation study by analyzing the fast photoionization limit. To this end we use a ratio  $\Gamma/\lambda = 100$  for which, using an Auger lifetime of 6 fs and the corresponding photoabsorption cross-section at the photon energy  $E_\omega = 2 \text{ keV}$ , a pulse with peak intensity of  $I = 1.9 \times 10^{21} \text{ W/cm}^2$  is required. By using a pulse length of  $T = 10 \text{ fs}$  we obtained a number of absorbed photons  $n_{\text{ph}} = 217$ , achieving a high system charge and fully stripping more than half of the atoms.

The resultant spectrum is shown in Fig. 4.7 along with a diagram emphasizing the preferred ionization path undergone by the system. With high intensities the formation of double core-holes is greatly favored and, according to the rate equations results, we might expect a very high plateau for the photoelectrons and a strong displacement into lower energies for Auger electrons. We see that this is indeed the case for the Auger electrons, as a very small amount of  $e^{\text{a}}$  are observed for positive energies as well as a high peak near zero due to plasma evaporation. This indicates that photoionization builds

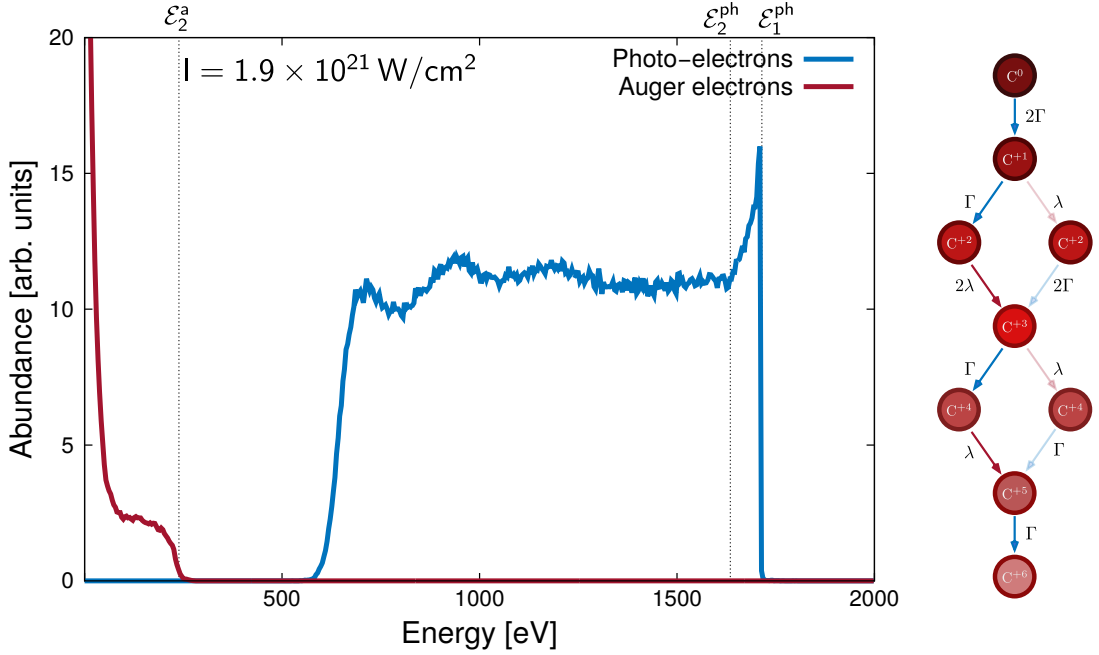


**Figure 4.7:** Electron energy spectrum calculated by molecular dynamics with fixed ions for a ratio  $\Gamma/\lambda = 100$ ,  $E_\omega = 2000$  eV and pulse length  $T = 20$  fs. An schematic of the preferred ionization path is presented, highlighting the favored formation of double core-hole states.

a high system charge  $Q$  before the Auger electrons are produced and therefore most of them are trapped due to the deep potential.

The photoelectron spectrum shows instead a triangular peak, which we could only expect for ionization channels whose rates are in an exact ratio of 2 (see section 4.1.1). While this certainly is not the case for photoelectrons and Auger electrons, it indeed happens for photoelectrons emitted from  $C^0$  and  $C^{+1}$  leaving respectively a single and a double core-hole ion (see equations (4.36)), which have the exact required ratio and are strongly favored in this intensity regime experiencing almost no influence from other channels. Given that, the width  $\delta E_{\text{peak}}$  of the triangular peak can be in fact easily related to the difference of excess energies

$$\delta E_{\text{peak}} = \mathcal{E}_1^{\text{ph}} - \mathcal{E}_2^{\text{ph}} = 80 \text{ eV},$$

as can be observed in the spectrum.

From the photoelectron spectrum we can also read that  $E_{\text{min}}^{\text{ph}} \approx 600$  eV, which according to the ionization path from Fig. 4.7 and the corresponding photoelectron excess energies should correspond to an electron leaving a fully striped  $C^{+6}$  ion behind with  $\mathcal{E}_6^{\text{ph}} = 1524$  eV. From equation (4.10) we can obtain a value for the final system charge  $Q$  as

$$Q = R \left( \mathcal{E}_6^{\text{ph}} - E_{\text{min},6}^{\text{ph}} \right)$$

which in this case yields  $Q \approx 230$ . Knowing that  $n_{\text{ph}} = 217$  we arrive to the conclusion

that only about 13 Auger electrons escaped during the pulse, while around 107 were trapped by the potential.

As a final remark for this case we would like to point out that the number of  $e^{\text{ph}}$  reached here will seem low in comparison to other regimes. This is a natural consequence of the creation of double core-holes, which renders the atom transparent to the incoming photons making it harder for the system to reach full ionization.

### Fast Autoionization Limit ( $\lambda \gg \Gamma$ )

We now turn our attention to the fast autoionization regime which is achieved with low intensities, employing for this a ratio  $\Gamma/\lambda = 0.01$ . Following the exact same assumptions as in the previous case this requires a pulse intensity of  $I = 1.9 \times 10^{17} \text{ W/cm}^2$  and, due to the low photoabsorption rate, a pulse length of  $T = 2000 \text{ fs}$  is used to significantly ionize the system. This yields a total number of photoelectrons  $n_{\text{ph}} = 226$ , implying that complete ionization is achieved for almost all ions.

In Fig. 4.8 the numerically obtained spectrum is shown, accompanied by the corresponding diagram highlighting the preferred ionization path followed by the system under these conditions. Due to the low intensity the Auger decay enabled by the absorption of a photon is almost certain to occur before the ion absorbs a second one, and double core-hole states should be virtually absent (eq. (4.36)). From our rate equation results of section 4.1.1 we might expect that both photoelectrons and Auger electrons should have identical distributions according to a plateau, and that is exactly what we obtain in our full simulation. In addition, as more Auger electrons are able to escape the system, the plasma peak near zero energy is less prominent than in the previous case.

There is, however, a new feature in the photoelectron spectrum, a characteristic step that separates the high-energy part from the low-energy region. In order to understand this step we have to acknowledge an important qualitative difference between these two regions. For the high energy part of the spectrum (that is, at the beginning of the pulse) the creation of a photoelectron is accompanied by an Auger electron and both leave the system, in this way the next pair of emitted electrons will see an increase of the background charge by  $\delta q = 2$ . As the charge is built up there is a point where the kinetic energy of the Auger electron is no longer enough to escape the Coulomb potential and the electron gets trapped. Just as in the case of clusters in chapter 3, this trapping is reflected in the screening of the photoelectrons, and each new one sees a charge increase of only  $\delta q = 1$ . It is clear this step does not show up in the fast photo-ionization regime, as nearly all Auger electrons emitted under those circumstances are immediately trapped and no qualitative change is observed.

Based on this behavior we can define an energy  $E_{\text{trap}}$  where the screening sets in as

$$E_{\text{trap}} = \mathcal{E}_1^{\text{ph}} - \mathcal{E}_2^{\text{a}} \quad (4.37)$$

which simply corresponds to the energy difference between the first photo-ionization and the first autoionization channels. For this to happen a charge  $Q_{\text{trap}}$  has to be reached

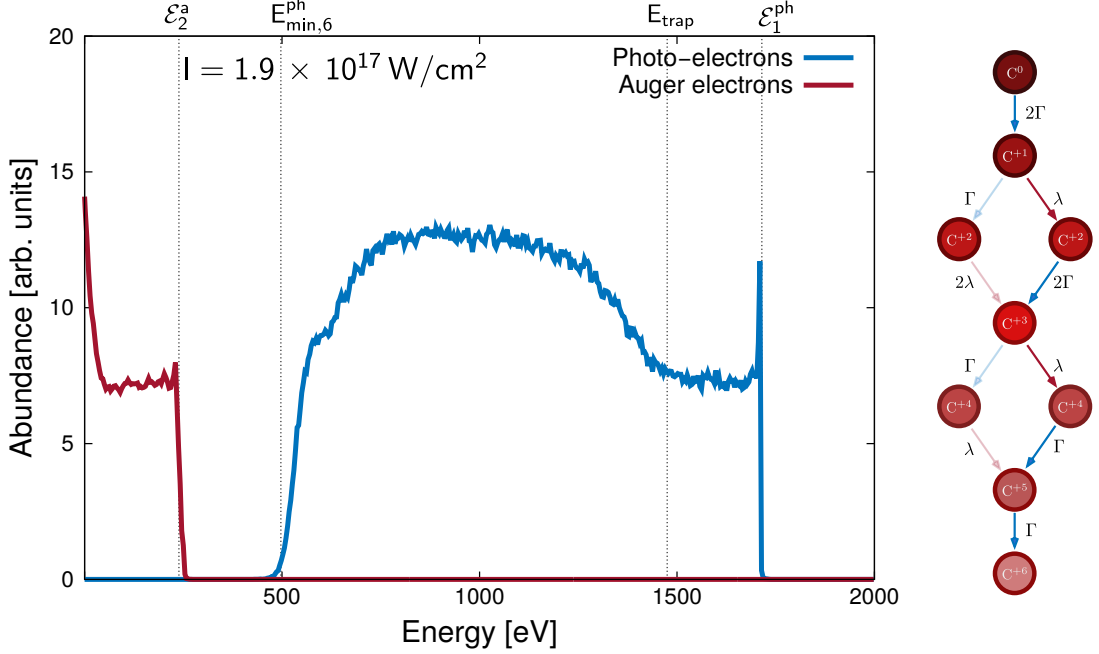


**Figure 4.8:** Electron energy spectrum calculated by molecular dynamics with fixed ions for a ratio  $\Gamma/\lambda = 0.01$ ,  $E_\omega = 2000$  eV and pulse length  $T = 2000$  fs. An schematic representation of the preferred ionization path is presented, where the simultaneous emission of photo- and Auger electrons is highlighted.

such that

$$\frac{Q_{\text{trap}}}{R} = \varepsilon_2^{\text{a}},$$

for which we have  $Q_{\text{trap}} \approx 59$ . Up to this point the system charge is formed in equal parts by Auger and photoelectrons and it follows immediately that  $Q_{\text{trap}}/2 \approx 29$  is the number of Auger electrons that can escape the system, while approximately 91 are trapped.

Using the 29 escaped Auger electrons, along with the 226 photoelectrons we can estimate the minimum energy of the photoelectron spectrum using equation (4.10) with the last photoionization channel. Through this we obtain  $E_{\text{min},6}^{\text{ph}} = 497$  eV which is in good agreement with the minimum photoelectron energy observed in Fig. 4.8.

### Equal Rates: $\Gamma = \lambda$

We close our molecular dynamics study of fullerene with fixed ions by analyzing the case where the photo-ionization and the Auger have the exact same rates. In this case we determine that an intensity  $I = 1.9 \times 10^{19}$  W/cm<sup>2</sup> is needed, and we utilize a pulse length  $T = 80$  fs to obtain a considerable degree of ionization. With this condition we find a yield of  $n_{\text{ph}} = 238$ , indicating total ionization was achieved in almost all the realizations.

In this regime there is no clear preferred ionization path and as we can observe, the

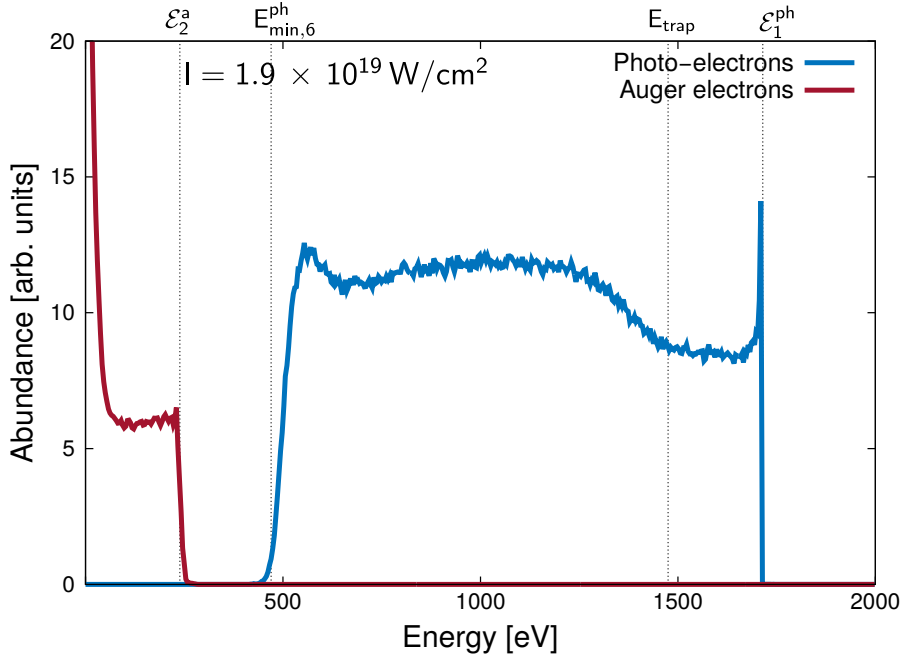


**Figure 4.9:** Electron energy spectrum obtained by molecular dynamics with fixed ions for equal rates  $\Gamma = \lambda$ ,  $E_\omega = 2000$  eV and pulse length  $T = 80$  fs. While total electron depletion is reached, a preferred ionization path is not evident for this regime.

resulting calculated spectrum in Fig. 4.9 shows a mixture of features from the last two limiting cases. The photoelectron contribution shows both a triangular peak, just not as developed as for the fast photoionization regime, as well as a step at  $E_{\text{trap}}$  due to the screening from trapped Auger electrons. The Auger electron contribution on the other hand, shows once again a plateau which in this case does not mimic perfectly the photoelectrons, having a smaller height. This implies that compared to the fast autoionization regime, fewer Auger electrons are able to escape which in turn favors a stronger plasma peak near zero.

The number of escaped Auger electrons can be determined by noting from the spectrum that  $E_{\text{min},6}^{\text{ph}} \approx 470$  eV, which requires a total charge  $Q \approx 262$  that is composed by 238  $e^{\text{ph}}$  and 24  $e^{\text{a}}$  in agreement with the numerical results. We can also cross check this estimate by comparing the height of the Auger contribution with that of the fast autoionization case for which we know the number of Auger electrons, obtaining a similar result.

We can summarize by saying that the amount of information that can be extracted just by identifying a few features in the electron spectrum is quite remarkable. For example the triangular peak at the blue edge of the photoelectron contribution is a clear feature that indicates fast photoionization, and it starts appearing whenever the pulse intensity is comparable to the Auger decay rate. This necessarily has to be accompanied by a suppression of the Auger electron spectrum due to trapping and a relative high

value for  $E_{\min}^{\text{ph}}$ . On the other hand for the fast autoionization regime we would have plateaus in both photoelectron and Auger contributions, a step starting at  $E_{\text{trap}}$  for the photoelectrons and a deeper trapping potential reflected in a lower  $E_{\min}^{\text{ph}}$ .

### 4.2.3 Influence of Ionic Motion in the Multiple Ionization of Fullerene

Through the previous results from our studies with rate equations and fixed ions molecular dynamics we have obtained a good amount of understanding and intuition regarding multi-channel ionization in fullerene. With this in hand we are now in a favorable position to proceed with the study and interpretation of the truly complex electron spectra of the fullerene  $\text{C}_{60}$  resulting from the full electronic and ionic dynamics triggered by an intense XFEL pulse. To this end we consider realistic parameters assuming a photon flux defined by an integrated intensity of  $10^{13}$  photons per pulse focused onto  $1 \mu\text{m}$ , experimentally achievable by current XFEL facilities. We also consider a photon energy of  $E_{\omega} = 1.3 \text{keV}$  photons, which will prove sufficient to retain a spectral gap between Auger and photoelectrons, resulting in roughly  $I_{\text{max}} \approx (2/T_{\text{fs}}) \times 10^{20} \text{W/cm}^2$ .

We start by making a connection with our previous fixed ions study using short pulses of  $T = 1 \text{fs}$  for several intensities, in which case the ionic movement should be relatively unimportant for the final spectrum. The results are shown in Fig. 4.10 for different intensities along with two excerpts for high and low intensities. For such short pulse lengths the weakest intensities can only produce a handful of photoelectrons as evidenced by the narrow peaks in both contributions from  $e^{\text{ph}}$  and  $e^{\text{a}}$ , slightly red shifted from their corresponding excess energies  $\mathcal{E}^{\text{ph}}$  and  $\mathcal{E}^{\text{a}}$  due to the shallow Coulomb potential.

As we increase the intensity more electrons are removed from the system and consequently a higher background charge  $Q$  is built, we observe the formation of both the familiar plateau for photoelectrons as well as the suppression of the Auger electron contributions due to trapping. Now it is clearly visible that the Auger suppression for high intensities is simply a progressive red-shifting of the Auger peak toward lower and lower energies until it leaves entirely the positive energy region.

At the highest intensities the characteristic triangular peak appears in the photoelectron spectrum as well as the plasma peak near zero, but a new feature also arises for the Auger in the form of broad spectrum and a sharp peak at relatively high energies ( $E \approx 200 \text{eV}$ ). By looking only at the spectra at high intensities this might seem to be in contradiction with our previous results from the fast autoionization regime, where we would expect a complete suppression of the Auger contribution. Due to the similarities of the positions and shapes of the Auger peaks at both weak and high intensities we might be tempted to suggest they are related and some kind of reemergence of this feature takes place. However, by inspecting the intensity dependence of the spectra we find that this Auger peak at high intensities behaves in a way not previously encountered.

We have seen that the position and height of the Auger contribution depends on the charge  $Q$  and therefore on the intensity  $I$ , but when the intensity reaches a value  $I \approx 10^{19} \text{W/cm}^2$  a second Auger peak appears whose position seems unaffected by the further increase of the background charge. This new peak appears close to the atomic



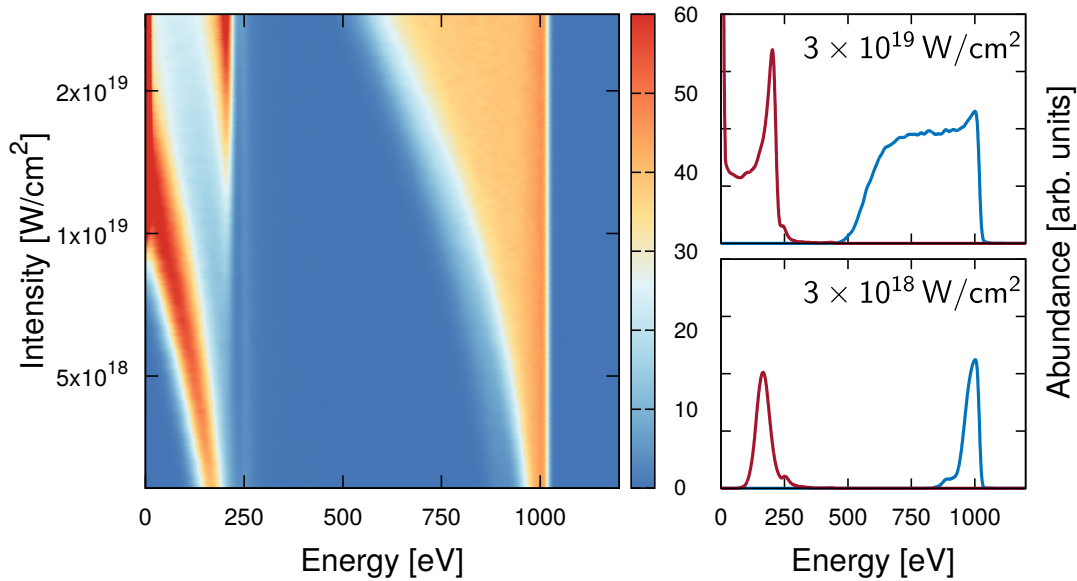


**Figure 4.10:** Electron energy spectra of the fullerene  $C_{60}$  obtained by molecular dynamics for a pulse length  $T = 1$  fs as a function of the intensity. Two particular spectra are shown along to present examples at low and high intensities.

line  $\mathcal{E}_4^a = 224$  eV already suggesting that it correspond to a different channel not previously accessible, requiring that the parent ion had undergone one Auger decay process beforehand. These two channels have different lifetimes, especially when considering high intensities where double core-hole states are prevalent. For a double core-hole  $C^{++}$  ion the Auger lifetime is just 3 fs according to our implementation, while the lifetime of a second Auger from a  $C^{+3}$  with a single core-hole varies between 30 and 70 fs. We can then infer that the different behavior of these two Auger channels has to be somehow linked to the different timescales.

At the beginning of the pulse as the system starts absorbing photons, the background potential is shallow as the system charge  $Q$  is small, being this the reason behind the small red shift observed for weak intensities. The background potential is also weak for late times, long after the pulse is terminated, as the induced Coulomb explosion disintegrates the molecule ( $R \rightarrow \infty$ ) driving the ions far apart from each other until their influence cannot be noticed anymore by any newly emitted electron. As the photoelectrons appear only during the short 1 fs pulse and the Auger electrons emitted from double core-hole states have a short lifetime, this effect is never experienced by any of them. This is not the case for the Auger electrons emitted from  $C^{+3}$  ions, appearing at such late times that the molecule is already destroyed, as evidenced by their sharp well defined peak.

It is now clear that nuclear motion can be very important for the final shape of the electron spectrum, even if only short pulses are involved. We investigate this effect further by analyzing electron spectra where we keep a constant peak intensity  $I = 10^{19}$  W/cm<sup>2</sup> with pulse lengths spanning from 1 fs up to 36 fs. The combined results

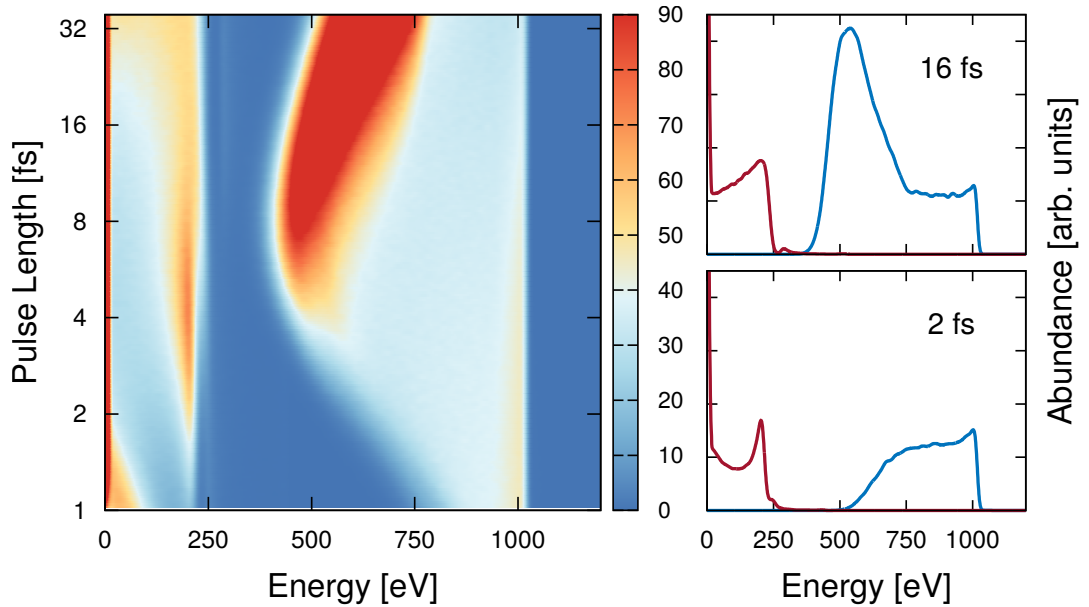


**Figure 4.11:** Electron energy spectra of the fullerene  $C_{60}$  obtained by molecular dynamics for a constant peak intensity  $I = 10^{19} \text{ W/cm}^2$  as a function of the pulse length. Two spectra are shown demonstrating typical behavior for short and long pulses.

of the simulations as well as two excerpts to illustrate short and long pulses are shown in Fig. 4.10, where we observe for the first time a non-monotonic behavior, both in the Auger and photoelectron contributions.

First we observe for the Auger electrons that short pulses have the expected behavior where the overall contribution is being suppressed due to the strong red shift, and the second Auger channel still does not play a significant role. This slowly changes for pulses as short as 2 fs where a small peak from the second Auger channel starts to show and keeps increasing with longer pulses. However, for pulse lengths of about  $T \approx 6$  fs, this second Auger peak starts to vanish and a broader and more regular distribution is observed. This very interesting and quite counter intuitive effect comes from the long lived single core-hole ion  $C^{+3}$ , which by the use of comparably long pulses is now still exposed to the XFEL beam and the next emitted electron is more likely to be a photoelectron and not an Auger. Therefore the creation of the double core-hole  $C_{++}^{+4}$  ion starts to be favored, and for this state the Auger rate is twice as fast with lifetimes ranging from 7 fs for the  $ss$  transition up to 30 fs for the  $sp$  one. In this way short pulses create long lived Auger decaying ionic states, while longer pulses enable a new Auger channel that decays in an intermediate timescale where it still can be affected by the time evolving potential, giving rise to this broader Auger spectrum for very long pulses.

As the pulse length becomes comparable to the ionic motion timescale, its influence start to be observed also in the photoelectron spectrum, which in Fig. 4.11 shows for the first time a qualitative difference with respect to previous scenarios. For short pulse lengths the familiar plateau and triangular peak shows up, and longer pulses bring along

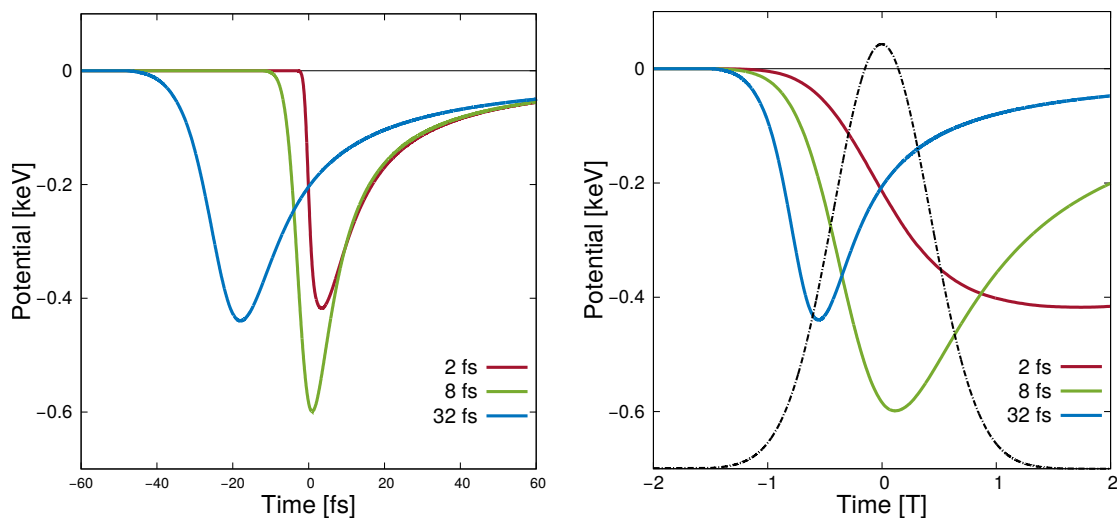


**Figure 4.12:** (a) Time-dependent background potential  $V(t)$  as given by (4.3), for a Gaussian pulse with peak intensity  $I = 10^{19} \text{ W/cm}^2$ . (b) Comparison of the same potentials with respect to the pulse envelope.

a broader spectrum and a less prominent peak on the blue edge of the distribution. The plateau keeps getting broader until for a pulse length of about  $T \approx 4 \text{ fs}$  a peak starts appearing at its red edge. From this point onwards longer pulses enhance this red edge peak while the broadening stops increasing until at  $T \approx 8 \text{ fs}$  the trend is reversed and the distribution starts to narrow.

In contrast to the Auger case, the change in the behavior of the photoelectron spectra is not caused by new available photoionization channels arising for longer pulses, it is instead a consequence of the temporal dependence of the background potential as shown in Fig. 4.12(a) led by two competing and opposite mechanisms. This can be stated more precisely using the time derivative of the potential which, according to equation (4.3), reads

$$\dot{V} = \frac{q}{R^2} \dot{R} - \frac{1}{R} \dot{q}, \quad (4.38)$$

where we can explicitly see the contributing terms. At the beginning of the pulse ( $t \rightarrow -\infty$ ) the ions have definite and stable positions ( $\dot{R} = 0$ ) and the change in the potential approximates to

$$\dot{V} \approx -\frac{1}{R} \dot{q}, \quad (4.39)$$

driven mainly by the electron removal  $\dot{q}$  from photoionization and Auger channels, being initially proportional to the pulse envelope. The charging rate  $\dot{q}$  eventually vanishes as the number of electrons in the system is finite, independently of how long or intense the laser pulse might be. The radial velocity  $\dot{R}$  on the other hand has to asymptotically approach a definite value as the molecule Coulomb explodes, but never vanishes. This

implies that as  $t \rightarrow \infty$  the potential changes according to

$$\dot{V} \approx \frac{q}{R^2} \dot{R}, \quad (4.40)$$

which entails that for later times

$$V(t) \approx -\frac{q}{\alpha + \beta t} \quad (4.41)$$

where  $\alpha$  and  $\beta$  are some integration constants. This explains why eventually the potential slowly decays, asymptotically approaching zero as time progresses.

A clearer picture of the interplay of these two effects in the photoelectron spectra can be obtained when the temporal development of the potential is compared to the pulse envelope, as done in Fig. 4.12(b) for the same three cases. For the short 2 fs pulse photoionization serves as the main contributor to the background potential buildup and it finishes before the ions can gain any significant radial velocity to weaken the potential. After the pulse is gone only autoionization processes remain to take place in a timescale where this potential reduction is relevant.

When intermediate pulse lengths such as 8 fs are used, both mechanisms have similar timescales and we observe that the minimum of the potential almost coincides with the maximum of the pulse. Quite remarkably, it is under this condition that the potential seems to reach its deepest minimum and consequently the photoelectron spectra achieve their broadest distributions. The potential then weakens for later times and, as roughly half of the pulse remains to arrive, the following emitted photoelectrons require less energy to escape the system. The slowly decreasing potential leads to a progressively closer bunching of the photoelectrons, as their energy varies less with respect to their emission times.

Finally for long pulses like the 16 fs one shown, the system gets significantly charged in a very early stage and the ions have enough time to gain sufficient speed and lead the time development of the potential for most of the pulse. This prevents such deep minima to be reached, and progressively narrows the energy interval of the photoelectron part of the spectrum. The main part of the pulse arrives into a decreasing Coulomb potential, and the created photoelectrons achieve higher energies and are piled up more closely in the spectrum due to the smaller differences in their energies. As progressively longer pulses are used, more electrons are emitted into this diminished potential and contribute to this peak, which slowly and continuously moves towards higher energies (limited of course by the  $\mathcal{E}_6^{\text{ph}}$  excess energy).

### 4.3 Dynamical Footprints of Auger Decay Rates

Through the previous sections we have been able to recognize which parameters are relevant for the multi-channel ionization of fullerenes, their interplay, the effect it has on the dynamics, and how that is reflected in the electron energy spectra. From the very first steps we found that at the core of many of the observed phenomena lies autoionization

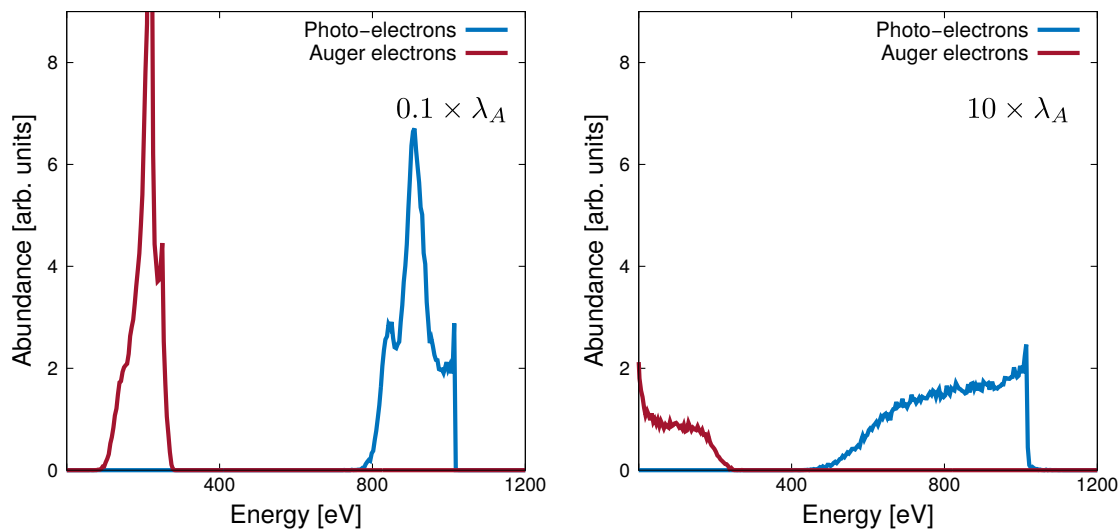


**Figure 4.13:** Comparison of two spectra with the same ratio  $\Gamma/\lambda$  and the same amount of photoelectrons  $\Gamma T$  obtained with MD calculations for fullerenes, assuming different Auger rates.

as an important process that not only influences the dynamics but actually enables some of the most interesting encountered features. From our rate study, for example, we were able to obtain many different spectral shapes by changing the ratio  $\Gamma/\lambda$ , which can be done by changing the pulse intensity. This would not be possible if the only ionization channels available were the photoionizing ones, as we would find that the ratio of photoionization rates would have fixed values, independently of both the pulse shape and intensity (provided multiphoton ionization can be neglected).

Additional results from our MD studies with fixed ions seemed to further confirm this ideas, as all the characteristics and features of the spectrum are solely determined by the ratio  $\Gamma/\lambda$  and the total number of photons in the pulse<sup>5</sup>. Of course, this is a big oversimplification as observed in the full MD calculations, where it is clear another timescale comes into play. The addition of this new timescale, due to the movement of charged ions, implies that systems with different autoionization rates have completely different spectra even with the same  $\Gamma/\lambda$ , and an appropriately scaled pulse. This can be seen in Fig. 4.13 where a spectrum of a fullerene has been calculated artificially assuming Auger rates smaller and higher by a factor of 10 than the atomic carbon rate, yielding different spectra with almost no resemblance.

However, even if several observables are different for the two spectra shown, like the minimum photoelectron energy or the average energy of Auger electrons, there is one quantity that remains the same in both cases, that is the number of photoelectrons. The number of emitted electrons is governed by a system of coupled differential equations similar to those in (4.8), where clearly particle movement has no influence, making it a robust quantity. Strictly speaking this system of equations also implies that the

<sup>5</sup>Provided the same pulse shape is used, and the plasma evaporation from the trapped Auger electrons can be neglected.

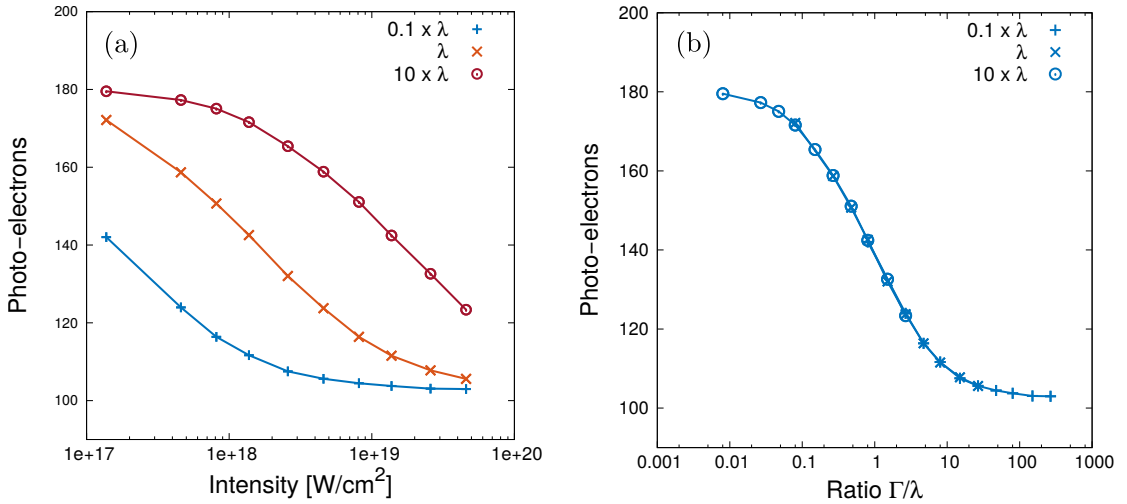


**Figure 4.14:** (a) Number of photoelectrons obtained from microscopic MD calculations as a function of the pulse intensity, for three different Auger lifetimes. (b) Same microscopic results now as a function of the ratio  $\Gamma/\lambda$ .

number of Auger electrons and the ionic charge states are also the same, but the Auger trapping ultimately leads to recombination, changing the final ionic charges and making the number of emitted Auger electrons difficult to measure.

We have already found that by tuning the pulse length and intensity, the autoionization rate  $\lambda$  acts as a gate that regulates the amount of emitted photoelectrons and determines which ionization channels are allowed. This is clearly seen in Fig. 4.14(a), where the number of photoelectrons is shown with respect to the pulse intensity for three fullerene-like systems where we have assumed different Auger lifetimes. We have kept a constant number of photons, which means that lower intensities imply long pulses and correspondingly high intensities imply short pulses. For all three cases we can see that the number of photoelectrons increases for smaller intensities, where the pulse is long enough to allow for the refilling of the core-shells, increasing photoabsorption. It also follows that short and intense pulses favor double core-hole states, which are essentially transparent to the pulse, frustrating photoabsorption and decreasing the number of emitted photoelectrons. While these results clearly depend on the Auger lifetime, we observe in Fig. 4.14(b) that expressing them in terms of the ratio  $\Gamma/\lambda$  collapses all three cases into one single curve, uniquely defined by the amount of photons in the pulse.

All the previous features would not be possible without the presence of autoionization processes in the system, as it is precisely the interplay between the Auger decay and photoionization what originates them, independently of the particular shape of the molecule or the induced potential. A proper understanding of this behavior, despite its simplicity and due to its generality, could potentially be used in order to obtain information about the ionization processes present in an arbitrary system.

### 4.3.1 Bottle-Neck Model of Multi-channel Ionization

The simplest model that can describe the competition between both ionization processes is a three step “bottle-neck model”, where the Auger decay acts like an intermediate gate between two subsequent photoionization events (see scheme in Fig.4.15). Such system is described by the following set of rate equations

$$\begin{aligned}
 \dot{N}^0 &= -\Gamma(t)N^0, \\
 \dot{N}^1 &= \Gamma(t)N^0 - \lambda N^1, \\
 \dot{N}^2 &= \lambda N^1 - \Gamma(t)N^2, \\
 \dot{N}^3 &= \Gamma(t)N^2.
 \end{aligned}
 \tag{4.42}$$

This set of equations, being first order and linear, admits a scaling of the form

$$\begin{aligned}
 \tau &= \lambda t, \\
 \tilde{\Gamma} &= \frac{\Gamma}{\lambda},
 \end{aligned}$$

which yields

$$\begin{aligned}
 \dot{N}^0 &= -\tilde{\Gamma}(\tau)N^0, \\
 \dot{N}^1 &= \tilde{\Gamma}(\tau)N^0 - N^1, \\
 \dot{N}^2 &= N^1 - \tilde{\Gamma}(\tau)N^2, \\
 \dot{N}^3 &= \tilde{\Gamma}(\tau)N^2.
 \end{aligned}
 \tag{4.43}$$

Here we have used the notation  $\dot{N}^i$  to emphasize the derivatives with respect to the scaled time. The total number of photoelectrons in turn is also given in a scaled version as

$$\dot{n}^{\text{ph}} = \tilde{\Gamma}(\tau) \left( N^0 + N^2 \right).
 \tag{4.44}$$

These scaled equations immediately explain not only the behavior observed in Fig. 4.14 but also the importance of the ratio  $\Gamma/\lambda$  in section 4.1.1, found in the dynamics for two channels.

In order to obtain an explicit solution we assume rectangular pulses of finite length, which implies a constant photoionization rate  $\tilde{\Gamma}$ . For the case of the fullerene  $C_{60}$  we

have the conditions  $N_0 = 120$  and  $N^{+1}(0) = N^{+2}(0) = N^{+3}(0) = 0$ , yielding the solution

$$\begin{aligned}
N^0 &= N_0 e^{-\tilde{\Gamma}\tau}, \\
N^{+1} &= \frac{N_0 \tilde{\Gamma}}{\tilde{\Gamma} - 1} \left( e^{-\tau} - e^{-\tilde{\Gamma}\tau} \right), \\
N^{+2} &= \frac{N_0 \tilde{\Gamma}}{(\tilde{\Gamma} - 1)^2} \left( e^{-\tau} - e^{-\tilde{\Gamma}\tau} - (\tilde{\Gamma} - 1) \tau e^{-\tilde{\Gamma}\tau} \right), \\
N^{+3} &= N_0 - \frac{N_0 \tilde{\Gamma}^2}{(\tilde{\Gamma} - 1)^2} e^{-\tau} + \left( \frac{2\tilde{\Gamma} - 1}{(\tilde{\Gamma} - 1)^2} + \frac{\tilde{\Gamma}\tau}{\tilde{\Gamma} - 1} \right) N_0 e^{-\tilde{\Gamma}\tau}.
\end{aligned} \tag{4.45}$$

From this we obtain finally an expression for the number of photoelectrons at the end of a pulse of length  $\tau$  as

$$n^{\text{ph}}(\tilde{\Gamma}, \tau) = 2N_0 - \frac{\tilde{\Gamma}^2}{(\tilde{\Gamma} - 1)^2} N_0 e^{-\tau} - \left( 1 - \frac{2 + \tilde{\Gamma}\tau}{\tilde{\Gamma} - 1} - \frac{1}{(\tilde{\Gamma} - 1)^2} \right) N_0 e^{-\tilde{\Gamma}\tau}. \tag{4.46}$$

This function is shown in Fig.4.15, for different values of pulse length and photoionization rates.

When the fullerene  $\text{C}_{60}$  is completely depleted from its electrons every single carbon atom has absorbed 4 photons, accounting for a total of 240 photoelectrons. This is achieved independently of the intensity provided that the pulse acts on the system for a sufficient amount of time ( $T \rightarrow \infty$ ), as denoted by the homogeneous region at long pulse lengths. However, another homogeneous region can also be observed at short and very intense pulses, where the number of emitted photoelectrons is about 120. This implies that depending of the intensity there are two qualitatively different paths to reach complete saturation, for either  $\tilde{\Gamma} \rightarrow 0$  or  $\tilde{\Gamma} \rightarrow \infty$ . For low photoionization rates  $\tilde{\Gamma}$  the equation (4.46) reads approximately

$$n^{\text{ph}}(\tilde{\Gamma} \rightarrow 0, \tau) = 2N_0 - \left( 2 + \tilde{\Gamma}\tau \right) N_0 e^{-\tilde{\Gamma}\tau}, \tag{4.47}$$

meaning that complete electron depletion occurs in one single step for pulse lengths on the order of  $T' = 1/\Gamma$ , and does not depend on the Auger decay rate  $\lambda$ . In contrast, for the limit of large photoionization rates induced by high intensities, equation (4.46) reduces to

$$n^{\text{ph}}(\tilde{\Gamma} \rightarrow \infty, \tau) = 2N_0 - N_0 e^{-\tilde{\Gamma}\tau} - N_0 e^{-\tau}, \tag{4.48}$$

for which we observe that saturation takes place in two steps, namely at pulse lengths of the order of  $T' = 1/\Gamma$  and  $T'' = 1/\lambda$ , where  $T' \ll T''$ . Hence, for pulse lengths  $T \in [T', T'']$ , the number of emitted photoelectrons remains fairly constant, as the Auger decay acts precisely as a bottle-neck, preventing the second photoabsorption from happening.



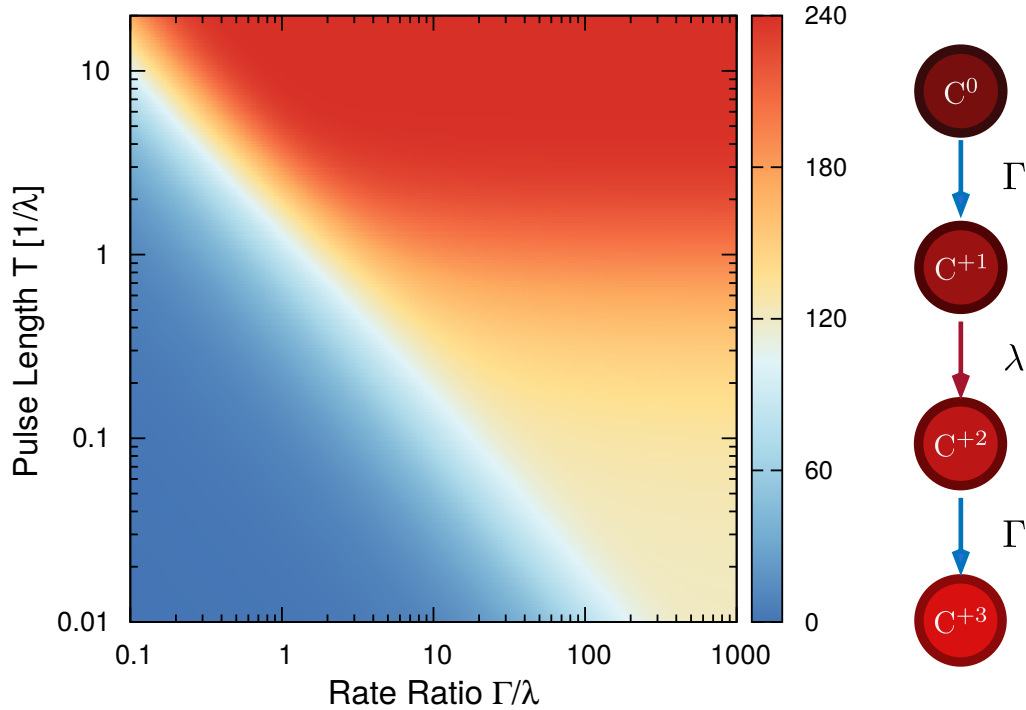


**Figure 4.15:** Number of photoelectrons according to the “bottle-neck model”, as given by the equation (4.46). The Auger lifetime ( $1/\lambda$ ) is used to define the timescale.

For a proper comparison with our results with constant number of photons of equation (4.46), we extract the appropriate paths with a parametrization in terms of the ratio  $\xi = \Gamma/\lambda$  and the total number of photons  $\eta = \Gamma T$  as

$$n^{\text{ph}} = 2N_0 - \frac{\xi^2}{(\xi - 1)^2} N_0 e^{-\eta/\xi} - \left( 1 - \frac{2 + \eta}{\xi - 1} - \frac{1}{(\xi - 1)^2} \right) N_0 e^{-\eta}. \quad (4.49)$$

Three paths obtained through this equation along with the corresponding microscopic MD calculations for Gaussian pulses with  $E_\omega = 1300$  eV are shown in Fig. 4.16 over a wide range of ratios  $\xi$  for the case of  $\eta = \{1, 2, 4\}$ , showing a remarkably good agreement for such a simple model. An interesting feature that can be observed is that the transition between the limiting values for high and low intensities, always seem to take place when the pulse length is of the order of the Auger lifetime.

This behavior could potentially be used to measure the Auger decay rate not only for fullerene, but for any molecular or atomic system, regardless of the peculiarities of their geometry or bond nature. In the same way, a similar behavior could be expected for other autoionization mechanisms such as Coster-Kronig or more intriguing and elusive processes like inter-atomic Coulomb decay (ICD) or electron transfer mediated decay (ETMD).

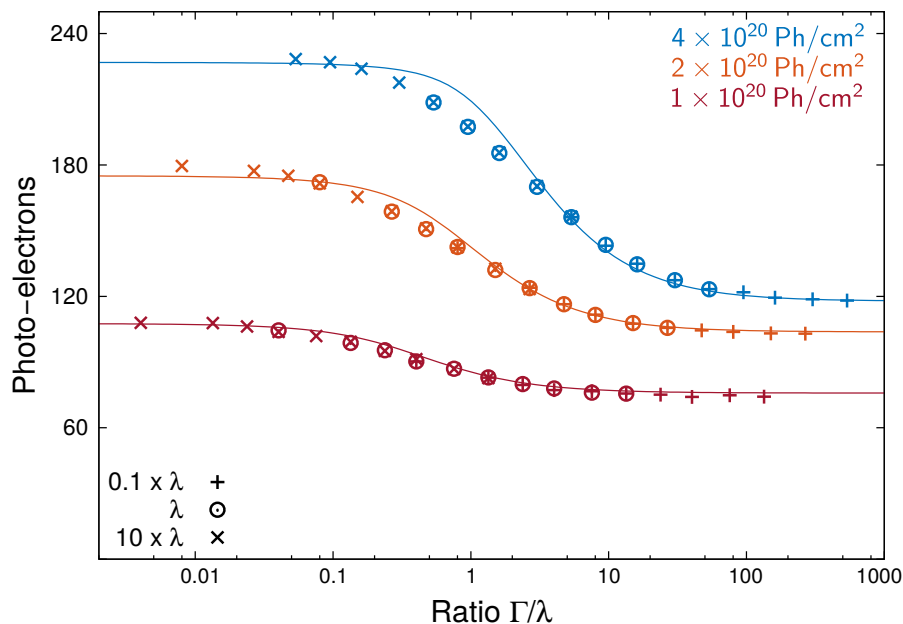


**Figure 4.16:** Number of photoelectrons from microscopic MD calculations for fullerene at several photon fluxes (corresponding to different colors) and Auger rates (indicated by different symbols) as a function of the ratio of photo-ionization and Auger rates. They are compared to the curves obtained with the “bottle-neck model” according to equation (4.49) for  $\eta = \{1, 2, 4\}$ .

## 4.4 Conclusions

We have analyzed the multi-channel ionization dynamics of fullerenes illuminated by short and intense X-ray pulses, as revealed through its electron spectra. The relevant parameters that explain general characteristic features have been identified. They will permit a simpler interpretation of spectra from bigger and perhaps less symmetric and inhomogeneous molecules. From the very first steps we have identified the ratio  $\Gamma/\lambda$  as a fundamental parameter to describe spectral features. In particular, the triangular shapes observed for two channels where the first is twice as likely as the second, serves as a clear indication of the formation of double core-hole states.

The photoelectron contribution to the spectrum carries also a fair amount of information from the Auger dynamics, as the presence of a step increase at  $E_{\text{trap}}$  indicates that some  $e^a$  were capable to escape the system before a sufficiently deep potential could trap them. The number of escaped Auger electrons, an otherwise elusive quantity, can be determined for short pulses through the onset  $E_{\text{min}}^{\text{ph}}$  with good precision.

The characteristic features like the triangular shapes and the plateaus survive even when ionic motion is included, as evidenced by studies with full MD calculations, where the influence of ionic motion is clearly observed in the spectra. In this case the onset energy  $E_{\text{min}}^{\text{ph}}$  also carries information about the depth of the time-dependent Coulomb potential, which achieves a minimum due to the competing opposite effects of charging and ionic motion. This might enable alternatives ways to study the Coulomb explosion

undergone by the ions.

Several of the mechanisms responsible for the observed features are general and quite robust, and therefore similar effects should be expected in other less symmetric molecules. In particular, we have proposed that the number of photoelectrons might be used as an alternative way to measure autoionization rates.



## Chapter 5

# Charge Migration in XFEL Diffractive Imaging

Perhaps one of the most ambitious goals for XFEL facilities is the achievement of single molecule diffractive imaging with atomic resolution, a feat traditionally considered to be essentially impossible [72] until the turn of the century, as the radiation dose needed would inevitably destroy the molecule. This phenomenon is commonly referred to as radiation damage and is a frequently encountered problem in X-ray crystallography, being a mayor issue in the structure determination of macromolecular crystals with synchrotron radiation. Several techniques have been developed in order to mitigate this effect, both experimentally such as the use of cryogenic temperatures [73] or theoretically by explicitly including radiation damage effects into the phasing problem algorithms [74–76], with some degree of success. For example, the use of cryogenic cooling slows down some of the reactions triggered by photoabsorption, allowing for an increase of 30 to 50 times in the exposure. However, recent results have determined a radiation dose limit on the order of  $3 \times 10^7$  Gy [77] for this technique, which is still insufficient not only for single particle imaging (SPI) but also for large macromolecular assemblies and membrane proteins which are difficult to handle and crystallize and for which the necessary diffraction quality is hard to obtain. Furthermore, as typical synchrotron experiments can have exposure times ranging from several minutes up to some hours, concern has been raised recently that some inaccurate structures could have been deposited in the Protein Data Bank as radiation sensitive targets could have experimental artifacts from photo-reduction reactions [78].

The use of XFEL sources enable much higher doses to be reached, on the order of  $1 \times 10^9$  Gy or even higher, opening the possibility of structure determination at room temperature from smaller samples. The short pulses delivered by these facilities ensure that only the native structure is measured, being potentially free of radiation damage, and any structural change could possibly be temporally resolved by pump-probe techniques. Nevertheless the sample is inevitably destroyed in the process but not before a scattering signal can be produced and recorded. This requires that a series of diffraction patterns have to be measured to obtain a large enough set of data from which the

structure can be deduced. The individual patterns obtained with each shot have to be identified, indexed and integrated to build up a significant diffraction signal, averaging out the background noise and other non-systematic sources of error in the process.

In the same way as in the case of X-ray crystallography, a proper understanding of the dynamics under XFEL pulses is fundamental in order to assess the radiation damage limits, to correctly interpret data, as well as to determine experimental parameters and develop phasing methods. Adding to the phenomena of multiple-channel ionization, electron trapping and screening, observed and studied in previous chapters, we find that further complications arise when dealing with proteins and other complex macromolecules as they do not present a particularly symmetric geometry, usually have an inhomogeneous spatial distribution, and they are composed from different atomic species with different electronic properties. Unlike synchrotron experiments where the only way to modify the ratio between scattering and photoabsorption is through the use of different wavelengths, when using XFEL facilities we encounter a highly non-linear regime where more parameters come into play, such as the intensity and pulse length, making it indeed a truly complex problem.

In this final chapter we aim at studying the XFEL diffractive imaging scheme from the point of view of the ionization dynamics, making special emphasis on the impact of charge migration and ionic motion on the final diffraction data. We start by reviewing the concept of diffraction-before-destruction (also referred sometimes as diffract and destroy) as originally proposed, as well as some recent experimental results in serial femtosecond crystallography (SFX) and recent advancements towards single particle imaging. We also discuss the very interesting effects of fast proton ejection observed in clusters, which helped defining the direction of our studies and motivated the inclusion of the effect of charge migration into our simulations. We proceed by giving the details of our molecular dynamics studies and analyzing its results, focusing in particular into the differences that arise by the inclusion of charge transfer, for different pulse lengths, intensities and atomic species. The diffraction patterns are constructed for several conditions and the influence of ionic movement is assessed for each one, using the  $R$  factor to have a measure of the scattering data quality. We finalize by focusing on specific trajectories in heavy ions, and discuss certain possibilities regarding molecule orientation, which is fundamental to the phasing problem.

## 5.1 Diffraction before destruction

As soon as the achievement of free electron lasers in the X-ray regime started to be regarded as a very real possibility thanks to the technological advancements, a considerable amount of theoretical effort was put into the task of predicting its potential applications. One of the most promising results came from the highly regarded work of Neutze and coworkers [79], where it was claimed that the ultrashort and ultrabright pulses delivered by XFELs would enable the recording of interpretable diffraction data from single molecules and very small crystals. Although the idea that extremely intense X-rays can be used to image biological samples have been previously suggested [80,81], the previous

discussions lacked quantitative analysis and considered the hydrodynamic expansion of the sample as the main limitation, therefore erroneously requiring milder experimental conditions. Neutze and coworkers were the first to evaluate the influence of radiation damage over the structure of the target, including several mechanisms for energy deposition in a molecular dynamics simulation such as photoabsorption and Compton scattering, as well as Auger emission from atomic lifetimes, taking into account photon energy, pulse length, intensity and sample size. These ionization mechanisms were described stochastically through time dependent probabilities, and the ions were propagated according to classical mechanics. The electrons, which influence the dynamics by impact ionization as well as by trapping and screening, were not considered. This model was applied to a set of three different targets: a T4 lysozyme as a single particle along with a solvent envelope, a  $5 \times 5 \times 5$  lysozyme nanocrystal, and to the capsid protein of the tomato stunt virus. They observed from their results that by using very high X-ray intensities and exposure times on the order of a few femtoseconds the radiation dose tolerance was several orders of magnitude higher compared to conventional X-ray diffraction experiments [82].

These results promptly triggered a broad discussion and research in several areas, starting from the development of alternative models for radiation damage in XFEL pulses using and occasionally combining Monte Carlo methods, PIC codes [83], molecular dynamics [84], hydrodynamical models [85] and even DFT calculations [86], using different degrees of sophistication and sometimes with mixed results. Other experimental issues were also motivated adopting techniques from other methods and developing new ones in sample-handling [87–90], data analysis and phasing methods [91,92] among others, being applied as soon as XFEL facilities became available. Proof of principle experiments were promptly performed using UV wavelengths to image nanostructures [93–95], showing no measurable damage and confirming the feasibility of single-particle diffractive imaging.

The initial skepticism from the structural biology community has vanished considerably after a series of experiments initiated just 5 years ago [96] has combined all the previous efforts to give shape to a new technique denominated serial femtosecond X-ray crystallography (SFX). Among the milestones already reached by this technique are the use of *in vivo* crystallization techniques [17,97,98], the achievement of atomic resolution [99], and time-resolved studies on photoactive systems [15,16,100]. This technique has enabled new research opportunities, allowing dozens of new studies in structural biology and it is expected to influence other branches of science.

On the other hand single particle imaging is still in development and, while some interesting experimental results have already been obtained such as the imaging of whole single viruses [13], cells [101] and even cellular organelles [12], no experiments with the required resolution for molecular structures have been performed. It is indeed a very challenging problem as the high photonic energies (around 10 keV) needed for atomic resolution usually lead to a significant decrease in the fluence when dealing with pulse lengths shorter than 10 fs. Nevertheless, with the current understanding of the underlying phenomena, there appears to be no fundamental constrain that forbid SPI to be achieved and a huge effort is already taking place to overcome the experimental chal-

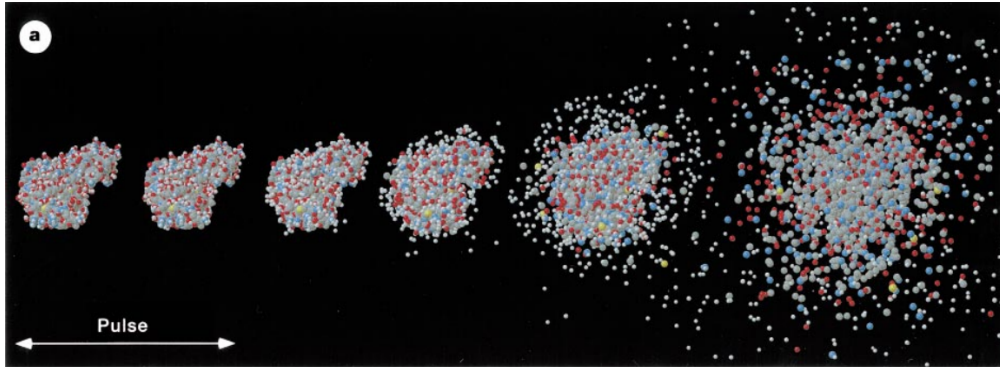


**Figure 5.1:** Coulomb explosion of T4 lysozyme as determined by [79] when exposed to a  $T = 2$  fs pulse with  $E_\omega = 12$  keV photons. While the structure is finally lost for long times, no appreciable displacement is observed for the time window of the pulse.

lenges [102]. From the theoretical point of view more studies are needed to further understand the dynamics of complex molecules in order to determine optimal experimental conditions, identify the impact of the dynamics into the scattered data and perhaps help to develop new phasing schemes or new experimental procedures.

## 5.2 Charge Transfer in Heterogeneous Clusters

At the same time as the previous results were being obtained, research was being made in order to better understand the dynamics of clusters under XFEL pulses. While these systems are genuinely interesting in their own right, some of the motivation behind it was due to the fact that they could provide valuable information for single particle diffractive imaging by working as proxy systems for big polyatomic molecules, and many interesting and intriguing results have been obtained.

While in the X-ray regime tunneling and field ionization from the incoming laser can safely be neglected, it was found by studying rare gas clusters that under short pulses a high enough charge could be built such that ionization by the resulting strong coulombic field could play a significant role [103]. Through this effect the cluster evolves into a core-shell system, where the inner core remained almost static while the outer shell explodes. This quickly prompted the idea that in order to slow down the coulomb explosion of the system of interest a sacrificial layer of a weakly diffracting material such as helium could be used [103–105], reducing with this the radiation damage effects during diffractive imaging.

Later experiments performed using large protonated systems [106] such as  $\text{CH}_4$  clusters of different sizes showed an even more surprising effect. Despite the fact that the main absorbers in such systems are the carbon atoms, a considerably large number of protons was detected while only a small amount of heavier carbon atoms with low charge states was observed. A further theoretical study [55] of composite clusters along the iso-electric sequence of  $\text{CH}_4$ ,  $\text{NH}_3$ ,  $\text{H}_2\text{O}$ , and Ne, showed that this proton ejection was a



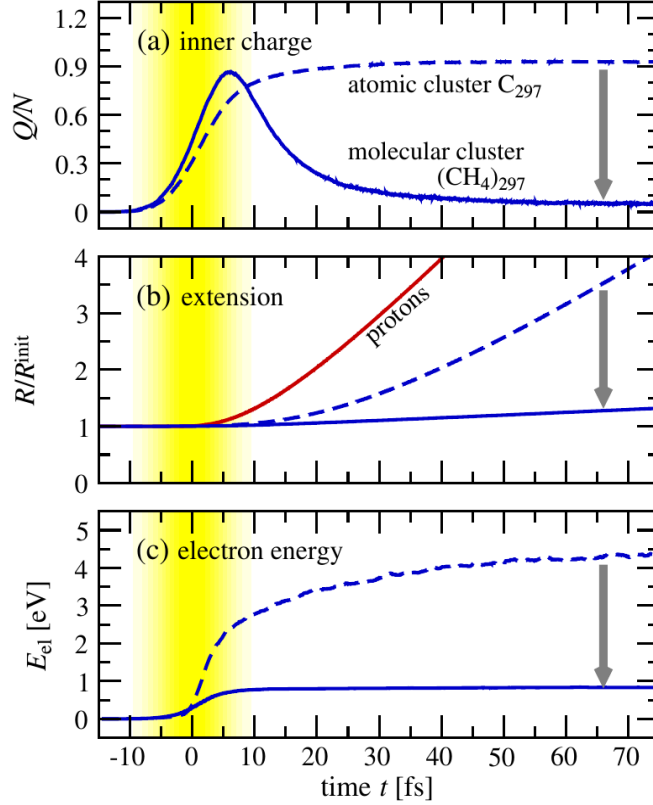


**Figure 5.2:** Time evolution of a molecular  $\text{CH}_4$  cluster (solid line) and an atomic carbon cluster (dashed line), when shined by an X-ray pulse ( $I = 10^{18} \text{ W/cm}^2$ ) of 10 fs length. (a) Charge contained within the cluster, defined by the outermost carbon atom. (b) Average radius, with the proton part shown in red. (c) Average kinetic energy of the trapped electrons. Proton ejection has a clear influence in all the observables. Taken from [55].

universal feature among the hydride clusters, while the atomic cluster had very different dynamics. This proton emission provides an additional and very efficient channel of energy release, significantly cooling the residual nanoplasma in comparison with similar pristine atomic clusters. For certain experimental conditions it was possible that the heavier ions could emerge with neutral charge due to recombination, despite the energetic pulse. All this has important consequences for the time evolution of the remaining heavier atoms, as we can observe in Fig. 5.2 that there is a big difference for the inner charge, the expansion dynamics, and plasma temperature, implying a fast recombination and neutralization that is absent in the case of the atomic cluster.

These previous results strongly contrast with some of the original observations of Neutze et. al., as in their study the explosion is mainly led by highly charged sulphur ions and a very small amount of protons. Not only that, but other subsequent studies found that the inhomogeneous nature of biological molecules [84] would produce a strong local distortion around heavy atoms and density fluctuations. According to this, the

amount of information that could possibly be retrieved by single-particle experiments would be unreliable and the use of tamper layers would not be able to overcome this issue. Some different results from water tampered proteins simulations also imposed further limitations to the use of tamper layers [107], claiming that this method would only be effective if the layers are composed of photoionizing materials, implying that He layers would provide no benefit.

We can clearly observe that there are two main differences between these two opposite assertions. On one side there is the inclusion of electronic dynamics, field ionization and charge transfer, all of them electronic phenomena often not included when dealing with biological molecules. On the other hand, the most interesting systems for structural studies have many inhomogeneities and are usually not very symmetric, for which few simplifications can be made. In order to have a realistic picture of the actual dynamics it is therefore necessary to study a realistic, inhomogeneous and composite system, for which the electronic phenomena should be properly included. In the following sections we attempt to achieve such a description and determine the correct behavior of a realistic system.

### 5.3 Charge Migration in Biomolecules

We observed in the previous section that the inclusion of charge transfer mechanisms is fundamental to properly understand and reproduce the dynamics of complex systems under XFEL pulses. Therefore in our study we will consider besides the usual channels of photoabsorption and Auger decay, already introduced in chapters 3 and 4, a new channel in the form of field ionization.

Field ionization occurs when the external electric field acting over an electron is higher than the one exerted by the parent atom. For any atom this channel would affect first and foremost its outermost electron and, while in principle it is possible for this channel to induce multiple ionization events removing further electrons, we will limit this effect to occur at most once for each atom. This outermost electron is considered here as a classical particle located in a potential centered at the parent ion. In order to avoid the issues of numerical instability caused by the Coulomb potential singularity, the potential exerted by a specific ion  $i$  at a distance  $r$  is modeled as follows

$$V_i(r) = -\frac{q_i(1 - e^{-\alpha_i r})}{r}, \quad (5.1)$$

where  $q_i$  is the effective charge of the ion and  $\alpha_i$  is a parameter that determines the dept of the potential. This potential is depicted in Fig. 5.3 where we observe that the singularity at  $r = 0$  is replaced by a minimum given as  $V_i(0) = -q_i\alpha_i$ , while retaining the long range of the coulombic interaction. For a neutral atom the effective charge felt by its outermost electron is  $q = 1$ , implying that  $\alpha_i = E_{b,i}$  is the binding energy or ionization potential. While in general for a complex multicomponent molecule the ionization potential  $E_{b,i}$  would be different for each one of the constituent atoms, as it is affected by the molecular environment, here we consider it to be well approximated by the ionization potential of the atomic case for each species.

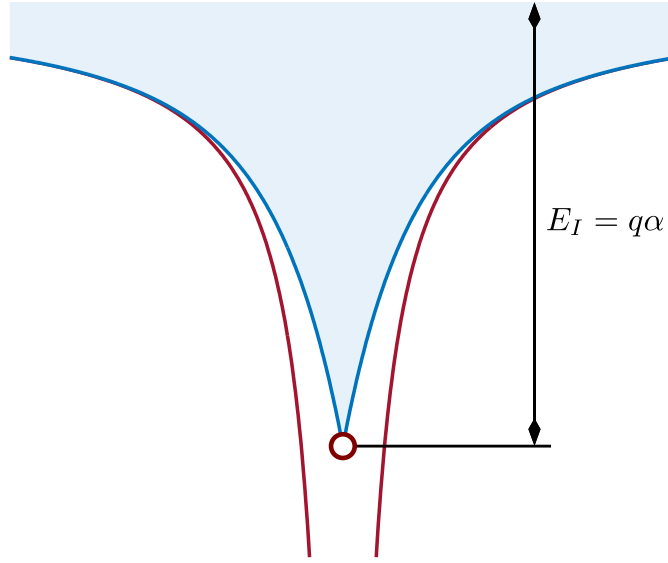


**Figure 5.3:** Comparison between the usual Coulomb potential for a single charged ion (red) with respect to the potential defined by equation (5.1), used in the simulations (blue). Unlike Coulomb's, our proposed potential features a finite and well defined value at the origin, directly related to the ionization potential.

The potential (5.1) has another useful characteristic due to the fact that its first derivative does not vanish at  $r = 0$ . As a consequence any infinitesimal displacement of the electron from its equilibrium position will be promptly counteracted by a restoring force given by

$$\mathbf{F}_i(0) = -\nabla V_i(r)|_{r=0} = -\frac{q\alpha^2}{2} \hat{\mathbf{r}}, \quad (5.2)$$

where  $\hat{\mathbf{r}}$  is a unit vector in the direction of the displacement. This implies that for sufficiently small perturbation the electron will remain confined in an infinitesimal region centered at the parent ion. This gives naturally a condition for field ionization, as an atom in an electric field would then lose its outermost electron if

$$|\mathbf{F}_{a,i} - \mathbf{F}_{e,i}| \geq q\alpha_i^2, \quad (5.3)$$

where  $\mathbf{F}_a$  and  $\mathbf{F}_e$  are, respectively, the forces experienced by the parent atom and its corresponding electron, which in our numerical implementation are not necessarily equal.

Regarding the other ionization processes, here we consider for all the following results a photon energy  $E_\omega = 10 \text{ keV}$  with the corresponding atomic photoabsorption cross sections, and typical Auger lifetimes of the different species in a (organic) molecular environment. The values of all these relevant ionization properties are summarized in table 5.1 for the usual atomic components of biological systems, as implemented in the simulations.

Even if sub-shell Auger rates and branching ratios are usually not available for most atoms, particularly when immersed in a molecular environment, it is clear that as the

Element	Photoionization	Auger Decay	Ionization
	Cross Section $\sigma_{\omega @ 10\text{keV}}$ [Barn]	Lifetime $\tau_A$ [fs]	Potential $E_b$ [a.u.]
Hydrogen	0.0045	—	0.5
Carbon	41.4	6.0	0.41
Nitrogen	82.4	4.6	0.53
Oxygen	147.9	3.0	0.5
Phosphorus	2037	3.0	0.38
Sulphur	2625	3.0	0.38

**Table 5.1:** Summary of the photoionization cross-section, Auger decay lifetimes, and ionization potentials of the valence shell for some of the most commonly encountered species in biological systems, as implemented in the simulations.

atoms get increasingly charged and lose electrons the corresponding Auger rates have to be modified as the number of channels decrease. To this end we estimate the modified Auger rate  $\lambda'_i$  for a given ion with  $n$  electrons available in its external shells using a counting argument [55] as follows

$$\lambda'_i(n) = \lambda_i \frac{n(n-1)}{N(N-1)}, \quad (5.4)$$

where  $\lambda_i$  is the usual Auger decay rate for a singly charged ion with one core vacancy, and  $N$  is the number of electrons in the external shells of the neutral species. It is clear from (5.4) that  $\lambda_i \geq \lambda'_i \geq 0$ , and that no transition is allowed for the case of  $n \leq 1$ , reflecting the two electron nature of the process. For the case of double core-hole states we make the same assumption as in the previous chapter and simply regard it as twice the rate of the single core-hole state, for the same valence configuration.

Once again we simulate both the photoionization and Auger decay processes in a Monte Carlo fashion, with the difference that due to the high kinetic energy of the photoelectrons, we assume they are instantly removed from the system and in consequence they are not propagated. We do, however, propagate both the field ionized and Auger electrons, as well as all the positive ions. The outermost valence electrons move along with their parent atoms, unless condition (5.3) is fulfilled at any given time, in which case they are propagated independently.

Having outlined all the particularities of the implementation, all that remains is to select an appropriate system to be studied. To this end we make use of the protein database to obtain a the structure and composition of a representative molecule. The structure of a T4 Lysozyme Mutant (pdb entry 2LC9 [108]) was chosen, an enzyme consisting of 2629 atoms and containing hydrogen, carbon, nitrogen, oxygen and sulphur. Lysozymes are abundant in nature and across species in different forms, in tears, saliva, egg white, milk and some other secretions, so it is quite safe to say they are representative biomolecules. Beside this, there are no particular reasons to prefer this arbitrary structure above other forms of lysozyme, or even above other proteins.

We have already observed in the previous chapters that the resulting dynamics from multi-channel systems can quickly become very complicated, this is even more so true if the system is multi-component, or inhomogeneous, or does not possess a particularly simple geometry. All these complications are present in the 2LC9 system, and using only the results of our simulation would make it difficult to identify which particular features arise as a consequence of charge migration. In order to solve this problem we study this system in parallel with another simulation scheme that is in some way a slightly expanded version of the original one used by Neutze. *et. al*, where ionization takes place through photoionization, Auger decay, and Compton scattering. We do propagate both the Compton and Auger electrons along with the ions, but field ionization is not allowed. By comparing the results from these two simulation schemes, for different pulse lengths and intensities, we expect to clearly identify the influence and features that arise from charge migration.

### 5.3.1 Time Evolution

We consider pulse intensities ranging from  $1.6 \times 10^{21}$  to  $1.6 \times 10^{22}$  W/cm<sup>2</sup> and pulse lengths spanning from 1 to 20 fs, conditions similar to the ones used in [79] yet still experimentally challenging at the moment. Each condition is studied using a set of 50 realizations to provide meaningful statistics. As the pulse arrives to the sample and ionization takes place and the constituent atoms start to move in different ways, according to their mass, charge state, and the local electric field. For this reason it is useful to calculate the average displacement of the different atomic species  $k$  as the pulse develops, as follows

$$\langle \Delta R_k(t) \rangle = \frac{1}{N_k} \sum_i \| \mathbf{R}_{k,i}(t) - \mathbf{R}_{k,i}^0 \|, \quad (5.5)$$

where  $\mathbf{R}_{k,i}^0$  is the original position of the ion  $i$  before the pulse starts, while  $\mathbf{R}_{k,i}(t)$  is its corresponding position at time  $t$ , and  $N_k$  is the total number of atoms of the species  $k$  in the 2LC9 system.

This average displacement is shown in Fig. 5.4 for the lowest and highest intensities considered here and a pulse length of 15 fs, for hydrogen, carbon, nitrogen and oxygen. Due to the small amount of sulphur in the system (only 5 atoms), it will be studied in more detail in a following section and will not be discussed for the moment. It is clear that the inclusion of charge migration has a tremendous impact in the ionic dynamics and, quite interestingly, even if a considerably larger number of species is present, a strong segregation and emission is observed for the protons while all the other heavy ions show the opposite effect. For the case of hydrogen with the inclusion of charge migration, despite having no direct interaction with the laser pulse, it quickly escapes the system as it gets charged through field ionization. Without charge migration the Compton scattering is the only ionization channel available for hydrogen and only a small amount of protons are released, as evidenced by the considerably smaller average displacement at all times. Heavier atoms in contrast seem to stabilize when charge

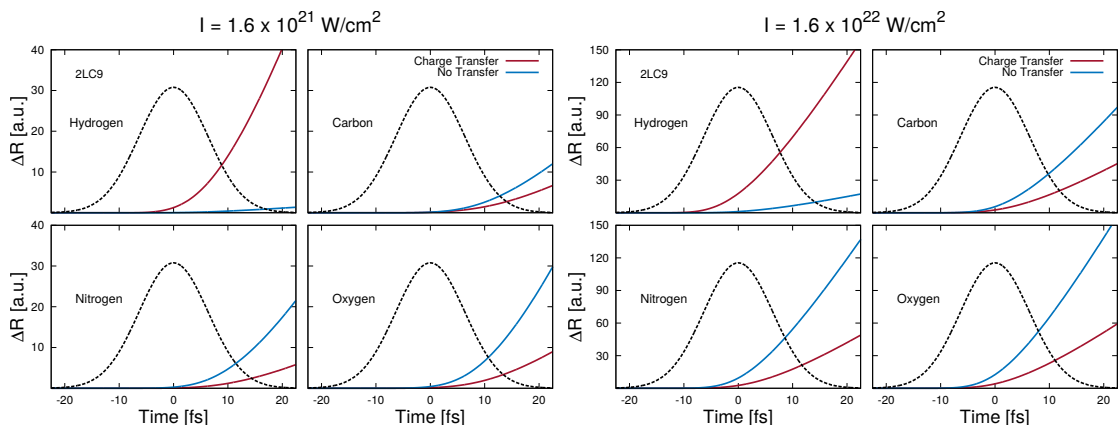


**Figure 5.4:** Comparison of the time evolution of the average displacement as obtained through simulations with charge migration (red) and without (blue) for the hydrogen, carbon, nitrogen and oxygen atoms in the 2LC9 system, for the lowest and highest intensities considered, and a pulse length of 15 fs. The pulse envelope is also included as a reference (dashed black line).

migration is included, showing a smaller average displacement even if the number of absorbed photons is roughly the same for both scenarios, as Compton scattering is not an efficient ionization channel due to its very small cross-section. It has to be concluded then that, just like it has been observed in hydride cluster [55] there is a net flow of electrons from the field ionized hydrogen ions to the heavier ones, which take away a large amount of the deposited energy as they leave the molecule. The remaining heavy ions are partially screened and, even if the system ultimately disintegrates, it does so in a significantly less violent way. Results for different intensities appear to show no qualitative difference. The only effect is a higher charging and consequently a faster explosion, while the overall trends are preserved.

This stabilization feature of heavy atoms is good news for the problem of structure determination, as those are precisely the main scatterers in diffractive imaging. The fast exploding protons pose no problem in this regard as their elastic scattering cross-section, just like all of its other interactions with light, are quite small by comparison and do not contribute significantly to the diffraction signal. In fact for regular experiments in synchrotron X-ray crystallography, the molecular structure is usually determined for all atoms except hydrogen. The latter have to be added *a posteriori* according to different assumptions and models [109,110]. Furthermore, as can be seen in Fig. 5.4, almost half of the pulse has already acted on the sample before any significant displacement is observed. This means that a good share of the structural information obtained by the diffraction pattern would be due to photons scattered from an undisturbed system. As scattering is a linear process, and assuming for the moment that the scattering cross-section and form factors remain stationary along the pulse, we can measure this structural information by proposing an integrated effective average displacement, as follows

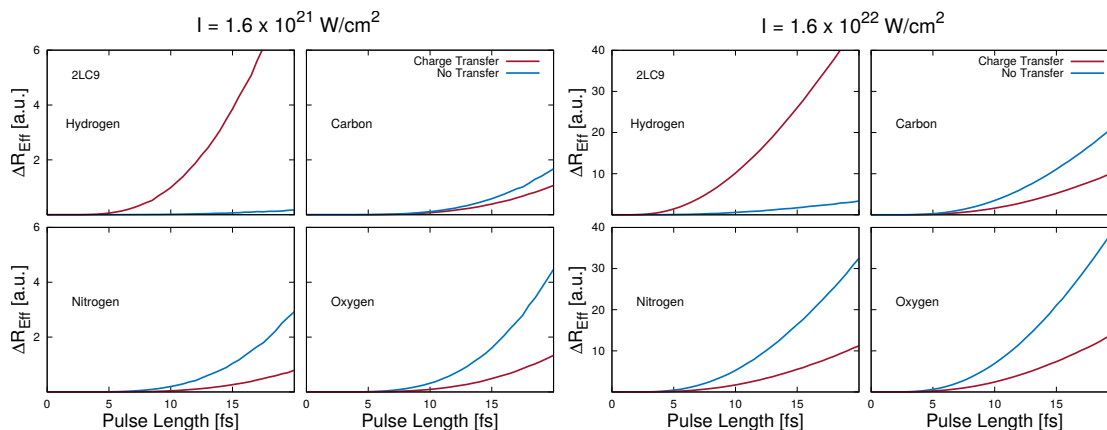


**Figure 5.5:** Effective average displacement (as defined by equation (5.6)) as a function of the pulse length, for simulations with charge migration (red) and without (blue) for the hydrogen, carbon, nitrogen and oxygen atoms in the 2LC9 system, for the lowest and highest intensities considered.

$$\langle \Delta R_k \rangle_{\text{Eff}} = \frac{1}{N_k} \sum_i \frac{\int dt I(t) \|\mathbf{R}_{k,i}(t) - \mathbf{R}_{k,i}^0\|}{\int dt I(t)}, \quad (5.6)$$

where the integration considers the complete pulse.

The effective displacement is shown in Fig. 5.5 with different pulse lengths, for the lowest and highest intensity. The trend observed previously is preserved and common to all pulse lengths and intensities, with hydrogen rapidly escaping and heavier ions remaining around their original positions. By this simple measure it can already be concluded that heavy atoms will only have sub-angstrom displacements for pulse lengths up to 5 fs, even at the highest intensities. This implies in principle that any diffraction data obtained under these experimental conditions would not suffer from radiation damage. This effect should be enhanced even further when the time-dependent scattering factors are taken into account, as the molecule scatters more effectively at the beginning of the pulse when all electrons can contribute. The eventual electrons loss due to the different ionization mechanisms diminishes the scattering power of the molecule, and might serve as an additional self-gating mechanism, in a way that parallels the effect of the loss of periodic order in SFX experiments [111].

## 5.4 Influence in XFEL Diffractive Imaging

The scattering signal measured in a hypothetical experiment would be the result of all the scattered photons over the entire pulse. During this time the flux of scattered photons in any given direction is constantly modified due to the electron loss and the ionic motion. In this section we calculate the diffraction patterns of the previous experiments taking into account the time-dependent ionic positions and form factors, as well as the

time dependent laser field. The total intensity of the diffraction signal  $S$  measured experimentally at any given point in the detector screen is therefore

$$S(\mathbf{k}) = \int_{\tau} dt |\mathbf{E}(\mathbf{k}, t)|^2, \quad (5.7)$$

where  $\mathbf{k}$  is the momentum transfer vector, and  $\mathbf{E}$  is the electric field at that point, which by neglecting polarization effects is given by

$$\mathbf{E}(\mathbf{k}, t) = \sum_{j=1}^{N_S} n_j(t) A_j(\mathbf{k}) e^{-i\mathbf{k} \cdot \mathbf{R}_j(t)},$$

with  $N_S$  being the number of shells in the molecule (for all atoms),  $n_j$  the number number of electrons in the shell  $j$ , while  $A_j$  is the corresponding form factor of said shell and  $\mathbf{R}_j(t)$  is the position at time  $t$  of the atom where the shell  $j$  belongs to.

The form factor  $A_j$  is related through equation (2.1) to the charge density  $\rho_j$  as follows

$$A_j(\mathbf{k}) = \int d^3r \rho_j(\mathbf{r}) e^{i\mathbf{k} \cdot \mathbf{r}}, \quad (5.8)$$

which by assuming a normalized charge density of the form

$$\rho_j = \frac{1}{8\pi r_j^3} e^{r/a_j}, \quad (5.9)$$

can be written as

$$A_j(\mathbf{k}) = \frac{1}{[1 + k^2 a_j^2]^2}, \quad (5.10)$$

with  $a_j$  being the mean radius of the charge density. Assuming that this proposed charge density can be obtained from a wave function such that  $\rho_j \sim |\psi_j|^2$ , which also happens to be an eigenfunction of the atomic system, then  $H\psi_j = E_j\psi_j$  for all  $r$ , and in particular for  $r \rightarrow \infty$  where we simply have

$$\frac{1}{2} \frac{d^2}{dr^2} \psi_j(r) = E_j \psi_j(r). \quad (5.11)$$

Therefore, the mean radius can be easily obtained as

$$a_j = \frac{1}{\sqrt{8|E_{b,j}|}}, \quad (5.12)$$

where  $E_{b,j}$  is the ionization energy of the shell  $j$ . While the actual ionization energy undoubtedly depends on the particular atomic species, we assume a simplified approach where we consider no significant differences arise among all the different valence shells, assigning a typical electron radius of  $a_j = 1/2$ , while for the core shells a value of  $a_j = 1/10$  is considered.

The calculated diffraction patterns are shown in Fig. 5.6 as constructed over a rectangular detection screen, perpendicular to the propagation of the laser beam and with a



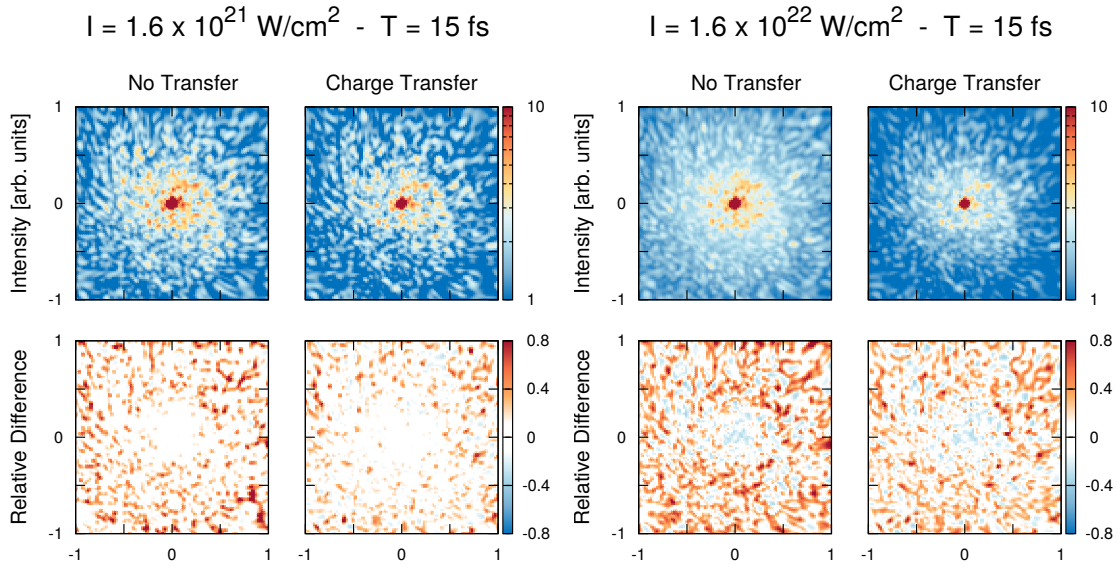


**Figure 5.6:** (Upper Section) Diffraction patterns obtained through the integrated scattering signal from both simulation schemes, for the lowest and highest intensities considered. (Lower Section) Relative difference of the diffraction patterns from numerical simulations with respect to an idealized case (refer to text).

total aperture of  $90^\circ$  in the  $x$  and  $y$  directions. The merged data from 50 different realizations is considered, for the highest and lowest intensity and a 15 fs pulse length in both simulation schemes. A first glance over these results might give very little insight about the underlying dynamics and its impact, due to their complexity. A direct comparison between both simulation schemes is also not a fair approach, as the occupation numbers of the ions could differ significantly. A more useful picture can be constructed by comparing each diffraction pattern with respect to the one that would be obtained from an unperturbed molecule ( $S_{\text{Ideal}}$ ), while the same time dependent occupation numbers are taken into consideration. In this way we obtain a differential pattern  $\Delta S$  where only the radiation damage due to the influence of the different ionic dynamics is taken into account, while the inevitable loss of scattering power is disregarded. These differential patterns, calculated as

$$\Delta S(\mathbf{k}) = \frac{S(\mathbf{k}) - S_{\text{Ideal}}(\mathbf{k})}{S_{\text{Ideal}}(\mathbf{k})} \quad (5.13)$$

are also shown in Fig. 5.6, for both simulation schemes.

A general feature, present in both simulation approaches, is an increase in the signal observed at wide scattering angles. With the inclusion of charge transfer mechanisms, however, these discrepancies are not only consistently smaller but also appear to be located at wider scattering angles. This has important consequences as wide angle scattering contains the most detailed information about the molecular structure. At high intensities in particular, even if damage is evident in both simulation schemes, the inclusion of charge transfer seems to preserve well defined features in the diffraction

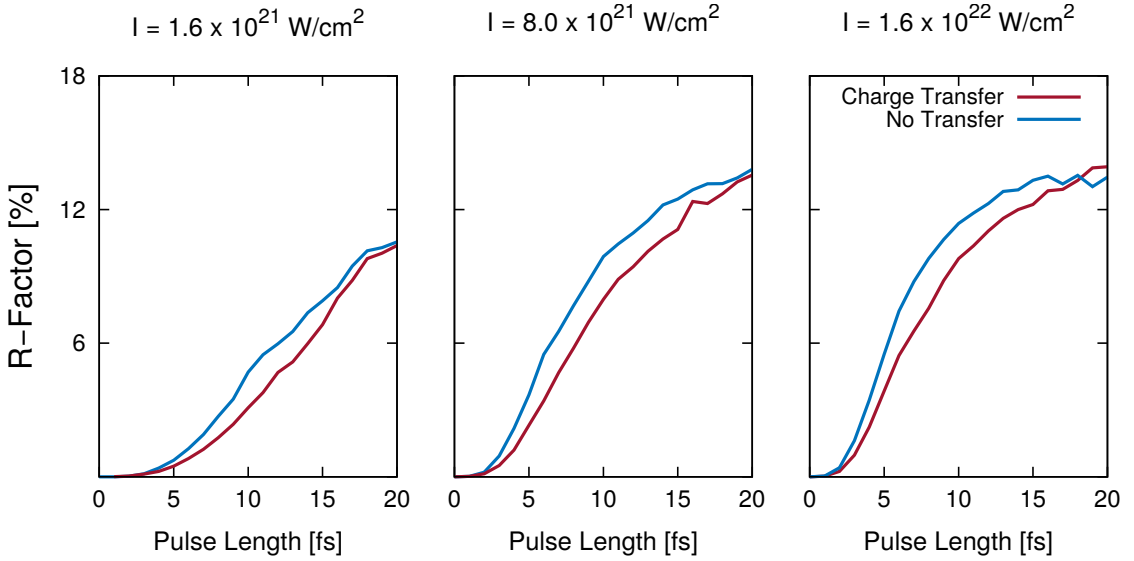


**Figure 5.7:** Comparison of the  $R$  factor from one-shot diffraction patterns, as obtained from numerical simulations with charge migration (red) and without (blue), as a function of the pulse length, for the different intensities considered.

pattern.

In order to assess the data quality in a quantitative way we make use of the so called  $R$  factor [112, 113] (sometimes called residual or reliability factor), defined here as follows:

$$R \equiv \sum_u \left| \frac{\sqrt{S(u)} - \sqrt{S_{\text{ideal}}(u)}}{\sum_{u'} \sqrt{S_{\text{ideal}}(u')}} \right|, \quad (5.14)$$

where  $S$  is the time integrated intensity from the evolving system,  $S_{\text{ideal}}$  the corresponding integrated intensity for the static unperturbed molecule, and the index  $u$  runs over all the pixels in the detection screen. Nevertheless, it has to be pointed out that even in usual X-ray crystallography there is no unique definition of a  $R$  factor and different formulations exist with varying degrees of sophistication [113–115]. The results obtained by this simple formulation should then be mainly understood as a coarse measure of the data quality, whose main purpose is to identify trends and possible features.

In Fig. 5.7 the calculated  $R$  factors are shown for a single shot measurement, where the somewhat noisy results clearly reflect the stochastic nature of the photoionization process. In each realization the laser pulse ionizes the constituent atoms in the molecule in a different way, creating each time a different time dependent charge distribution which drives the ionic motion accordingly. Despite the noise however, a consistent improvement in value of the  $R$  factor can be observed when charge migration is included, for almost all pulse lengths for the three different intensities considered. While single shot data is not directly used to obtain the molecular structure of the sample, a fundamental step in the whole process is the sorting of each individual data set, and the small improvement observed could have important consequences. Unfortunately at this point

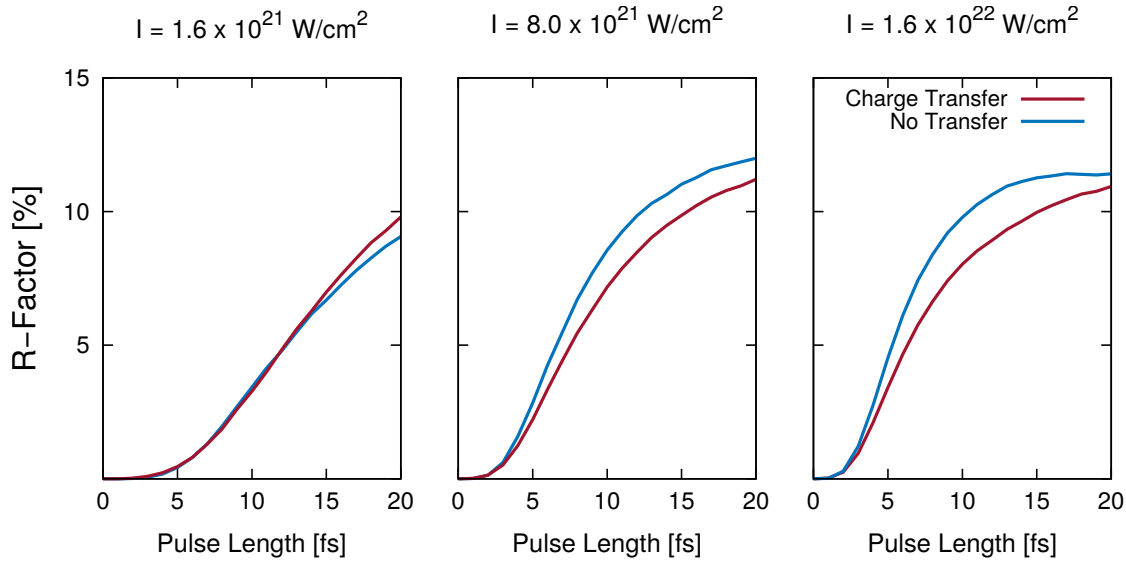


**Figure 5.8:** Comparison of the  $R$  factor from the diffraction patterns obtained by merging a set of 50 realizations, as obtained from numerical simulations with charge migration (red) and without (blue), as a function of the pulse length, for the different intensities considered.

it is not entirely clear how much of the observed improvement is due to the random nature of photoabsorption, and how much is due to a systematic enhancement of the data quality.

To answer this question the calculated  $R$  factors from a merged set of 50 realizations are shown in Fig. 5.8 from the diffraction images calculated according to (5.7) for different intensities and pulse lengths, comparing both simulation schemes. The  $R$  factors are consistently smaller for all pulse lengths, except for lowest intensity where there seems to be no appreciable difference. This points out that while charge migration might perhaps also improve the data quality for low intensities, this difference is hindered by the stochastic effects in charging, and finally averaged out by the data merging procedure. This is not the case for higher intensities, where the damping effects of charge migration clearly survive the averaging, implying that stabilization of heavy atoms seems to favorably impact in data quality.

It is also observed quite naturally that the use of longer pulses increases the value of the  $R$  factor, as ionic motion has more time to develop and to destroy the structure. Nevertheless, the smaller  $R$  factors obtained by the inclusion of charge migration effects imply that in principle, longer pulses than previously expected can be used to obtain useful data, in particular for higher intensities. While the difference does not seem very pronounced, it could have a significant impact as the achievement of both intense and short pulses is still nowadays experimentally challenging, particularly when the pulse length is less than 10 fs.

While a complete discussion over the full implications of charge migration would require further studies, the use of alternative approaches for the  $R$  factor (not shown)

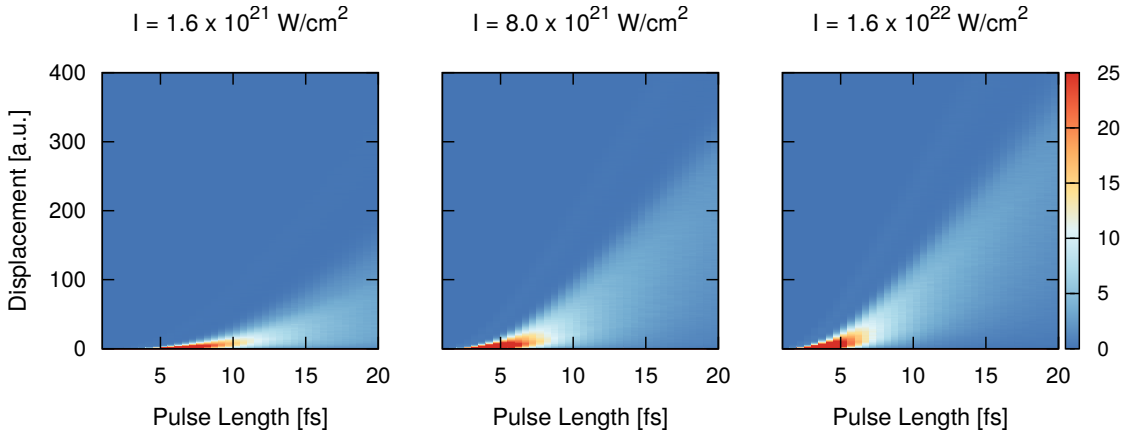


**Figure 5.9:** Displacement distribution as a function of the pulse length, as obtained from simulation where charge migration effects are not included, for the different intensities considered.

appears to agree with these observations, as the same trends are obtained. The same remains true for different molecular orientations we have analyzed and, while there might be some other factors such as the wavelength, the particle size, and so on, it seems safe to state that charge migration effects do improve data quality from diffraction experiments.

## 5.5 Ionic Motion and Coulomb Explosion

After having analyzed the average dynamics of the different constituent species in the 2LC9 system in the previous section, it is appropriate to study this dynamics in a more detailed way. To this end the displacement distributions are calculated for the positions towards the end of the gaussian pulse, at a distance of 1.5 times the FWHM from the pulse peak. By doing so we account for more than 99% of the total incoming photons.

The final position distribution for the case where charge migration is not allowed is shown in Fig. 5.9 for different intensities, as a function of the pulse length. Without charge migration the molecule Coulomb explodes apparently in a homogeneous way, and the structure does not survive more than some femtoseconds. Higher intensities induce a more violent explosion through a faster charging that destroys the system sooner, giving rise to a distribution that rapidly broadens.

With the inclusion of charge migration effects a big qualitative difference arises in the displacement distribution shown in Fig. 5.10. This distribution now displays two modes, one peak remaining close to zero displacement for all times while another one indicates a quick escape. The latter is formed solely by field ionized hydrogen, and a higher pulse intensity results in a faster explosion. The remaining heavy ions constitute the peak around zero, in an excited but essentially neutral state, which for the case of low intensities seems to be almost unchanged when using longer pulses. Eventually, the remaining ions undergo a much slower hydrodynamic expansion.

As the intensity increases the heavy ion peak indeed manages to remain around zero

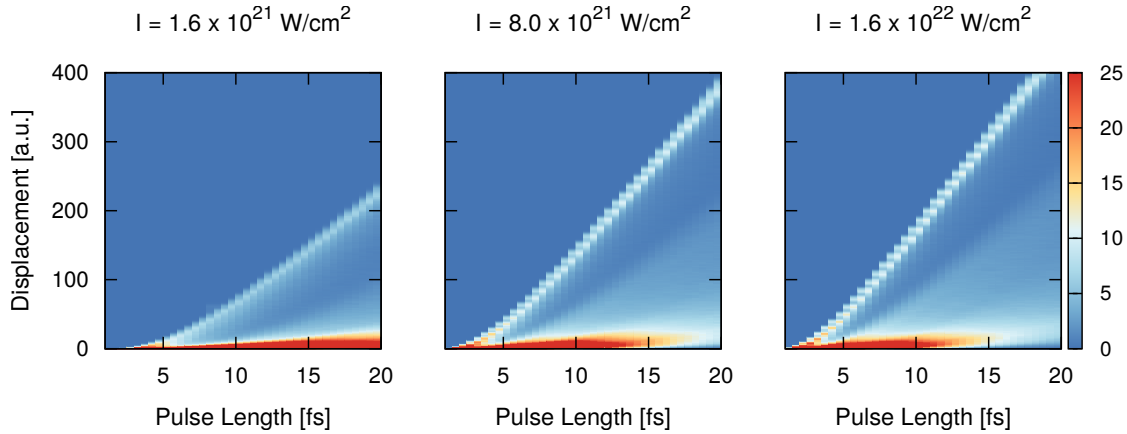


**Figure 5.10:** Displacement distribution as a function of the pulse length, as obtained from simulation with charge migration effects, for the different intensities considered.

for considerably longer times when compared to the homogeneous Coulomb explosion case, but eventually disintegrate for increasingly longer pulse lengths. This behavior can be explained by what was observed in [55] for hydride clusters, as for low intensities the fast exploding hydrogen manage to essentially neutralize the system, leaving only a low energetic expansion. As the amount of energy that can be removed by proton ejection is limited, at higher intensities the system can only be stabilized through this mechanism for the early stages of the pulse, and further damage has to be sustained directly by the remaining heavier ions, ultimately leading to a significantly damped but similar Coulomb explosion.

These features are even more evident in Fig. 5.11, where the relative increase in the magnitude of the radial coordinate  $|r_f|/|r_i|$  is shown for different elements at the end of a 20 fs pulse. Here we can clearly observe that without charge migration, all the heavy atoms undergo an expansion with very similar distributions. These distributions are very broad, except for a peak located at  $|r_f|/|r_i| = 1$ , corresponding to a small fraction of ions that have not absorbed any photons. This clearly unphysical peak naturally disappears for high intensities where no neutral ion remains, for all elements except hydrogen due to its small cross-section. In contrast, the inclusion of charge transfer mechanisms produces narrow distributions for heavy with peaks located close to  $|r_f|/|r_i| = 1$ , and a very broad distribution for the case of hydrogen. Interestingly enough, a small fraction of the ions even get closer to the center of mass of the molecule ( $|r_f|/|r_i| < 1$ ). The transition from a hydrodynamic expansion into a Coulomb explosion can also be observed as the distributions of heavy ions evolve from monomodal at low intensities, into bimodal ones for high intensities.

There is additionally another interesting feature, as without charge migration the distributions a somewhat chaotic and homogeneous explosion takes place. On the other hand, with the inclusion of charge transfer mechanisms, the distributions appear to have richer and more complicated structures, particularly evident in the case of hydrogen.

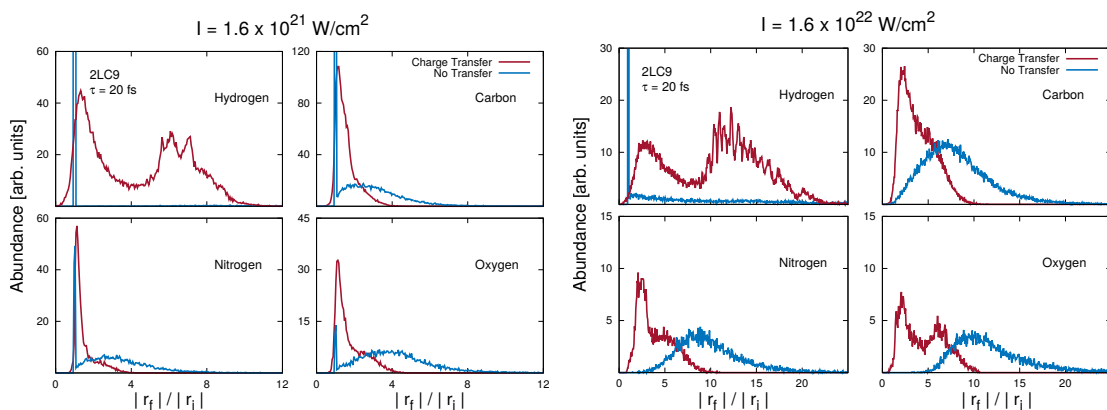


**Figure 5.11:** Histograms of the relative change of the radial coordinate  $|r_f|/|r_i|$  for simulations with charge migration (red) and without (blue) for the hydrogen, carbon, nitrogen and oxygen atoms in the 2LC9 system, for the lowest and highest intensities considered, with a 20 fs pulse.

This seems to imply that the ions might preserve information about the structure of the molecule as they evolve in time.

From all the previous result we can conclude that proteins particularly rich in hydrogen would be able to withstand higher amounts of damage while maintaining its structure for longer periods of time, as a higher charge could be neutralized by proton ejection. It is also often the case for proteins to be surrounded by a solvation layer, which might not only imply a different structure in comparison to nanocrystals but also would provide for an extra number of protons, perhaps helping to further stabilize the molecule.

### 5.5.1 Deterministic trajectories in sulphur

So far the study of the dynamics of the five sulphur ions in the 2LC9 molecule has been relegated by favoring the other more abundant elements. This has given us a good idea of the general features of the dynamics. It has been observed that without charge migration effects, the molecule as a whole explodes very homogeneously. However, with the inclusion of charge transfer mechanisms the time evolution of the system appears to carry some structural information, and in order to study the particularities of these dynamics it might be useful to focus on a small subset of particles, for which the sulphur ions seem to be an appropriate choice. At this point we will focus exclusively on the dynamics of sulphur for long pulses, allowing enough time for the system to evolve.

Some of the individual trajectories calculated for each of the five sulphur atoms are shown in Fig. 5.12, along with the initial configuration of the 2LC9 system for the lowest and highest intensities investigated, both for a pulse length of 20 fs. Also shown is the temporal evolution of the radial coordinate for each sulphur atom. The expected increase in time of the radial coordinate as the molecule disintegrates is clear, but some interesting behavior is now evident. The first and most remarkable characteristic is that for each of the individual sulphur atoms many different realizations produce very similar

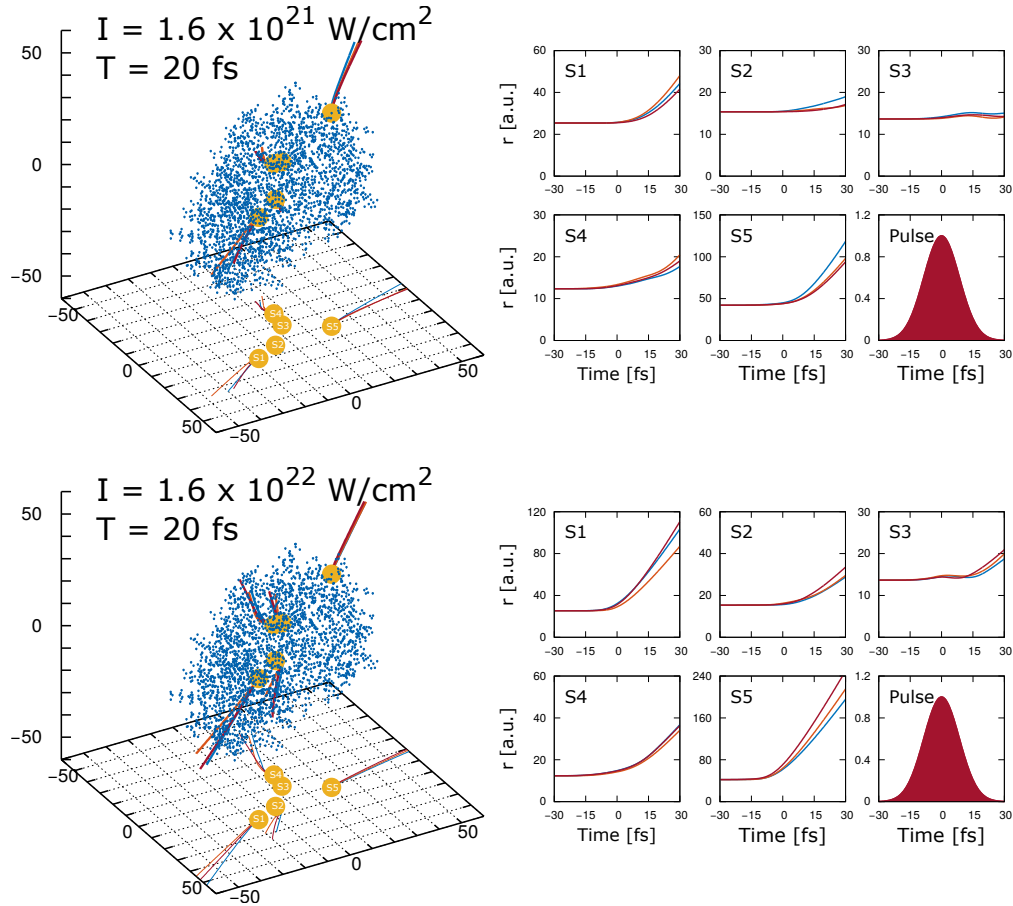


**Figure 5.12:** (Left) Individual trajectories of each sulphur atom in the 2LC9 system for three different realizations, for the lowest and highest intensities considered and a 20 fs pulse length. (Right) Radial coordinate as a function of time for each of the individual sulphur atom for the corresponding realizations.

trajectories, even if this trajectories are not particularly simple and despite the random nature of the photoionization process. While expansion seems to be a general trend for all sulphur atoms, this expansion differs significantly for each one of them.

The atom S5 located the farthest from the center of mass, is the fastest moving one in both scenarios. This can be explained by the fact that the electric field is strongest close to the surface, so that atoms far from the center are accelerated most strongly. This argument also explains why the atom S1 is the second fastest for both intensities, as its initial radial coordinate is correspondingly the second largest. This simple explanation, however, cannot account for the remaining sulphur ions which, despite their similar initial distances with respect to the center of mass, display quantitative and sometimes even qualitative different behavior. These three atoms do not show a clear trend in their radial evolution, as the atom S4 which is closest to the center seems to move faster, atom S2 appears to move slightly slower, and finally atom S3 is essentially indifferent

to the dynamics. These differences might be explained by the fact that different atoms have different environments and neighbors, from which they could be more or less likely to get electrons, reducing with this their effective charge. This suggests that while the locations of the ions can have an important influence on their trajectories (as occurs for atom S5), the local environment might be equally important and can give rise to significant differences.

The deterministic trajectories of these heavy atoms on the other hand might be of great help in the realization of single-particle imaging. After all, the signal requirement in a single shot experiment is not to obtain a sufficiently high signal-to-noise ratio to perform the analysis, it suffices with a strong enough signal to determine the target orientation and classify the different performed measurements. Once the data is classified and processed, the determination of the structure can be done. In this respect, by detecting these heavy ions the molecular orientation could be determined within a small margin of error, which might depend both on the target and the pulse characteristics. This idea has been proposed before [116] and simulated without charge migration mechanisms, where it was concluded that the usually encountered inhomogeneities in the sample would induce great deviations in the final trajectories. We have observed here, that inhomogeneities in fact propitiate similar trajectories for each ion.

### 5.5.2 Conclusions

The problem of single-particle diffractive imaging with XFEL pulses has been analyzed for the case of lysozyme 2LC9, and in particular the effect that charge migration has both in the dynamics and in the diffraction pattern. These effect have been usually overlooked in similar studies and, from what has been observed both theoretically and experimentally in hydride clusters, the influence on the dynamics can be tremendous. It was observed that charge migration also enables proton emission in more complex molecules, even when many more atomic species are present. Through this mechanism the system loses a great amount of energy in a very short time compared to the ionic motion. This process allows for the remaining atoms to stay closer to their original position for longer times, as the molecule disintegrates in a less violent manner.

The effect of proton emission is also observed in the diffraction pattern, allowing longer pulse lengths to be used compared to previous results, while maintaining the same resolution. Furthermore, the previously reported problems that arise when inhomogeneous samples are used also are reduced through this mechanism, which might allow for the determination of the molecular orientation by detecting the heavy atoms.

Charge migration effects might also be partially responsible for the current success of serial femtosecond crystallography, where radiation damage appears to be less problematic than previously expected. As the XFEL beam only partially illuminates the sample, the surrounding unit cells might act as a huge source of electrons that can continuously screen the heavy ions and perhaps preventing the loss of their scattering power.



## Chapter 6

# Summary and Outlook

In this thesis we aimed to gain a better understanding of some of the complex dynamics that arise in finite systems exposed to the highly intense pulses provided by XFELs. Of course, due to the multitude of atom-photon interactions that occur in the X-ray regime, as well as the many different systems that can be studied in XFEL experiments, we had to restrict ourselves to a limited number of representative and general systems. Nevertheless, it was clear from our very first results that this regime holds many surprises even in the simplest scenarios we considered. This trend was observed at every new step we took, and with each new result many more questions and some very interesting possibilities have appeared, which we briefly summarize here.

### 6.1 Multiple Ionization

We began our efforts by studying the problem of multiple sequential ionization in clusters under XFEL pulses. This subject has been previously addressed in earlier XFEL experiments, and the resulting plateau in the electron energy spectrum from the direct emission of photoelectrons has been already measured and explained. Equally well understood is the thermalization and evaporation of plasma electrons obtained from inner ionization, giving rise to the emission of fast electrons. These plasma electrons appear as an exponentially decaying distribution in the energy spectra.

However, a new feature arises at the transition between these two well defined regimes, when both direct photoelectrons and plasma electrons can be created by the incoming photons. Charge screening due to the trapped plasma electrons allows for more direct photoelectrons to escape the system, producing a peak at low energies in the electron energy spectra. Screening is the fundamental piece for the formation of this low-energy peak and, therefore, evaporation of plasma electrons can significantly suppress this feature. Moreover, this low-energy peak has to coexist with the plasma electron contribution in a similar energy region of the spectrum, which probably had prevented an earlier identification of this effect. Therefore, in order to facilitate the formation of the low-energy peak, experimental conditions have to be chosen in such a way that the plasma evaporation rate is as small as possible. We have found that this is

avored by the use either big clusters or low excess energies. Knowing this might allow to experimentally disentangle both contributions in the spectrum, in future studies.

This simple phenomenon poses new questions, as how it would translate to heterogeneous, multi-component systems. For example, by having two components with different binding energies we could in principle observe similar effects at more convenient energy intervals, where plasma electrons have no influence. Interesting differences may also arise if the cluster is homogeneous mixture or in a core-shell configuration.

The competition between plasma evaporation and the sequential low energy peak could also be exploited in our favor. If the low energy peak is disentangled, it might serve as a probe for the time evolution of the plasma in very short time scales.

## 6.2 Multiple Channel Ionization

In our next study we tackled the problem of multiple channel ionization of fullerenes, as evidenced by the electron energy spectra. Fullerenes can be ionized through two main processes, namely photoionization and Auger decay. For intense XFEL pulses ionization can occur multiple times until the constituent carbon atoms are eventually stripped from all their electrons, and the resulting energy spectra can be very complicated and hard to interpret. A progressive approach was taken, where we started by a simplified scenario and, step by step, more complication were added until finally a realistic case was analyzed. At the end of this series of studies, and with the insight gained in all these steps, a surprisingly clear interpretation of the electron energy spectra was obtained.

As a first step we considered a homogeneous sphere of constant radius where only two consecutive ionization channels are available. Even for this simple case the spectra showed many different shapes, whose features are uniquely defined by the ratio of the rates of the consecutive channels. Some interesting cases arise for the limit where the photoabsorption rate  $\Gamma$  is much larger than the Auger decay rate  $\lambda$ , or viceversa, where the electron energy spectra features one plateau for each contribution. Additionally, for the very particular case where  $\Gamma/\lambda = 2$ , each contribution shows a triangular shape which mirror each other.

As a next step of sophistication we considered the ionization dynamics of fullerene  $C_{60}$  with fixed positions for the ions. For this case, in addition to the previous observations, two new features emerge. The first one is due to screening, which occurs when the background charge is so high that the least energetic electrons can no longer leave the system. This is observed as a sudden step in the spectra at a characteristic energy. The second feature occurs at high intensities, where the formation of double core-holes is greatly favored, showing the characteristic triangular shape for  $\Gamma/\lambda = 2$ , which holds precisely for the creation of single and double core-hole states.

Finally the full problem of fullerene  $C_{60}$  with ionic motion was tackled in two scenarios: constant pulse length and constant peak intensity. For short pulses, the spectrum evolves from sharp, atomic-like spectra, to a broad spectrum similar to the previous high-intensity results. Ionic motion does not seem to affect the photoelectron contribution, however, intense enough pulses produce a new high energy peak for the Auger

electrons, corresponding to long lived excited states that decay after the molecule has disintegrated.

For the case of constant intensity, the spectra evolved from short pulses where no new features due to ionic motion are observed, while progressively longer pulses induce broader photoelectron spectra. For pulses longer than 6 fs the broadening stagnates and an accumulation of photoelectrons at the lower end of the spectrum appears. Finally, for pulses longer than 10 fs, the trend is reversed and the photoelectron spectrum starts to narrow. This phenomenon is understood from the competition of charging and expansion, affecting the potential and in consequence the electrons final energy. For short pulses the potential is influenced mainly by charging, while for long pulses expansion takes over.

A simple feature connecting the number of emitted photoelectrons to the Auger decay rate could be identified. For intense XFEL pulses, Auger decay acts as a gate that allows or blocks further ionization. As the number of photoelectrons is a very robust observable, it could then be used to measure or estimate the Auger decay rate in molecules, which is both hard to calculate from first principles and not easily accessible by usual experiments.

This opens new research possibilities, not only as a new way to measure molecular Auger rates but perhaps some other intriguing decay mechanisms like Interatomic Coulomb Decay (ICD) or Electron Transfer Mediated Decay (ETMD), whose dependence with respect to the interatomic distances might also give rise to new surprising phenomena.

### 6.3 Charge Migration

In our final study we sought to understand the effects of charge migration in complex biological molecules, and in particular its impact on single-particle diffraction imaging applications. For this we have chosen an arbitrary but representative system in the form of the 2LC9 molecule, a lysozyme mutant containing all the mayor atomic species present in biological systems. From the very beginning we observed that the inclusion of charge migration greatly influences the dynamics in the system, changing them even in a qualitative way. Proton ejection, a mechanism previously observed in hydride clusters, is also present in the 2LC9 molecule, despite being a considerably more inhomogeneous and asymmetric system. And also in the same manner, proton ejection is an efficient mechanism to release energy deposited from the laser into the system. A side effect of this energy release is that the expansion of the remaining ions is considerably suppressed, remaining close to their original positions for longer periods of time. Radiation damage in a single particle has two components, ionization damage from photoabsorption and structural damage from ionic motion. In this way the suppressed expansion can be understood as a partial mitigation of radiation damage, due to proton ejection.

This is further confirmed through the calculation of the diffraction patterns corresponding to different intensities and pulse lengths, as well as their  $R$  factors. Both these results suggest that charge migration effects allow for the use of longer pulses in diffrac-

tion experiments, without significant loss of structural information. Therefore, it was found that usually encountered inhomogeneities in biological systems, usually considered a matter of concern for single particle diffraction experiments, have a mitigating effect that preserves structural information and might as well explain the lack of measurable radiation damage in recent SFX experiments.

There are, of course, many open questions and research opportunities in this topic, such as how charge migration affects nanocrystals and what role does periodicity play. It can be inferred from the present results that in nanocrystals, the availability of more electrons from the neighboring unit cells can further stabilize the sample in serial femtosecond X-ray crystallography (SFX) experiments, as the radiation damage can effectively be pushed away from the beam focus into the surrounding crystal structure.

Also, data quality might be improved further through electron recombination by allowing the sample to regain some of its scattering power, in particular for heavier ions. Further studies about the improvement of data quality are also needed, as not all the positions in the screen are equally useful for the determination of the molecular structure. A detailed study of the dependence of the  $R$  factor with respect to the scattering angle, the intensity, and photon energy, could help to determine optimal experimental conditions for single-particle imaging.

Finally, further investigation of how the apparently deterministic trajectories of heavy ions can be used to determine the molecular orientation. Understanding and exploiting all the previous phenomena might help to further relax the still demanding experimental requirements that single-molecule imaging seem to require.

# List of Figures

2.1	Relative contributions of Rayleigh scattering, Compton scattering, and photoionization cross-sections . . . . .	11
2.2	Fluorescence and Auger yields as a function of the atomic number $Z$ . . .	13
3.1	Sketch of the different regions and quantities influencing the total sequential ionization spectrum of a spherical cluster. . . . .	24
3.2	Collection of $P_q$ contributions from direct photoelectrons as well as the screened ones . . . . .	25
3.3	Analytical approximation of the sequential spectrum, compared to the numerically obtained one . . . . .	26
3.4	Full electron energy spectra and direct photoelectron contribution for a Coulomb complex of radius $R = 10$ , excess energy $\mathcal{E} = 40$ and $N = 1000$ .	29
3.5	Numerical electron energy spectra of direct photoelectrons for different pulse lengths. . . . .	30
3.6	Sketch of the different regions and quantities that define the number of electrons involved in the sequential ionization process . . . . .	31
3.7	Contribution of direct electrons and screened direct electrons in the sequential ionization spectrum . . . . .	32
3.8	Number of photoelectrons and plasma electrons with respect to the final charge $Q$ . . . . .	35
3.9	Numerical electron energy spectra for spherical clusters of different sizes .	36
3.10	Contour plot of the plasma electron density as a function of the cluster radius $R$ . . . . .	37
4.1	Sketch of the formation of a broad electron energy spectra in polyatomic molecules. . . . .	40
4.2	Spectrum obtained from rate equations for the case $\Gamma = \lambda$ . . . . .	44
4.3	Electron energy spectrum numerically obtained in the fast photoionization limit for a ratio $\Gamma/\lambda = 10^3$ . . . . .	45
4.4	Electron energy spectrum for the fast autoionization regime numerically obtained with a rate $\Gamma/\lambda = 10^{-3}$ . . . . .	47
4.5	Energy spectra of Auger and photoelectrons for the ratio $\Gamma/\lambda = 2$ for a rectangular and a Gaussian pulse . . . . .	49

4.6	Simplified scheme of the ionization path of carbon atoms in fullerene . . .	54
4.7	Electron energy spectrum calculated by molecular dynamics with fixed ions for a ratio $\Gamma/\lambda = 100$ . . . . .	56
4.8	Electron energy spectrum calculated by molecular dynamics with fixed ions for a ratio $\Gamma/\lambda = 0.01$ . . . . .	58
4.9	Electron energy spectrum obtained by molecular dynamics with fixed ions for equal rates $\Gamma = \lambda$ . . . . .	59
4.10	Electron energy spectra of the fullerene $C_{60}$ obtained by molecular dynamics for a pulse length $T = 1$ fs as a function of the intensity . . . . .	61
4.11	Electron energy spectra of the fullerene $C_{60}$ obtained by molecular dynamics for a constant peak intensity $I = 10^{19}$ W/cm <sup>2</sup> . . . . .	62
4.12	Time-dependent background potential $V(t)$ , and comparison with respect to the pulse envelope . . . . .	63
4.13	Comparison of two spectra with the same ratio $\Gamma/\lambda$ , for different Auger rates . . . . .	65
4.14	Number of photoelectrons obtained from microscopic MD calculations as a function of the pulse intensity, and as a function of the ratio $\Gamma/\lambda$ . . . . .	66
4.15	Number of photoelectrons according to the “bottle-neck model” . . . . .	69
4.16	Number of photoelectrons from microscopic MD calculations for fullerene at several photon fluxes and Auger rates . . . . .	70
5.1	Coulomb explosion of T4 lysozyme as determined by [79] . . . . .	76
5.2	Time evolution of a molecular $CH_4$ cluster and an atomic carbon cluster .	77
5.3	Comparison between the usual Coulomb potential for a single charged ion with respect to the potential defined by equation (5.1) . . . . .	79
5.4	Comparison of the time evolution of the average displacement for the hydrogen, carbon, nitrogen and oxygen atoms in 2LC9, with and without charge transfer mechanisms . . . . .	82
5.5	Effective average displacement as a function of the pulse length for hydrogen, carbon, nitrogen and oxygen atoms in 2LC9, with and without charge transfer mechanisms . . . . .	83
5.6	Diffraction patterns obtained through the integrated scattering signal and relative difference with an ideal case . . . . .	85
5.7	Comparison of the $R$ factor from one-shot diffraction patterns . . . . .	86
5.8	Comparison of the $R$ factor from the merged diffraction patterns of 50 realizations . . . . .	87
5.9	Displacement distribution as a function of the pulse length for simulations without charge migration mechanisms . . . . .	88
5.10	Displacement distribution as a function of the pulse length from simulations with charge transfer mechanisms . . . . .	89
5.11	Histograms of the relative change of the radial coordinate $ r_f / r_i $ . . . . .	90
5.12	Individual trajectories of each sulphur atom in the 2LC9 system . . . . .	91

# Bibliography

- [1] Ayvazyan, V. *et al.* First operation of a free-electron laser generating GW power radiation at 32 nm wavelength. *The European Physical Journal D-Atomic, Molecular, Optical and Plasma Physics* **37**, 297–303 (2006).
- [2] Ackermann, W. *et al.* Operation of a free-electron laser from the extreme ultraviolet to the water window. *Nature photonics* **1**, 336–342 (2007).
- [3] Emma, P. *et al.* First lasing and operation of an ångstrom-wavelength free-electron laser. *Nature Photonics* **4**, 641–647 (2010).
- [4] Shintake, T. *et al.* A compact free-electron laser for generating coherent radiation in the extreme ultraviolet region. *Nature Photonics* **2**, 555–559 (2008).
- [5] Ishikawa, T. *et al.* A compact X-ray free-electron laser emitting in the sub-ångstrom region. *Nature Photonics* **6**, 540–544 (2012).
- [6] Allaria, E. *et al.* Highly coherent and stable pulses from the FERMI seeded free-electron laser in the extreme ultraviolet. *Nature Photonics* **6**, 699–704 (2012).
- [7] Geloni, G. *et al.* Coherence properties of the european XFEL. *New Journal of Physics* **12**, 035021 (2010).
- [8] Patterson, B. *et al.* Coherent science at the swissFEL X-ray laser. *New Journal of Physics* **12**, 035012 (2010).
- [9] Sorokin, A. *et al.* Photoelectric effect at ultrahigh intensities. *Physical review letters* **99**, 213002 (2007).
- [10] Wabnitz, H. *et al.* Multiple ionization of atom clusters by intense soft X-rays from a free-electron laser. *Nature* **420**, 482–485 (2002).
- [11] van der Schot, G. *et al.* Imaging single cells in a beam of live cyanobacteria with an X-ray laser. *Nature communications* **6** (2015).
- [12] Hantke, M. F. *et al.* High-throughput imaging of heterogeneous cell organelles with an X-ray laser. *Nature photonics* (2014).

- [13] Seibert, M. M. *et al.* Single mimivirus particles intercepted and imaged with an X-ray laser. *Nature* **470**, 78–81 (2011).
- [14] Kern, J. *et al.* Simultaneous femtosecond X-ray spectroscopy and diffraction of photosystem II at room temperature. *Science* **340**, 491–495 (2013).
- [15] Kern, J. *et al.* Taking snapshots of photosynthetic water oxidation using femtosecond X-ray diffraction and spectroscopy. *Nature communications* **5** (2014).
- [16] Tenboer, J. *et al.* Time-resolved serial crystallography captures high-resolution intermediates of photoactive yellow protein. *Science* **346**, 1242–1246 (2014).
- [17] Redecke, L. *et al.* Natively inhibited trypanosoma brucei cathepsin b structure determined by using an X-ray laser. *Science* **339**, 227–230 (2013).
- [18] Pellegrini, C. The history of X-ray free-electron lasers. *The European Physical Journal H* **37**, 659–708 (2012).
- [19] Als-Nielsen, J. & McMorrow, D. *Elements of modern X-ray physics* (John Wiley & Sons, 2011).
- [20] Kirian, R. A. & Chapman, H. N. Imaging of objects by coherent diffraction of X-ray FEL pulses (2015).
- [21] Drake, G. W. *Springer handbook of atomic, molecular, and optical physics* (Springer Science & Business Media, 2006).
- [22] Hopersky, A. N., Nadolinsky, A. M. & Novikov, S. A. Compton scattering of two X-ray photons by an atom. *Physical Review A* **92**, 052709 (2015).
- [23] Fuchs, M. *et al.* Nonlinear X-ray Compton scattering. *arXiv preprint arXiv:1502.00704* (2015).
- [24] Pabst, S. Atomic and molecular dynamics triggered by ultrashort light pulses on the atto- to picosecond time scale. *The European Physical Journal Special Topics* **221**, 1–71 (2013).
- [25] Santra, R. & Young, L. Interaction of intense X-ray beams with atoms. In Jaeschke, E., Khan, S., Schneider, J. R. & Hastings, J. B. (eds.) *Synchrotron Light Sources and Free-Electron Lasers*, 1–24 (Springer International Publishing, 2015).
- [26] Moshhammer, R. *et al.* Few-photon multiple ionization of Ne and Ar by strong free-electron-laser pulses. *Physical review letters* **98**, 203001 (2007).
- [27] Hoener, M. *et al.* Ultra-intense X-ray induced ionization, dissociation, and frustrated absorption in molecular nitrogen. *Physical review letters* **104**, 253002 (2010).



- [28] Young, L. *et al.* Femtosecond electronic response of atoms to ultra-intense X-rays. *Nature* **466**, 56–61 (2010).
- [29] Mobilio, S., Boscherini, F. & Meneghini, C. *Synchrotron Radiation: Basics, Methods and Applications* (Springer, 2014).
- [30] Fang, L. *et al.* Double core-hole production in N<sub>2</sub>: beating the Auger clock. *Physical review letters* **105**, 083005 (2010).
- [31] Eland, J. H. *et al.* Double core hole creation and subsequent Auger decay in NH<sub>3</sub> and CH<sub>4</sub> molecules. *Physical review letters* **105**, 213005 (2010).
- [32] Bambynek, W. *et al.* X-ray fluorescence yields, Auger, and Coster-Kronig transition probabilities. *Reviews of Modern Physics* **44**, 716 (1972).
- [33] Attwood, D. *Soft X-rays and extreme ultraviolet radiation: principles and applications* (Cambridge university press, 1999).
- [34] Ditmire, T., Donnelly, T., Rubenchik, A., Falcone, R. & Perry, M. Interaction of intense laser pulses with atomic clusters. *Physical Review A* **53**, 3379 (1996).
- [35] Saalman, U., Siedschlag, C. & Rost, J. Mechanisms of cluster ionization in strong laser pulses. *Journal of Physics B: Atomic, Molecular and Optical Physics* **39**, R39 (2006).
- [36] Fennel, T. *et al.* Laser-driven nonlinear cluster dynamics. *Reviews of modern physics* **82**, 1793 (2010).
- [37] Milchberg, H., McNaught, S. & Parra, E. Plasma hydrodynamics of the intense laser-cluster interaction. *Physical Review E* **64**, 056402 (2001).
- [38] Gets, A. & Krainov, V. The ionization potentials of atomic ions in laser-irradiated Ar, Kr and Xe clusters. *Journal of Physics B: Atomic, Molecular and Optical Physics* **39**, 1787 (2006).
- [39] Hilse, P., Moll, M., Schlages, M. & Bornath, T. Laser-cluster-interaction in a nanoplasma-model with inclusion of lowered ionization energies. *Laser physics* **19**, 428–436 (2009).
- [40] Son, S.-K., Young, L., Santra, R. *et al.* Impact of hollow-atom formation on coherent X-ray scattering at high intensity. *Physical Review A* **83**, 033402 (2011).
- [41] Son, S.-K., Santra, R. *et al.* Monte Carlo calculation of ion, electron, and photon spectra of xenon atoms in X-ray free-electron laser pulses. *Physical Review A* **85**, 063415 (2012).
- [42] Murphy, B. *et al.* Femtosecond X-ray-induced explosion of C<sub>60</sub> at extreme intensity. *Nature communications* **5** (2014).

- [43] Hairer, E., Lubich, C. & Wanner, G. Geometric numerical integration illustrated by the Störmer–Verlet method. *Acta numerica* **12**, 399–450 (2003).
- [44] Last, I. & Jortner, J. Dynamics of the coulomb explosion of large clusters in a strong laser field. *Physical Review A* **62**, 013201 (2000).
- [45] Ditmire, T. Simulation of exploding clusters ionized by high-intensity femtosecond laser pulses. *Physical Review A* **57**, R4094 (1998).
- [46] Siedschlag, C. & Rost, J.-M. Small rare-gas clusters in soft X-ray pulses. *Physical review letters* **93**, 043402 (2004).
- [47] Rost, J.-M. Complex non-equilibrium dynamics in plasmas. *European Review* **17**, 249–262 (2009).
- [48] Bostedt, C. *et al.* Multistep ionization of argon clusters in intense femtosecond extreme ultraviolet pulses. *Physical Review Letters* **100**, 133401 (2008).
- [49] Bostedt, C. *et al.* Fast electrons from multi-electron dynamics in xenon clusters induced by inner-shell ionization. *New Journal of Physics* **12**, 083004 (2010).
- [50] Gnodtke, C., Saalman, U. & Rost, J.-M. Slow and fast multi-photon ionization of clusters in strong XUV and X-ray pulses. *Chem. Phys.* **414**, 65 (2013).
- [51] Iwayama, H. *et al.* Frustration of direct photoionization of ar clusters in intense extreme ultraviolet pulses from a free electron laser. *Journal of Physics B: Atomic, Molecular and Optical Physics* **42**, 134019 (2009).
- [52] Iwayama, H. *et al.* Frustration of direct photoionizations of rare gas clusters in intense extreme ultraviolet free-electron laser pulses. In *Journal of Physics: Conference Series*, vol. 212, 012014 (IOP Publishing, 2010).
- [53] Iwayama, H. *et al.* Frustration of photoionization of ar nanoplasma produced by extreme ultraviolet FEL pulses. *Journal of Physics B: Atomic, Molecular and Optical Physics* **46**, 164019 (2013).
- [54] Gnodtke, C., Saalman, U. & Rost, J.-M. Dynamics of photo-activated coulomb complexes. *New Journal of Physics* **13**, 013028 (2011).
- [55] Di Cintio, P., Saalman, U. & Rost, J.-M. Proton ejection from molecular hydride clusters exposed to strong X-ray pulses. *Physical review letters* **111**, 123401 (2013).
- [56] Gnodtke, C., Saalman, U. & Rost, J.-M. Massively parallel ionization of extended atomic systems. *Physical review letters* **108**, 175003 (2012).
- [57] Berrah, N. *et al.* Double-core-hole spectroscopy for chemical analysis with an intense X-ray femtosecond laser. *Proceedings of the National Academy of Sciences* **108**, 16912–16915 (2011).

- [58] Kroto, H. W. *et al.* C<sub>60</sub>: buckminsterfullerene. *Nature* **318**, 162–163 (1985).
- [59] O’Brien, S. C., Heath, J. R., Curl, R. F. & Smalley, R. E. Photophysics of buckminsterfullerene and other carbon cluster ions. *The Journal of Chemical Physics* **88**, 220–230 (1988).
- [60] Lépine, F. Multiscale dynamics of C<sub>60</sub> from attosecond to statistical physics. *Journal of Physics B: Atomic, Molecular and Optical Physics* **48**, 122002 (2015).
- [61] Rost, J.-M. Semiclassical S-matrix theory for atomic fragmentation. *Physics reports* **297**, 271–344 (1998).
- [62] Saalman, U., Mikaberidze, A. & Rost, J. M. Spatial correlations in finite samples revealed by coulomb explosion. *Physical review letters* **110**, 133401 (2013).
- [63] Motomura, K. *et al.* Sequential multiphoton multiple ionization of atomic argon and xenon irradiated by X-ray free-electron laser pulses from SACLA. *Journal of Physics B: Atomic, Molecular and Optical Physics* **46**, 164024 (2013).
- [64] Yeh, J. & Lindau, I. Atomic subshell photoionization cross sections and asymmetry parameters:  $1 \leq z \leq 103$ . *Atomic data and nuclear data tables* **32**, 1–155 (1985).
- [65] Carroll, T. *et al.* Carbon 1s photoelectron spectrum of methane: Vibrational excitation and core-hole lifetime. *Physical Review A* **59**, 3386 (1999).
- [66] Carroll, T. *et al.* Carbon 1s core-hole lifetime in CO<sub>2</sub>. *Physical Review A* **61**, 042503 (2000).
- [67] Schlachter, A. *et al.* Lifetime of a k-shell vacancy in atomic carbon created by  $1s \rightarrow 2p$  photoexcitation of C<sup>+</sup>. *Journal of Physics B: Atomic, Molecular and Optical Physics* **37**, L103 (2004).
- [68] Hartmann, E. X-ray fluorescence yields for light emitter atoms: carbon. *Journal of Physics B: Atomic, Molecular and Optical Physics* **21**, 1173 (1988).
- [69] Tashiro, M., Ehara, M. & Ueda, K. Double core-hole electron spectroscopy for open-shell molecules: Theoretical perspective. *Chemical Physics Letters* **496**, 217–222 (2010).
- [70] Inhester, L., Groenhof, G. & Grubmüller, H. Core hole screening and decay rates of double core ionized first row hydrides. *The Journal of chemical physics* **138**, 164304 (2013).
- [71] Cryan, J. P. *et al.* Auger electron angular distribution of double core-hole states in the molecular reference frame. *Physical review letters* **105**, 083004 (2010).
- [72] Breedlove, J. R. & Trammell, G. T. Molecular microscopy: Fundamental limitations. *Science* **170**, 1310–1313 (1970).

- [73] Garman, E. F. Radiation damage in macromolecular crystallography: what is it and why should we care? *Acta Crystallographica Section D: Biological Crystallography* **66**, 339–351 (2010).
- [74] Ravelli, R. B., Leiros, H.-K. S., Pan, B., Caffrey, M. & McSweeney, S. Specific radiation damage can be used to solve macromolecular crystal structures. *Structure* **11**, 217–224 (2003).
- [75] Bourenkov, G. P. & Popov, A. N. Optimization of data collection taking radiation damage into account. *Acta Crystallographica Section D: Biological Crystallography* **66**, 409–419 (2010).
- [76] Borek, D., Cymborowski, M., Machius, M., Minor, W. & Otwinowski, Z. Diffraction data analysis in the presence of radiation damage. *Acta Crystallographica Section D: Biological Crystallography* **66**, 426–436 (2010).
- [77] Owen, R. L., Rudiño-Piñera, E. & Garman, E. F. Experimental determination of the radiation dose limit for cryocooled protein crystals. *Proceedings of the National Academy of Sciences of the United States of America* **103**, 4912–4917 (2006).
- [78] Carugo, O. & Carugo, K. D. When X-rays modify the protein structure: radiation damage at work. *Trends in biochemical sciences* **30**, 213–219 (2005).
- [79] Neutze, R., Wouts, R., van der Spoel, D., Weckert, E. & Hajdu, J. Potential for biomolecular imaging with femtosecond X-ray pulses. *Nature* **406**, 752–757 (2000).
- [80] Solem, J. C. & Baldwin, G. C. Microholography of living organisms. *Science* **218**, 229–235 (1982).
- [81] Solem, J. C. Imaging biological specimens with high-intensity soft X-rays. *JOSA B* **3**, 1551–1565 (1986).
- [82] Henderson, R. The potential and limitations of neutrons, electrons and X-rays for atomic resolution microscopy of unstained biological molecules. *Quarterly reviews of biophysics* **28**, 171–193 (1995).
- [83] Kai, T. *et al.* Intensity of diffracted X-rays from biomolecules with radiation damage caused by strong X-ray pulses. *Journal of the Physical Society of Japan* **83**, 094301 (2014).
- [84] Jurek, Z. & Faigel, G. The effect of inhomogenities on single-molecule imaging by hard XFEL pulses. *EPL (Europhysics Letters)* **86**, 68003 (2009).
- [85] Hau-Riege, S. P. Photoelectron dynamics in X-ray free-electron-laser diffractive imaging of biological samples. *Physical review letters* **108**, 238101 (2012).
- [86] Fratallocchi, A. & Ruocco, G. Single-molecule imaging with X-ray free-electron lasers: Dream or reality? *Physical review letters* **106**, 105504 (2011).

- [87] Weierstall, U., Spence, J. & Doak, R. Injector for scattering measurements on fully solvated biospecies. *Review of Scientific Instruments* **83**, 035108 (2012).
- [88] Sierra, R. G. *et al.* Nanoflow electrospinning serial femtosecond crystallography. *Acta Crystallographica Section D: Biological Crystallography* **68**, 1584–1587 (2012).
- [89] Weierstall, U. *et al.* Lipidic cubic phase injector facilitates membrane protein serial femtosecond crystallography. *Nature communications* **5** (2014).
- [90] Zarrine-Afsar, A. *et al.* Crystallography on a chip. *Acta Crystallographica Section D: Biological Crystallography* **68**, 321–323 (2012).
- [91] Hattne, J. *et al.* Accurate macromolecular structures using minimal measurements from X-ray free-electron lasers. *Nature methods* **11**, 545–548 (2014).
- [92] Barends, T. R. *et al.* Anomalous signal from S atoms in protein crystallographic data from an X-ray free-electron laser. *Acta Crystallographica Section D: Biological Crystallography* **69**, 838–842 (2013).
- [93] Chapman, H. N. *et al.* Femtosecond diffractive imaging with a soft-X-ray free-electron laser. *Nature Physics* **2**, 839–843 (2006).
- [94] Gaffney, K. & Chapman, H. Imaging atomic structure and dynamics with ultrafast X-ray scattering. *Science* **316**, 1444–1448 (2007).
- [95] Bogan, M. J. *et al.* Single particle X-ray diffractive imaging. *Nano Letters* **8**, 310–316 (2008).
- [96] Chapman, H. N. *et al.* Femtosecond X-ray protein nanocrystallography. *Nature* **470**, 73–77 (2011).
- [97] Koopmann, R. *et al.* In vivo protein crystallization opens new routes in structural biology. *Nature methods* **9**, 259–262 (2012).
- [98] Sawaya, M. R. *et al.* Protein crystal structure obtained at 2.9 Å resolution from injecting bacterial cells into an X-ray free-electron laser beam. *Proceedings of the National Academy of Sciences* **111**, 12769–12774 (2014).
- [99] Boutet, S. *et al.* High-resolution protein structure determination by serial femtosecond crystallography. *Science* **337**, 362–364 (2012).
- [100] Aquila, A. *et al.* Time-resolved protein nanocrystallography using an X-ray free-electron laser. *Optics express* **20**, 2706–2716 (2012).
- [101] Kimura, T. *et al.* Imaging live cell in micro-liquid enclosure by X-ray laser diffraction. *Nature communications* **5** (2014).

- [102] Geloni, G. *et al.* Perspectives for imaging single protein molecules with the present design of the european XFEL. In *Free Electron Laser Conference 2014*, PUBDB-2014-03601, MOP082 (European XFEL, 2014).
- [103] Gnodtke, C., Saalman, U. & Rost, J. M. Ionization and charge migration through strong internal fields in clusters exposed to intense X-ray pulses. *Physical Review A* **79**, 041201 (2009).
- [104] Hau-Riege, S. P., London, R. A. & Szoke, A. Dynamics of biological molecules irradiated by short X-ray pulses. *Physical Review E* **69**, 051906 (2004).
- [105] Hau-Riege, S. P. *et al.* Sacrificial tamper slows down sample explosion in flash diffraction experiments. *Physical review letters* **104**, 064801 (2010).
- [106] Iwan, B. *et al.* Explosion, ion acceleration, and molecular fragmentation of methane clusters in the pulsed beam of a free-electron laser. *Physical Review A* **86**, 033201 (2012).
- [107] Hau-Riege, S. P., London, R. A., Chapman, H. N., Szoke, A. & Timneanu, N. Encapsulation and diffraction-pattern-correction methods to reduce the effect of damage in X-ray diffraction imaging of single biological molecules. *Physical review letters* **98**, 198302 (2007).
- [108] Bouvignies, G. *et al.* Solution structure of a minor and transiently formed state of a T4 lysozyme mutant. *Nature* **477**, 111–114 (2011).
- [109] Engler, N., Ostermann, A., Niimura, N. & Parak, F. G. Hydrogen atoms in proteins: positions and dynamics. *Proceedings of the National Academy of Sciences* **100**, 10243–10248 (2003).
- [110] Rhodes, G. *Crystallography made crystal clear: a guide for users of macromolecular models* (Academic press, 2010).
- [111] Barty, A. *et al.* Self-terminating diffraction gates femtosecond X-ray nanocrystallography measurements. *Nature Photonics* **6**, 35–40 (2012).
- [112] Hamilton, W. C. Significance tests on the crystallographic R factor. *Acta Crystallographica* **18**, 502–510 (1965).
- [113] Diederichs, K. Crystallographic data and model quality. *Nucleic Acid Crystallography: Methods and Protocols* 147–173 (2016).
- [114] Kleywegt, G. J. & Brünger, A. T. Checking your imagination: applications of the free R value. *Structure* **4**, 897–904 (1996).
- [115] Brunger, A. T., Kuriyan, J. & Karplus, M. Crystallographic R factor refinement by molecular dynamics. *Science* **235**, 458–460 (1987).

- [116] Jurek, Z. & Faigel, G. Orienting single-molecule diffraction patterns from XFELs using heavy-metal explosion fragments. *EPL (Europhysics Letters)* **101**, 16007 (2013).





# Acknowledgements

At this point, as I contemplate how a very unique and rewarding part of my life comes to an end, it is definitely no easy task to look over the long series of events that had driven me to this point. This is particularly true as I, along the way, got indebted and obliged to many people. I will try to do my best, however, to recognize them, with no particular order.

First of all, I would like to express my sincere gratitude to my advisors Prof. Jan-Michael Rost and Prof. Ulf Saalman. First of all for their guidance and support, but also for daring to accept me as a student despite my peculiar academic background. I really hope they had never regretted that decision. I am grateful for many lessons, some of them through long discussions or detailed explanations, but many other I learned by example. Thanks to them, I am now aware that to calculate is not the same as to understand, and that a complicated problem is not the same as an interesting one. I feel no shame to admit that my concept of what makes good research is now completely different. I also appreciate the freedom they gave me to look for my own answers, while at the same time making sure I kept focus and our research goals could be achieved. I plan to keep all these lessons in mind for the future.

The many different colleagues with whom I shared an office deserve a special mention. I am thankful to Nils Henkel, not only for being always certain to provide an almost excruciatingly quiet atmosphere at work, or showing me that no matter how far I travel, awful mexican pop music will find me. I am thankful to him for being at the same time a “very cliché” german, as he said, as well as a very peculiar one. I missed him, even if an equally quiet, slim, and tall european (and fellow 9gager) in the form of Rick van Bijnen came to the office in his place. I have even wondered if Rick was actually trying to make it easier for me by being intentionally just as quiet. Anyhow, I am also thankful to Rick, even if he always managed to mock me with some awful beer for my birthday, and despite the fact that the Netherlands kicked Mexico out of the World Cup. I will finish thanking also my other fortunately not so quiet office mates, Julia Gundermann and Darko Dimitrovski, with whom I shared the office for a period of time way too short for my taste.

I was fortunate enough to be able to work in a great environment with great people, both colleagues and friends. In my many years in the institute I saw many people come and leave the Finite Systems group: Fabian Maucher, Rick Mukherjee, Sebastian Wüster, Carlos Zagoya, Martin Winter, Georg Bannasch, Pierfrancesco Di Cintio, Alexey

Mikaberidze, Christian Gnodtke, Elias Diesen, Karsten Leonhardt, Adrian Sanz Mora, David Schönleber, Andreas Rubisch, Pablo López Vázquez, Alan Celestino, Mehrdad Baghery, Callum Murray, Koen van Kruining, Wildan Abdussalam, Laura Gil, Zach Walters, Thomas Pohl, Stefan Skupin, Valentin Walther, Alex Eisfeld, Tommaso Macri, Marko Gaćeša, Jörg Götte, among many others, all of them deserving my most sincere appreciation and admiration. All of them deserve special remarks, from the funny, witty and kicker obsessed Fabian, or the usual targets of my mean spirited jokes Alan and Mehrdad (whom I unfortunately will have to hurt at some point, he knows why), to the bouldering boss and cold weather enthusiast Karsten, but I lack enough space to properly do so. I am also afraid I am unavoidably forgetting more than a couple people, and I deeply apologize in advance.

I purposely forgot to include Michael Genkin in the previous list, not to annoy him (which sounds like something I would do), but because he deserves special credit as coordinator of the IMPRS program, a task he had performed admirably. On the same topic, I also like to acknowledge and thank my fellow students in the program, for the nice informal discussion we held during the program retreats as well as the pleasant social aftermaths. Unfortunately, again, they are way too many to properly thank them individually.

I am also grateful to many other colleagues and friends from the institute. For example Pablo Sartori, the only reason why I have a gym membership (and, even if he will not believe me, I actually use it). It was always a pleasure to see Anna Deluca coming into the office for a quick talk, usually involving something geeky, and I also appreciate her sister-like concern over my well being. Petruța was always a good friend, even if it was incredibly frustrating how she could understand every single word I said in spanish, while romanian was completely inaccessible to me. It was a lot of fun to be around Federico Vázquez, proving once again mexicans and argentinians necessarily express their friendship through mean personal jokes, almost instantly. It is funny how I managed to become friends with Xavier Prudent *before* he became part of the institute, thanks to a particularly severe winter and delayed trains at Berlin. Once again, there are more people to thank, but not enough space, like Younes, Omar, Talia, Izaak, Jorge, Colm, Johannes, etc. Sorry I cannot elaborate more.

Outside the institute I also had the support from many people to keep a good mod and a healthy mind. I could start with Rafael, Tamara, Carla, Peter, and David, among others, with whom I spent good times during my first years. Also among them is Jorge Robles, a very good friend, always capable of a good chat. I also appreciate the mostly spanish table in the Mensa, particularly Eugenio Patallo who provided a lot of entertainment at lunch time. Thanks to both Artur and Marolyn with whom I got to know amazing places in Poland, and spent many good moments in Dresden. Melanie Ludwig was probably my first german friend outside the institute, a very good way to start. Other good friends, Maxi and Stefi were probably 85% responsible of me having a social life. I also want to thank my friends and countrymen in Dresden: Nasser and Sandra, for sharing my passion for action packed commercial movies, Alejandra for being a good friend and sharing the usual joys and frustrations of being abroad, and Anibal

for unexpectedly bringing a piece of my city to Dresden.

This has been a learning experience in different ways, and one of them came in the form of Liza Monges. From her I learned new things, way too many to enumerate, that can not be thanked, just treasured deeply. Most of my dearest experiences during this period of time happened at her side.

Only God knows what would I be without my family. In that respect, I have been more than fortunate. For the father I have, Moisés Camacho, who supported me all this time, even if he had trouble understanding this alien world of academia. I am entirely sure he will be even happier than me when I finish my studies. For my mother Carmina, who has supported me in in a way that always made me be certain I was doing the right thing. My brother Joaquín is probably indirectly responsible for me turning into physics. My grandparents also deserve a special mention, as they were more than a fundamental part of my early years and they are always in my thoughts. As I said. . . I have been very fortunate.



# Versicherung

Hiermit versichere ich, dass ich die vorliegende Arbeit ohne unzulässige Hilfe Dritter und ohne Benutzung anderer als der angegebenen Hilfsmittel angefertigt habe; die aus fremden Quellen direkt oder indirekt übernommenen Gedanken sind als solche kenntlich gemacht. Die Arbeit wurde bisher weder im Inland noch im Ausland in gleicher oder ähnlicher Form einer anderen Prüfungsbehörde vorgelegt.

Die Arbeit wurde am Max-Planck-Institut für Physik komplexer Systeme in der Abteilung "Endliche Systeme" angefertigt und von Prof. Dr. Jan-Michael Rost betreut.

Ich erkenne die Promotionsordnung der Fakultät Mathematik und Naturwissenschaften der Technischen Universität Dresden vom 23 Februar 2011 an.

---

Abraham Camacho Garibay